

Towards low-cost PEM fuel cells

Interfacial effects and material dynamics of a non-PGM electrocatalyst

Rangel Cardenas, A.L.

DOI

[10.4233/uuid:e164a3b3-75fb-4879-ba5e-27f7f50b3e6b](https://doi.org/10.4233/uuid:e164a3b3-75fb-4879-ba5e-27f7f50b3e6b)

Publication date

2021

Document Version

Final published version

Citation (APA)

Rangel Cardenas, A. L. (2021). *Towards low-cost PEM fuel cells: Interfacial effects and material dynamics of a non-PGM electrocatalyst*. [Dissertation (TU Delft), Delft University of Technology]. <https://doi.org/10.4233/uuid:e164a3b3-75fb-4879-ba5e-27f7f50b3e6b>

Important note

To cite this publication, please use the final published version (if applicable). Please check the document version above.

Copyright

Other than for strictly personal use, it is not permitted to download, forward or distribute the text or part of it, without the consent of the author(s) and/or copyright holder(s), unless the work is under an open content license such as Creative Commons.

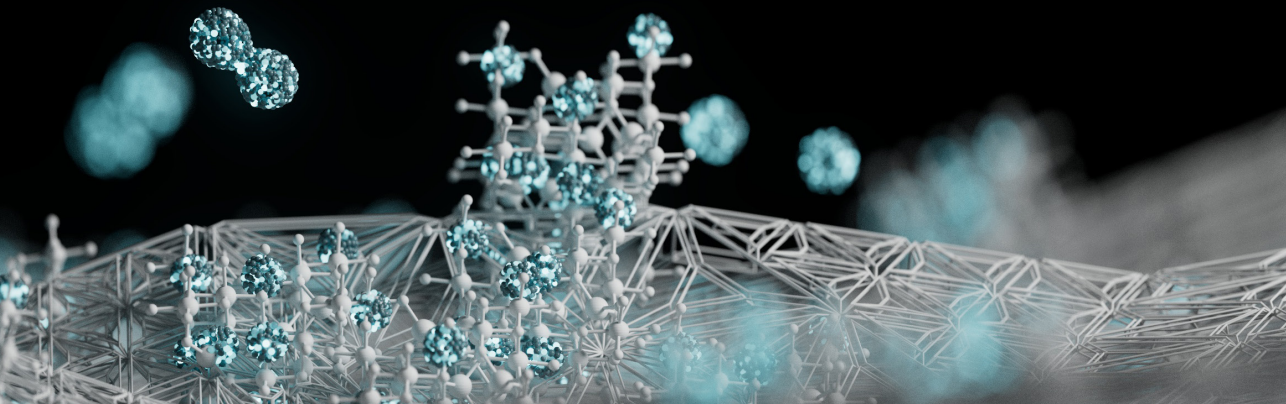
Takedown policy

Please contact us and provide details if you believe this document breaches copyrights. We will remove access to the work immediately and investigate your claim.

Angie L. Rangel Cárdenas

TOWARDS LOW-COST PEM FUEL CELLS

Interfacial effects and material dynamics
of a non-PGM electrocatalyst



Propositions

accompanying the dissertation

Towards low cost PEM fuel cells

Interfacial effects and material dynamics of a non-PGM electrocatalyst

by

Angie L. Rangel-Cárdenas

1. Interfaces are experimental, bulk is fundamental.
(Chapters 2, 3, 4 and 5 of this thesis.)
2. Traditional testing techniques often do not reflect the real conditions of the intended application, leading to extraordinary claims or limiting us from re-searching in different directions.
(Chapters 4 and 5 of this thesis.)
3. Typical hot-pressing methods to fabricate MEAs may cause fundamental changes to the materials, rendering fundamental research mostly useless.
(Chapter 5 of this thesis.)
4. Manganese oxides are an electrocatalysis super-hero as their spin- and electronic configurations can be fine-tuned according to the desired application.
(Chapters 4 and 5 of this thesis.)
5. Policies that favour women towards high positions are not a sign of their weakness, but crucial to close the gender gap in academia and industry.
6. Indifference is at the heart of all problems. If we are not part of the solution, then we are perpetuating the problem.
7. Idolization of extroverted traits is yet another form of discrimination that leads to stereotyping of introverts and disregards their contribution to society.
8. Perfection is often expected from those taking steps towards a more conscious and sustainable lifestyle, while imperfect solutions are already better.
9. Asking someone with mental health illness to 'just get over it' is as ridiculous as asking someone with a gallbladder problem to 'just heal it'.
10. Letting go is a valuable skill both for life as for science. There is no perfect experiment or perfect data, making drawing conclusions and generating knowledge an art form.

These propositions are regarded as opposable and defensible, and have been approved as such by the promotor prof. dr. S.J. Picken.

Towards low-cost PEM fuel cells

Interfacial effects and material dynamics of a
non-PGM electrocatalyst

Towards low-cost PEM fuel cells

Interfacial effects and material dynamics of a
non-PGM electrocatalyst

Proefschrift

ter verkrijging van de graad van doctor
aan de Technische Universiteit Delft,
op gezag van de Rector Magnificus Prof. dr. ir. T.H.J.J. van der Hagen,
voorzitter van het College voor Promoties,
in het openbaar te verdedigen op 4 November 2021 om 10:00 uur

door

Angie Lorena Rangel Cárdenas

Chemical Engineer
Universidad Industrial de Santander

Master of Science in Sustainable Energy Technologies
Technische Universiteit Delft

geboren te Ocaña, Colombia.

Dit proefschrift is goedgekeurd door de

promotor: prof. dr. S.J. Picken

promotor: dr. ir. G.J.M. Koper

promotor: dr. E.M. Kelder

Samenstelling promotiecommissie:

Rector Magnificus,
Prof. dr. S.J. Picken,
Dr. ir. G.J.M. Koper,
Dr. E.M. Kelder,

voorzitter
Technische Universiteit Delft
Technische Universiteit Delft
Technische Universiteit Delft

Onafhankelijke leden:

Prof. dr. ir. F. Mulder
Prof. dr. M. Koper
Prof. dr. S. Kjelstrup,
Prof. dr. J.E. ten Elshof,
Prof. dr. ir. M. Wagemaker,

Technische Universiteit Delft
Leiden University, Netherlands
NTNU, Norway
Twente University, Netherlands
Technische Universiteit Delft, reservelid



Keywords: PEM fuel cell; interfaces; transport resistance; electrocatalysis; spinel LMO; HOR; ORR.

Printed by: Proefschriftmaken

Front & Back: Beautiful cover art that captures the entire content of this thesis in a single illustration by Manuel Zeller.

Copyright © 2021 by A.L. Rangel Cárdenas

ISBN 978-94-6384-264-8

An electronic version of this dissertation is available at

<http://repository.tudelft.nl/>.

A Pa, Ma y Javi.

Contents

Summary	xi
Samenvatting	xv
1 Introduction	1
1.1 The PEM fuel cell	5
1.2 Alternative materials	7
1.2.1 Spinel LiMn_2O_4	10
1.3 Electrocatalysis	10
1.4 Outlook of this thesis	12
References	13
2 Transport in PEMFCs	19
2.1 Introduction	20
2.2 Transport Coefficient Matrix Method (TCM)	21
2.3 Membrane properties: a literature survey	24
2.3.1 Proton conductivity	24
2.3.2 Water permeability	28
2.3.3 Hydrogen permeability	30
2.3.4 Electro-osmotic drag	31
2.4 Discussion	33
2.5 Conclusions	36
References	38
3 Anomalous water sorption kinetics	43
3.1 Introduction	44
3.2 Experimental	46
3.2.1 Home-made electrode fabrication	46
3.2.2 MEA preparation and characterization	46
3.2.3 Water sorption measurements	47
3.3 Results	47
3.3.1 MEA preparation and characterization	47
3.3.2 Equilibrium water sorption	47
3.3.3 Water sorption kinetics	48
3.3.4 Interfacial effects in a simplified mathematical model	52
3.3.5 Analysis of interfacial effects	54
3.4 Discussion	56
3.5 Conclusion	57
3.A SEM micrographs of electrodes	59
3.B SEM micrographs pristine electrode vs. MEA	60
3.C Mean surface roughness	60

3.D Onset time as a function of interfacial resistance	60
References	61
4 Structure/activity insights on protonated spinel LiMn_2O_4	65
4.1 Introduction	67
4.2 Experimental	69
4.2.1 Synthesis of $\text{Li}_{1+\delta}\text{Mn}_{2-\delta}\text{O}_4$ (LMOd)	69
4.2.2 De-lithiation/Protonation	70
4.2.3 Deuteration	71
4.2.4 XRD, SEM and ICP measurements	72
4.2.5 Neutron Diffraction.	72
4.2.6 Solid-state NMR	72
4.2.7 Electrochemical tests	73
4.3 Results	73
4.3.1 Leaching in acid solution and temperature stability of crystal structure	73
4.3.2 Controlled ion-exchange (Li^+/H^+) by titration	74
4.3.3 Structure and composition analysis by neutron diffraction	75
4.3.4 Chemical shift of protonated LMOs	78
4.3.5 Electrochemical performance of HLMOs electrocatalysts for ORR in acidic media	81
4.4 Discussion	82
4.5 Conclusion	87
4.A Hahn-echo pulse program for ^2H measurements	89
4.B Synthesis of starting spinels	89
4.C Temperature studies	90
4.D Titration curves	91
4.E SEM micrographs	93
4.F Neutron Diffraction.	93
4.G Solid-state NMR	95
4.H Mn OS validation	96
References	97
5 Protonated LMOs as electrocatalysts in a PEMFC	103
5.1 Introduction	105
5.2 Experimental	107
5.2.1 Synthesis	107
5.2.2 Membrane Electrode Assembly (MEA) preparation	107
5.2.3 Characterization	108
5.2.4 Electrochemical measurements	108
5.2.5 X-ray absorption (XAS) measurements	108
5.2.6 XAS Data Analysis	109

5.3	Results	109
5.3.1	Synthesis	109
5.3.2	MEA fabrication	110
5.3.3	Cubic spinel types as potential ORR and HOR catalysts.	112
5.3.4	XAS of disordered HLMO in <i>operando</i> fuel cells	113
5.3.5	Ex-situ measurements of pure cubic spinel HLMO in a PEMFC	114
5.4	Discussion.	116
5.4.1	Characterisation	116
5.4.2	Performance.	118
5.5	Conclusions	121
5.A	Fuel cell	122
5.B	XAS set-up	122
5.C	Calibration of Mn oxidation state	123
5.D	EXAFS upon Nafion addition	124
5.E	Identification of non-spinel reflections in Electrodes and MEAs	124
5.F	FC under constant voltage conditions	125
	References.	126
	Acknowledgements	133
	Curriculum Vitæ	139
	List of Publications	141

Summary

The rapid increase in global energy consumption and world population calls for faster solutions to alleviate the damage done so far to the environment and minimise the dire consequences we might expect in the next decades. In the last 100 years, energy consumption has increased almost 10-fold, going from 18 PWh a year to ~171 PWh a year. At the same time, global population has multiplied 4-fold and is predicted to be around 8.5 billion by 2030 and 9.7 billion by 2050. A larger population will intensify energy demands, making controlling our CO₂ emissions more urgent than ever. Increasing the utilisation of renewable energy sources has been a main objective in order to comply to the Paris agreement of keeping the global temperature increase below 2 °C and to comply to the EU Green Energy Deal of carbon neutrality by 2050. Towards this direction, hydrogen has been proposed as a strong candidate as it is a transportable and storable energy carrier. As a fuel, it can be used in polymer-electrolyte-membrane fuel cells (PEMFCs) where it can generate electricity by recombining hydrogen with oxygen having water as the only by-product. This makes it an attractive device in the quest for carbon-neutral energy production. Since they were first used in the 1970s to power a spacecraft, PEMFCs lost traction due to their high cost and short lifetime. However, this clean energy technology has recently regained interest in academia, government and industry. As an example of fuel cell (FC) commercialisation, we have seen successful introduction of FC vehicles in the market in the last few years. Since the world's first FC vehicle was introduced into the commercial market in 2002 by Toyota, FC vehicles and FC hybrid vehicle production and use has steadily increased.

PEMFCs find application in many fields such as portable power, stationary electricity generation, transportation or large electrical plants. The most common application of PEMFCs is in vehicle engines where they are usually paired with other forms of energy storage units in what is known as hybrid electric vehicles (HEVs). Despite their many environmental and efficiency advantages, PEMFCs still face many challenges before they can reach broader commercial use. The most important factor in this regard is probably their still high cost, where approximately 40-50% of a FC stack cost is due to the materials used as catalysts, i.e. Pt group metals (PGMs). Platinum is an ideal electrocatalyst due to its fast kinetics in acidic media towards the oxygen reduction and hydrogen oxidation reactions (ORR and HOR, respectively). However, its high cost and susceptibility to CO poisoning have been a major impediment to the commercial establishment of PEMFCs. This has led to research focusing on lowering Pt loading, specially at the cathode where about 80% of the catalyst is found due to the more sluggish kinetics of the ORR. On the other hand, developing PGM-free electrocatalysts to completely replace Pt with cheap, Earth-abundant materials is another solution that has shown a lot of potential. A significant improvement has been shown towards ORR in the last decade with a lot of these electrocatalysts using Co, Fe, Ni, Mn, etc., in different crystal structures.

In general, transition metals oxides (TMOs) have recently attracted a lot of attention because of their low cost, high electrical conductivity and their wide range of chemical and physical properties. There is a broad range of crystal structures with their accompanying metal oxidation state, electronic configuration and magnetic properties that are fundamentally interesting to understand in order to rationally design new, more efficient electrocatalysts.

In this thesis, fundamental insights on a non-PGM material will be presented, i.e. *spinel* LiMn_2O_4 -based electrocatalyst for PEMFC, and its working principle as a HOR and ORR electrocatalyst. In addition to that, part of this thesis will deal with FCs in a more "macro-scale" viewpoint. There is still a wide gap when translating intrinsic activity of the catalytic materials into membrane-electrode assemblies (MEAs) and a complete FC. This has to do with the traditional methods employed to screen new materials, which are typically not representative of a real-world FC, e.g. liquid electrolyte vs. polymer electrolyte. To this end, interfacial effects in a PEMFC have been studied by means of mass and charge transport where we show that losses in this small area of a cell are the most significant, thus making it major focus when designing new devices.

In chapter 1, the context in which the importance of fuel cells exists is presented. At the same time, the theory and methods relevant to understand the following chapters are shortly presented.

In chapter 2, we discuss the ambiguity found in literature when discussing transport properties while we emphasize that these cannot be properly discussed unless interfacial effects are taken into consideration. Here, we propose an approach based on non-equilibrium thermodynamics in order to disentangle the effects of bulk and interface in these properties. In addition, in chapter 3, we study interfacial effects on mass transport further. We show that deviation from Fickian behaviour in water transport in a half MEA is due to interfacial effects and that results may vary in orders of magnitude depending on the length scale studied.

In chapters 4 and 5, we study a novel electrocatalyst based on a *spinel* lithium manganate. We propose that proton insertion in a *spinel* LiMn_2O_4 (LMO) can make it active towards ORR and HOR. First, we describe synthesis methods and study proton insertion in the *spinel* crystal structure. Proton insertion is achieved by ion-exchange with Li ions in the structure. We find protonation to happen in two steps; first, Li is removed from the structure down to 60%, and second, a Li^+/H^+ exchange reaction is dominant below this point. In addition, we have found protons to occupy the 96g position (in Wyckoff notation) of the crystal structure.

These proton-exchanged LMOs, or HLMOs, as we shall refer to them, show an increased activity towards ORR in acidic media. We believe a synergistic effect between protons and active Mn centres is responsible for the increased activity. Furthermore, we believe Mn(III) centres with the high-spin configuration to be the active Mn site and whose formation is aided by proton insertion and by small amounts of Li remaining in the structure.

Finally, HLMOs were tested in an operating FC. Here we found them to be active at either electrode, i.e. to HOR or ORR. Oxygen vacancy formation/annihilation and changes in the local structure are found to occur in the HLMO depending on

whether it is used at the oxygen side or the hydrogen side. This can be understood as the opportunity to optimize the material towards one reaction or the other by fine-tuning structural and chemical properties such as oxidation state, bond length, metal centre coordination number and oxygen vacancy concentration. Furthermore, we find structure reversibility in HLMO electrocatalyst, meaning that by inverting the cell the initial structure could be recovered at least twice. This opens opportunities for future research in catalysis regeneration.

In short, in this thesis we aim to demonstrate the importance of interfaces and to propose a new class of materials that could lead to low cost PEMFCs. We provide tools to analyse interfaces in more systematic manners and propose a material with inexpensive preparation methods whose raw cost is ca. 3000 times lower than that of platinum.

Samenvatting

De snelle toename van het wereldwijde energieverbruik en de wereldbevolking vraagt om snellere oplossingen om de schade aan het milieu tot nu toe te verlichten en de ernstige gevolgen die we in de komende decennia kunnen verwachten tot een minimum te beperken. In de afgelopen 100 jaar is het energieverbruik bijna vertienervoudigd, van 18 PWh per jaar naar ~171 PWh per jaar. Tegelijkertijd is de wereldbevolking vermenigvuldigd met een viervoud en er wordt voorspeld dat er tegen 2030 ongeveer 8.5 miljard mensen zullen zijn en in 2050 9.7 miljard. Het verhogen van het gebruik van hernieuwbare energiebronnen is een belangrijke doelstelling geweest om te voldoen aan de "Paris agreement" en "de EU Green Energy of carbon neutrality" om de wereldwijde temperatuurstijging tegen 2050 onder de 2 °C te houden. Daarom is waterstof voorgesteld als een potentiële kandidaat, omdat het een transporteerbare en opslaanbare energiedrager is. Als brandstof kan het worden gebruikt in Polymer Electrolyte Membrane brandstofcellen (PEMFCs) waar het elektriciteit kan opwekken door waterstof opnieuw te laten reageren met zuurstof met water als enige bijproduct. Dit maakt het een aantrekkelijk systeem in de zoektocht naar CO₂-neutrale energieproductie. Sinds de PEMFCs voor het eerst werden gebruikt in de jaren 1970, om een ruimtevaartuig van stroom te voorzien, verloren PEMFCs interesse vanwege hun hoge kosten en korte levensduur. Deze schone energietechnologie heeft echter onlangs weer interesse gewekt in de academische wereld, de overheid en de industrie. Als voorbeeld van commercialisering van brandstofcellen (Fuel Cells, FCs) hebben we de afgelopen jaren een succesvolle introductie van FC-voertuigen op de markt gezien. Sinds 's werelds eerste FC-voertuig in 2002 op de markt werd geïntroduceerd door Toyota, zowel FC-voertuigen als FC-hybride voertuigen, is de productie en het gebruik gestaag toegenomen.

PEMFCs vinden toepassing op vele gebieden zoals in draagbare power tools, stationaire elektriciteitsproductie, vervoer of grote elektriciteitsbedrijven. De meest voorkomende toepassing van PEMFCs is in voertuigmotoren waar ze meestal worden gekoppeld aan andere vormen van energieopslagsystemen in zogenaamde hybride elektrische voertuigen (HEV's). Ondanks hun vele milieu- en efficiëntievoordelen staan PEMFCs nog steeds voor veel uitdagingen voordat ze een breder commercieel gebruik bereiken. De belangrijkste factor in dit opzicht is waarschijnlijk hun nog steeds hoge kosten, waar ongeveer 40 - 50% van de kosten van een FC-stack te wijten is aan de materialen die als katalysatoren worden gebruikt, d.w.z. Platina-achtige materialen, de zogenaamde PGMS. Platina (Pt) is een ideale elektro-katalysator vanwege de snelle kinetiek in zure media ten opzichte van de zuurstofreductie en waterstofoxidatiereacties (respectievelijk ORR en HOR). De hoge kosten en gevoeligheid voor CO-vergiftiging zijn echter een grote belemmering geweest voor de commerciële implementatie van PEMFCs.

Dit heeft geleid tot onderzoek gericht op het verlagen van het Pt-gehalte, vooral

in de kathode waar ongeveer 80% van de katalysator wordt gevonden vanwege de meer trage kinetiek van de ORR. Aan de andere kant is het ontwikkelen van PGM-vrije elektrokatalysatoren om Pt volledig te vervangen door goedkope, ruim-beschikbare materialen, een interessante oplossing die in het afgelopen decennium potentie heeft getoond met een aanzienlijke verbetering ten opzichte van ORR. Veel van deze elektrokatalysatoren gebruiken Co, Fe, Ni, Mn, enz., in verschillende soorten kristalstructuren. Over het algemeen hebben overgangsmetaaloxiden (TTO's) de laatste tijd veel aandacht getrokken vanwege hun lage kosten en hun variabele oxidatietoestanden (OS), wat in combinatie met een hoge elektrische geleidbaarheid hen interessante chemische en fysische eigenschappen geeft. Er is een breed scala aan kristalstructuren met hun bijbehorende metaaloxidatietoestand, elektronische configuratie en magnetische eigenschappen die fundamenteel interessant zijn om te onderzoeken om rationeel nieuwe, efficiëntere elektrokatalysatoren te ontwerpen.

In dit proefschrift worden fundamentele inzichten over niet-PGM-materialen gepresenteerd, die gebaseerd zijn op spinel LiMn_2O_4 elektrokatalysatoren voor PEMFC waarbij het werkingsprincipe als HOR- en ORR-elektrokatalysator worden belicht. Daarnaast zal een deel van dit proefschrift gaan over FC's in een meer "macro-scale" kader. Er is nog steeds een grote kloof bij het vertalen van de intrinsieke activiteit van de katalysatormaterialen in zogenaamde membraan elektrodesystemen (MEA's) en een complete FC. Dit heeft te maken met de traditionele methoden die worden gebruikt om nieuwe materialen te screenen, die meestal niet representatief zijn voor een echte FC, bijvoorbeeld vloeibaar elektrolyt versus polymerelektrolyt. Hiertoe zijn interface effecten in een PEMFC bestudeerd door middel van massa- en ladingstransport, waarbij we aantonen dat verliezen in dit kleine deel van een cel het belangrijkste zijn, wat cruciaal is bij het ontwerpen van nieuwe apparaten.

In hoofdstuk 1 wordt het belang van brandstofcellen beschreven. vervolgens worden de theorie en methoden die relevant zijn om de volgende hoofdstukken te begrijpen gepresenteerd.

In hoofdstuk 2 bespreken we de discussie die in de literatuur wordt aangehouden bij het verklaren van transporteigenschappen, waarbij we benadrukken dat deze niet goed kunnen worden besproken tenzij er rekening wordt gehouden met interface-effecten.

Hier stellen we een aanpak voor op basis van niet-evenwichtsthermodynamica om de effecten van bulk- en interface-eigenschappen uit de doeken te doen.

Daarnaast bestuderen we in hoofdstuk 3 de interface-effecten op het massatransport in meer detail. We laten zien dat afwijking van Fickiaansgedrag in het watertransport in een halve MEA te wijten is aan interface-effecten en dat de resultaten kunnen variëren in ordes van grootte, afhankelijk van de onderzochte lengteschaal.

In hoofdstuk 4 en 5 bestuderen we een nieuwe elektrokatalysator gebaseerd op een spinel lithiummanganate (LiMn_2O_4). We veronderstellen dat protoninsertie in een spinel LiMn_2O_4 (LMO) het actief kan maken voor ORR en HOR. Eerst beschrijven we synthesemethoden en bestuderen we protoninsertie in de spinel-kristalstructuur. Protoninsertie wordt bereikt door ionenuitwisseling met Li-ionen

vanuit de structuur. We vinden protonering in twee stappen; allereerst wordt Li tot 60% uit de structuur verwijderd en ten daarna ontstaat een uitwisselingsreactie van Li^+ met H^+ onder dit punt. Deze H^+ -ionen komen vervolgens op de 96g-positie (in Wyckoff-notatie) van de kristalstructuur in plaats van op de 8a-positie die de Li^+ -ionen innamen. Deze proton-uitgewisselde LMO's, of HLMOs, zoals we ze zullen noemen, vertonen een verhoogde activiteit ten opzichte van ORR in zure media. Wij geloven dat een synergetisch effect tussen protonen en actieve Mn-centra verantwoordelijk is voor de verhoogde activiteit. Bovendien geloven we dat Mn(III)-centra met de hoogspin-configuratie de actieve Mn-sites zijn en waarvan de vorming wordt ondersteund door protoninsertie en door kleine hoeveelheden Li die in de structuur achterblijven.

Ten slotte werden HLMOs getest in een operationele brandstofcel. Hier vonden we dat ze actief waren op beide elektrodes, d.w.z. op HOR en ORR. De structuur is verder onderhevig aan vorming en annihilatie van zuurstofvacatures, afhankelijk van of het aan de zuurstof- of waterstofzijde wordt gebruikt.

Voorts kan dit worden gebruikt als mogelijkheid om het materiaal voor de ene of de andere reactie (HOR of ORR) te optimaliseren door structuur- en chemische eigenschappen zoals oxidatietoestand, bindingslengte, coördinatie nummer van het metaalion en de zuurstofvacaturenconcentratie te optimaliseren. Bovendien vinden we dat de structuur zich reversibel gedraagt in dezen HLMO-elektrokatalysator, wat betekent dat door de cel om te keren de oorspronkelijke structuur kan worden teruggewonnen. Dit opent kansen voor toekomstig onderzoek naar katalyseregeneratie.

Kortom, in dit proefschrift willen we het belang van interfaces aantonen en een nieuwe klasse materialen voorstellen die kunnen leiden tot goedkope PEMFCs. We geven methodes aan om interfaces systematischer te analyseren en stellen een materiaal voor met goedkope bereidingsmethoden waarvan de grondstofkosten ca. 3000 keer lager zijn dan die van platina.

1

Introduction

*The plan unravelled in freedom, so to speak,
as did all (his) other plans and intentions.*

Patrick Süskind, *The Perfume*

In this thesis several aspects of PEM fuel cells will be discussed from an atomic scale, e.g. crystal and electronic structure of non-noble metal materials for electrocatalysis and their dynamics, to a meso-macro scale, e.g. transport properties in a cell and interfacial effects on them. In this chapter basic theory necessary to understand the following chapters is presented as well as the context in which PEM fuel cells are considered important as devices for cleaner energy production. We describe alternative materials and a short background of the material type studied in this thesis. The work done in each chapter is shortly described in the last section.

In the last few decades we have seen a rapid increase in research and utilisation of renewable energy sources as the world's energy consumption has spiked. However, this rise in renewable technologies, although promising, is still far from ideal. In 2019, energy consumption was approximately 10 times larger than a hundred years before, going from 18 PWh to ~ 171 PWh [1] (see figure 1.1). At the same time, population has had a near 4-fold increase since the 1920s and is predicted to be around 8.5 billion by 2030 and 9.7 billion by 2050 [2] (see figure 1.2). Decreasing fossil fuel supply as well as increasing environmental and health concerns associated to their use, has been the drive of research and implementation of renewable energies in the last decades. In the last 50 years, we have seen renewable energy generation and consumption grow by almost a factor of 2, growing from ~ 10 PWh in 1965 to ~ 18 PWh in 2019 [1]. Nevertheless, this is still a small increase in half a century and just a fraction of overall energy consumption. In order to keep in line with the Paris agreement's objectives of keeping the global temperature increase below 2°C , the EU aims for carbon neutrality by 2050 as laid in the Green Energy Deal [3].

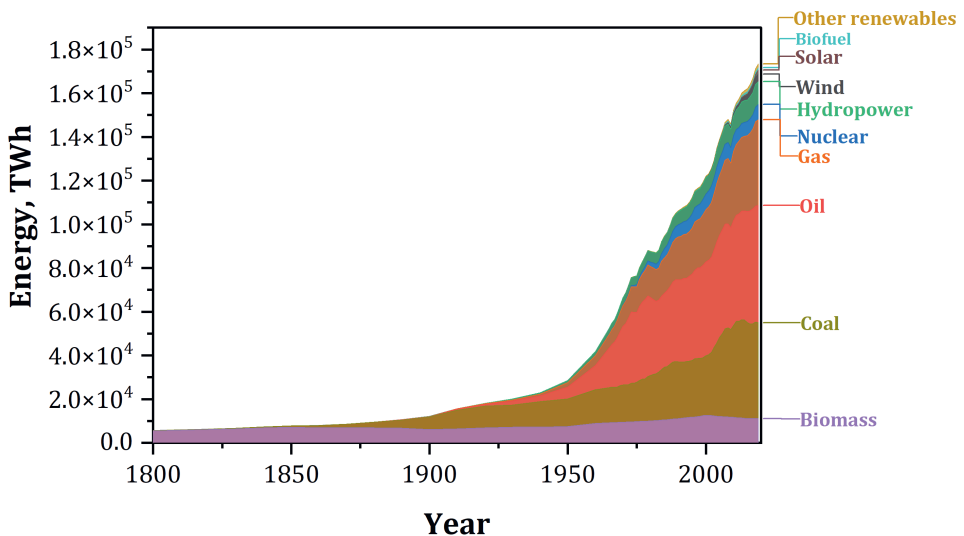


Figure 1.1: Global energy consumption by source.

Hydrogen has been proposed as a strong candidate in achieving these objectives as it is a transportable and storable energy carrier. When produced from electrolysis powered by renewable sources, e.g. the sun or wind, hydrogen is an ideal candidate. As a fuel, it can be used in polymer-electrolyte-membrane fuel cells (PEMFCs) where it can generate electricity by recombining hydrogen with oxygen having water as the only by-product, thus being an attractive device in the search for carbon-neutral energy production. Since they were first used in the 1970s to

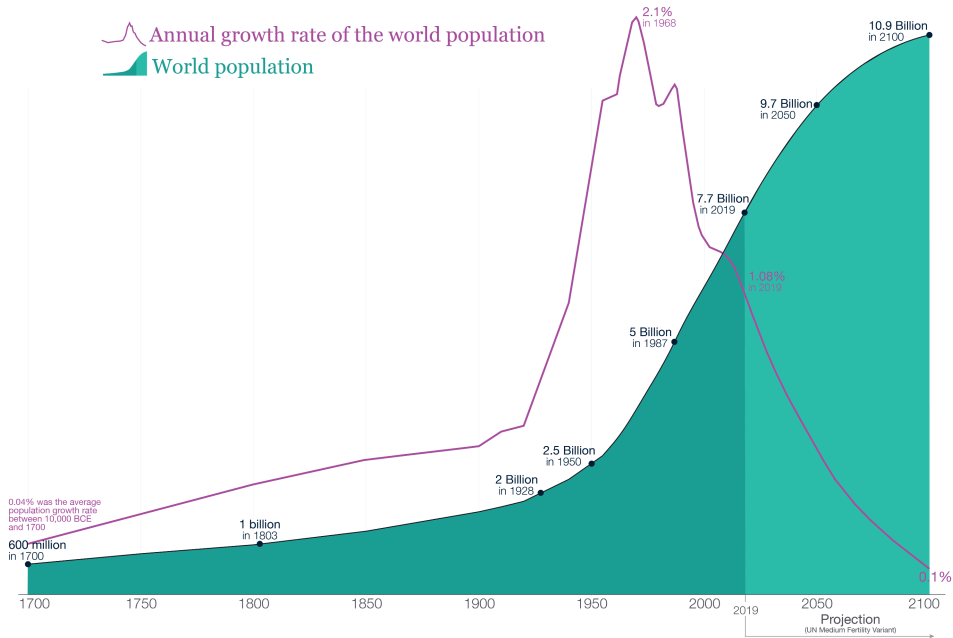


Figure 1.2: Population growth from the 1700s up to the present days and prediction until 2100 [2].

power a space mission, PEM fuel cells lost traction due to their high cost and short lifetime. However, this clean energy technology has recently regained interest in academia, government and industry [4]. As an example of fuel cell commercialization, we have seen successful introduction of fuel cell vehicles in the market in the last few years [4]. Since the world's first fuel cell vehicle was introduced into the commercial market in 2002 by Toyota [5], FC vehicles and FC hybrid vehicles production and use has steadily increased. In fact, the market size is projected to increase globally by ~66% (Compound Annual Growth Rate) by 2026 in comparison to 2019 with Honda, Toyota, Hyundai, Daimler, Audi, BMW, Volvo, Ballard Power Systems, General Motors and MAN as the major companies in the market [6].

PEM fuel cells find application in many fields such as portable power, stationary electricity generation, transportation or large electrical plants [7]. The most common application of PEMFCs is in vehicle engines where they are usually paired with other forms of energy storage units in what is known as hybrid electric vehicles (HEVs). However, in marine and air transportation they have been recently attracting more attention. The use of PEMFCs in surface ships is currently in demonstration whilst products for underwater vehicles are already in production [8]. In aviation, they are considered energy systems for Unmanned Aviation Vehicles (UAVs, or drones). On the other hand, PEMFCs have become strong competitors against batteries in stationary power generation where uninterrupted power supply is required [8] as well as they gained more attention in residential buildings when combined

with heat and power supplies [8].

Despite their many environmental and efficiency advantages, PEM fuel cells still face many challenges before they reach broader commercial use, among which their still high cost is probably the most important factor. Figure 1.3 shows the distribution of cost by component in a PEMFC stack (taken from [9]). Approximately 40-50% of a fuel cell stack cost is due to the materials used as catalysts, i.e. Pt group metals (PGMs) [4, 9].

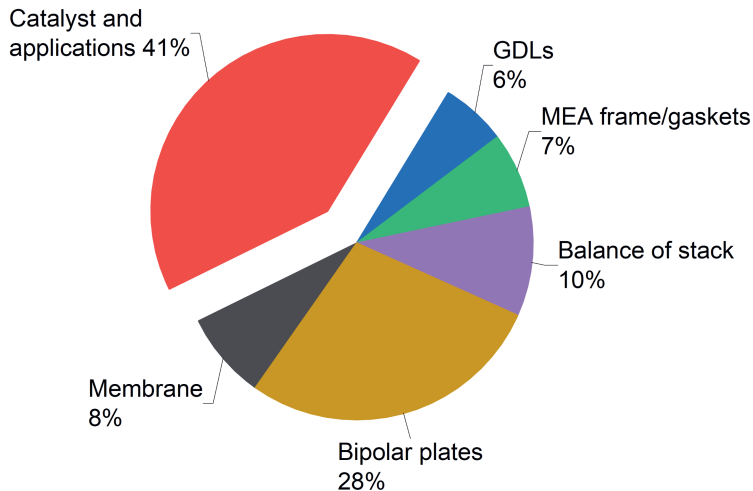


Figure 1.3: Component cost breakdown at a production volume of 500,000 units/yr for a fuel cell stack.

The fast kinetics of platinum as catalyst towards ORR and HOR in acidic media makes it the golden standard catalyst for PEMFCs. However, its high cost and susceptibility to CO poisoning have been a major impediment to the commercial establishment of PEMFCs. This has led to a research focus on lowering the Pt loading, specially at the cathode where about 80% of the catalyst is found due to the more sluggish kinetics of the oxygen reduction reaction (ORR) [4, 10]. Another approach taken was to develop PGM-free electrocatalysts to completely replace Pt with cheap, Earth-abundant materials. In this quest, non-PGM electrocatalysts have significantly improved towards ORR in the last decade. A lot of these electrocatalysts use Co, Fe, Ni, Mn, etc. in metal organic frameworks (MOFs) mostly, but other structures have also been studied [11]. In general, transition metals oxides (TMOs) have recently attracted a lot of attention because of their low cost and their variable oxidation states (OS) which combined with high electrical conductivity gives them interesting chemical and physical properties [10, 12–14]. Among these specific characteristics we can find a broad range of crystal structures with their accompanying metal oxidation state, electronic configuration and magnetic properties, all

of which are fundamentally interesting to understand in order to rationally design new, more efficient electrocatalysts.

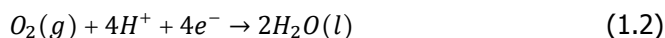
In this thesis I will deal with this side of research where I aim to contribute some fundamental insights on a non-PGM material, i.e. *spinel* LiMn_2O_4 -based electrocatalyst for PEMFC, and its working principle as a Hydrogen Oxidation (HOR) and Oxygen Reduction (ORR) electrocatalyst. In addition to that, part of this thesis will deal with fuel cells in a more "macroscale" viewpoint. There is still a wide gap when translating intrinsic activity of the catalytic materials into membrane-electrode assemblies (MEAs) and a complete fuel cell. This has to do with the traditional methods employed to screen new materials, which are typically not representative of a real-world fuel cell, e.g. liquid electrolyte vs. polymer electrolyte. To this end, interfacial effects in a PEMFC have been studied by means of mass and charge transport where we show that losses in this small area of a cell are the most significant and where most effort should go to apart from new materials as catalyts.

1.1. The PEM fuel cell

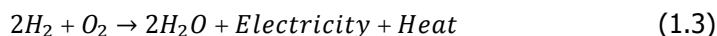
In a PEMFC hydrogen and oxygen are converted into water and electric work. The hydrogen oxidation reaction (HOR) takes place at the anode surface and can be written as:



while at the cathode surface the oxygen reduction reaction (ORR) takes place:



The overall reaction of PEMFCs can simply be described as hydrogen reacting with oxygen to generate water, electricity and heat:



A schematic representation of a PEMFC is shown in figure 1.4. Here, the polymer electrolyte membrane (PEM) has the functions of separating the anode and cathode as well as providing proton conduction pathways from one side to the other. The most common material used for this purpose is Nafion® (by DuPont), a proton conducting polymer that consists of a tetrafluoroethylene (TFE) backbone and perfluoroalkyl ether (PFA) side chains terminated in sulfonic acid groups. These type of polymers combine the hydrophobicity of the backbone with the high hydrophilicity of the sulfonic acid functional group in one macromolecule. This results in a microphase separation of the hydrophobic and hydrophilic domains with the sulfonic acid groups aggregating to form a network of hydrophilic domains that are hydrated upon absorption of water. As water is absorbed into Nafion, the hydrophilic domains swell and restructure giving way to the dissociation of protons from their counter ions .i.e. $-\text{SO}_3^-$ groups) and subsequently become solvated and mobilized by hydration water. It is, therefore, within this domain that the transport of water and protons occur [15, 16].

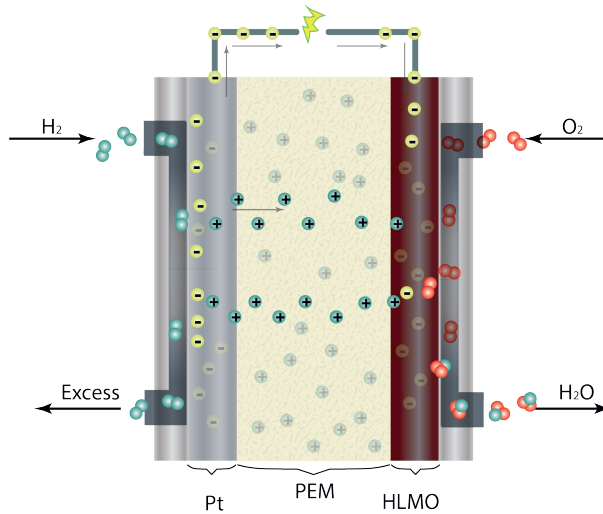


Figure 1.4: Schematic representation of a PEMFC.

In general, during operation hydrogen gas and air are fed into the anode and cathode gas flow channels (GFCs). Hydrogen and oxygen diffuse to the respective catalyst layer via the gas diffusion layers (GDLs). The theoretical maximum efficiency is defined by the ratio between the Gibbs free energy change (ΔG) and enthalpy change (ΔH).

$$\eta_{FC,max} = \frac{\Delta G}{\Delta H} \quad (1.4)$$

Under standard conditions, $\Delta G = -237.145 \text{ kJ/mol}$ and $\Delta H = -285.83 \text{ kJ/mol}$, making the theoretical maximum efficiency of a fuel cell about 83%. On the other hand, a heat engine is limited by the carnot cycle

$$\eta_{Carnot} = 1 - \frac{T_L}{T_H} \quad (1.5)$$

where T_L and T_H denote the low and high temperature of the two reservoirs, respectively. In conventional automobiles, Otto and diesel engines have efficiencies lower than the Carnot cycle and depend on the engine configuration [11]. In practice, Otto or diesel engines reach an efficiency of $\sim 30\text{-}35\%$.

Since PEMFCs are electrochemical devices, they directly produce electrical power and voltage. The created potential of the electrochemical cell depends on the concentrations or partial pressures of the participating species and can be described by the Nernst equation:

$$E = E^0 + \frac{RT}{2F} \ln\left(\frac{a_{H_2} a_{O_2}^{1/2}}{a_{H_2O}}\right) \quad (1.6)$$

where $E^0 = -\frac{\Delta G^0}{zF}$ with z the number of electrons transferred and F is Faraday's constant. R is the universal gas constant; and a_i reflects the activity of species i , and is equal to p_i/p_0 for gases, C_i/C_0 for solutions, and equals unity for pure substances such as water. However, during operation a voltage drop occurs due to an overpotential to ensure the output current. This overpotential is a result of electrode activation (ΔV_{ac}), electrolyte resistance (ΔV_{Ω}) and mass transport limitations (ΔV_{trans}). Thus, the real output voltage of a PEMFC can be written as:

$$V_{FC} = E - \frac{RT}{2\alpha F} \log i^* - \Delta V_{act} - \Delta V_{\Omega} - \Delta V_{trans} \quad (1.7)$$

where i^* is the cross-over current and α is the transfer coefficient. Thus, the operating efficiency of a PEMFC can be written as:

$$\eta_{FC} = \frac{V_{FC}}{E} \quad (1.8)$$

For vehicles, PEMFC efficiency is targeted at $\sim 60\%$ or higher, thus the operating voltage should be around 0.6-0.8 V.

1.2. Alternative materials

In the search for alternative materials, transition metal oxides (TMOs) have gained a lot of attention recently in the field of PEM electrolysers (PEMEC) and PEMFC electrocatalysis [12, 17–21]. The use of metal oxides (MOs) as electrodes for energy conversion is very old, going back to the 1850s where mainly lead and manganese dioxides were studied in the early days [22]. Electrochemical applications distinguish two approaches: a) the use of MOs as charge storage materials, i.e. in primary or secondary batteries, or b) MOs used as electrocatalysts either converting chemical energy into electricity or vice versa. Development of the latter application has lagged behind its energy storage counterpart and research on these materials as electrocatalyst has only gained more attention in the last few decades [22]. In the 1990s, electronic properties of metals started to be related to their chemical reactivity. Since then, d-band theory has been used to describe bond formation on TMO surfaces which have different filling of the d-band [23].

One of the main areas of research of TMOs is in the field of water splitting. The splitting of water using only sunlight is considered the holy grail of chemistry. In nature, there is such a system known as the water oxidizing centre (WOC) of Photosystem II, where a Mn_4CaO_x cluster is responsible for water oxidation. It is also well known that this system is preserved in all oxygenic photosynthetic organisms [17]. Thus, the unique role of manganese in this system has sparked a lot of curiosity in the search for new catalytic materials inspired by Nature's own creations. As a result, a lot of attempts to mimic the WOC's functionality have been done [17, 18, 24, 25].

It is not surprising then, that TMOs have been of interest for a long time as heterogeneous water oxidation catalysts, among which RuO_2 and IrO_2 are known to be highly active although quite expensive. On the other hand, among non-PGM active metal oxides, several metals in different crystal structures have been studied, e.g. *spinel*-types based on Co, Ni or Mn, perovskites with different metal centres, e.g. Co, Ni and La and MOFs [12, 13, 18, 19, 26, 26–31]. The unique property that makes TMOs so versatile in catalysis is the presence of variable oxidation states [13].

Conversely, in fuel cell applications research of these promising type of materials is rather limited. Electrocatalysts based on Mn such as MnO_2 , Mn_3O_4 *spinel* types, Ni or Co based, e.g. NiCo_2O_4 , and La-based oxides have all been studied for fuel cell applications [19], however, most research focuses on alkaline conditions or neutral conditions, whereas attention for acidic electrolytes is lacking in the literature.

In alkaline environments, however, TMOs with *spinel* crystal structure have been shown as proficient electrocatalysts for fuel cells [13]. Among *spinel*-types, manganese oxides, cobalt oxides, copper oxides and iron oxides can be found in the literature for ORR in alkaline solutions [12, 13, 32].

Manganese oxides are especially attractive as they reunite several desired characteristics for catalysis: they are abundant, have low toxicity, and a multivalent nature that gives them a lot of structural diversity (see figure 1.5)[31]. For instance, manganese oxides in different crystal structures have been extensively studied as catalysts in many different applications, e.g. in the conversion of CO , NO_x , SO_x and other volatile organic compounds, decomposition of ozone and hydrogen peroxides, organic reduction and oxidation, removal of bacterial pathogens, epoxidation of olefins, photo-/electrochromics and oxygen evolution and reduction reactions (OER and ORR) [12, 14, 20, 32–35]. More specifically, in terms of ORR activity MnO , MnO_2 , Mn_3O_4 , MnOOH , Mn_2O_3 and Mn_5O_8 have all been shown to be highly active in alkaline conditions [29, 31, 32, 35, 36]. Furthermore, research on alkaline media often suggests that active materials allow reversible proton insertion and various manganese oxides have been studied in that respect, e.g. Mn_2O_3 , Mn_3O_4 , and MnO_2 [14, 34, 35]. Particularly manganese oxides in cubic crystal structures such as *spinel* manganese oxides have been shown as promising alternatives for ORR in alkaline conditions [10, 12–14, 32, 37, 38]. This cubic *spinel* class of materials with formula AMn_2O_4 have been shown to be more catalytically active than their tetragonal counterparts as they have better affinity towards oxygen adsorption as well as higher density of active sites [10, 37].

In addition, *spinel*-types based on Mn have been identified as highly active towards ORR [32] in comparison with other structures or phases such as $\alpha\text{-MnO}_2$, $\beta\text{-MnO}_2$, $\gamma\text{-MnO}_2$, $\lambda\text{-MnO}_2$, perovskites, layered, tunneled, etc [29]. For example, it has been shown that *spinel* LiMn_2O_4 becomes active only when removing Li from its structure [27]. However, despite their historic potential as catalysts to ORR and OER in alkaline and neutral conditions in e.g. metal-air batteries [40–44], alkaline fuel cells [31, 41, 44], microbial fuel cells [40, 44] and electrolyzers [31, 45, 46], research on manganese oxides as catalysts in PEMFCs has been rather limited.

It could be presumed that the lack of documentation about MnOs in acidic media

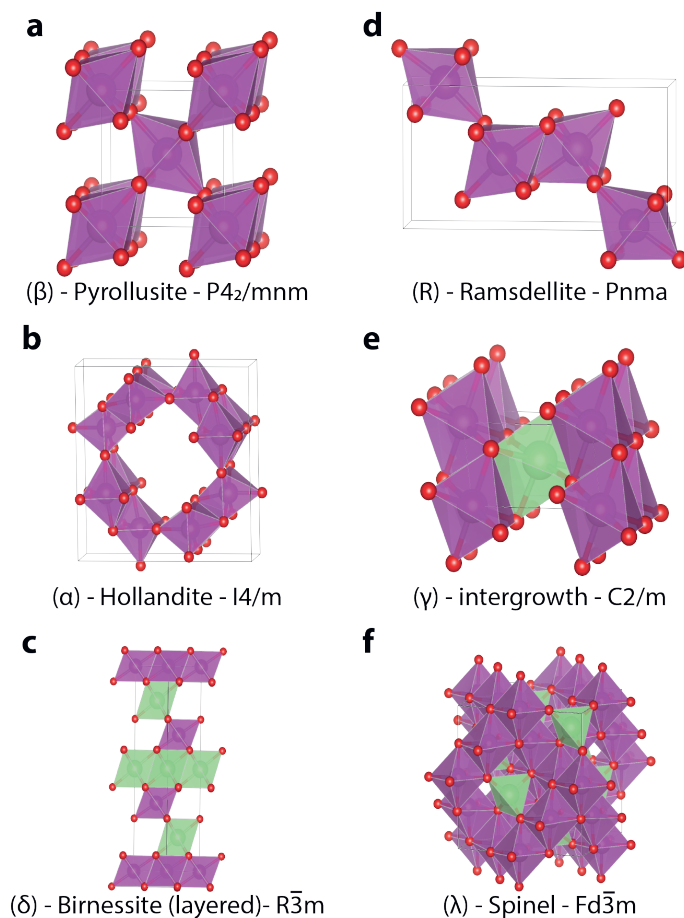


Figure 1.5: Examples of some manganese oxide polymorphs.

is due to manganese's thermodynamic instability at low pH values as predicted by Pourbaix [47]. However, in the last few years the stabilization of TMOs against corrosion in acidic conditions for PEM electrolyzers has become more prominent, with a few suggestions already found in the literature for manganese oxides, e.g. addition of titanium oxide or doping with fluorine [19, 46, 48]. Additionally, it has been suggested that these materials can be activated to function as catalysts in acidic environments by exploiting a self-healing process that consists of oxidative electrodeposition of dissolved Mn ions [49]. These findings, though in early stages, open up the possibility of engineering Earth abundant TMOs in order to use them as catalysts in acidic environments.

In this thesis, a spinel-type LiMn_2O_4 will be studied as a novel electrocatalyst for HOR and ORR in PEMFC applications.

1.2.1. Spinel LiMn_2O_4

Spinel is a class of minerals with general formula AB_2X_4 where X is an anion (typically oxygen or sulfur). This system crystallises in a cubic system that is arranged in a cubic close-packed lattice with cations A and B occupying some of the tetrahedral and octahedral sites in the lattice. The majority of spinel compounds belong to space group $Fd\bar{3}m$ (No. 227 in international tables). There are 8 formula units per cubic cell, where there are 32 anions and 24 cations. Table 1.1 lists the various lattice sites denoted using Wyckoff notation [50].

Table 1.1: Wyckoff positions of group $Fd\bar{3}m$ (No. 227).

Multiplicity	Wyckoff letter	Site symmetry
8	a	-43m
8	b	-43m
16	c	..3m
16	d	..3m
32	e	..3m
48	f	2..m m
96	g	..m
96	h	..2
192	i	1

In spinel LiMn_2O_4 (LMO) Li cations are found in the 8a tetrahedral sites and Mn atoms in 16d octahedral sites, both coordinated with oxygen anions (32e sites). In figure 1.6 a schematic representation of spinel LMO is shown. Furthermore, there are 96 interstices between the anions in the cubic unit cell.

In this thesis, a series of advanced spectroscopic techniques such as X-ray absorption spectroscopy (XAS), neutron diffraction (ND) and solid-state nuclear magnetic resonance (ss-NMR), have been used to probe the crystal structure of the materials studied and the changes induced on them in order to activate them as electrocatalysts for the oxygen reduction (ORR) and Hydrogen Oxidation (HOR) reactions.

1.3. Electrocatalysis

A catalytic process that involves electron transfer as oxidation and reduction reactions at the interface between an electrolyte and an electrode is a sub-field known as electrocatalysis. Electrocatalysts are materials that lower the overpotential of these reactions and can accomplish this through different reaction pathways that are ruled by thermodynamic potentials [51–53]. A good electrocatalyst can minimize the overpotential required for driving a specific electrochemical reaction. This depends on electrode material, reactants, products and intermediates at the interphase electrode-electrolyte. The aim is to improve the reaction rate, i.e. the generated electrical current. This can be achieved by lowering the activation energy of the target reaction by the formation of intermediate bonds between the compound and the electrode. Metrics to compare electrocatalysts include the pro-

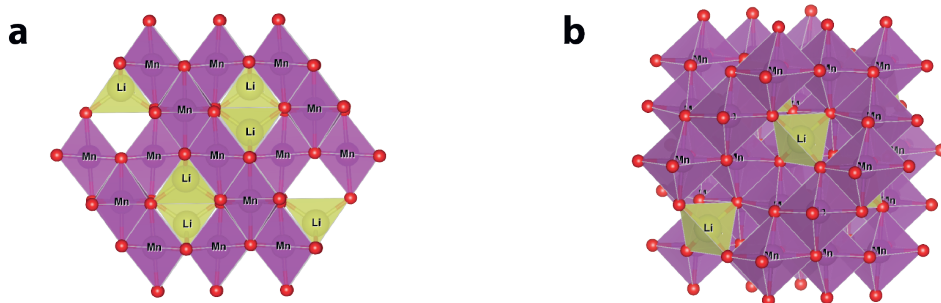


Figure 1.6: Spinel LMO from two different points of view. Mn: octahedral centres. Li: tetrahedral centres. O: corners (in red).

duced electrical current at a given applied potential.

The most commonly used techniques are steady-state polarization, cyclic voltammetry, rotating disk electrode (RDE) and rotating ring-disk electrode (RRDE). In a three-electrode cell or half cell, identification of phenomena occurring at a single interface is possible. The set-up consists of a working electrode (where the interface being studied is), a counter electrode and a reference electrode. Voltammetry is the most common experiment in dynamic electrochemistry. Here, the potential at the working electrode interface is varied in time and the current response is recorded. Different voltammetry techniques are common such as cyclic voltammetry (CV), linear sweep voltammetry (LSV) and hydrodynamic sweep voltammetry (HSV) [54].

In CV scans are performed varying the potential back and forth and recording the current response. This is typically the first experiment performed by electrochemists when evaluating a new system. On the other hand, LSVs are typically performed in only one direction, either oxidation or reaction and it is done where a surface needs to be assessed without its regeneration in the backward scan. CVs and LSVs yield important information about electrocatalytic properties of materials such as the onset potential, half-wave potential, diffusion coefficient of reactants, oxidation, dissolution of the material, as well as determination of the electrochemically active surface area (ECSA) [13, 54, 55]

However, these techniques are limited by mass transport of the reactants towards the surface of the electrode. In this case, controlling mass transport conditions can be useful in understanding reaction mechanisms. Hydrodynamic voltammetry makes use of the RDE technique, where a disk electrode is embedded in a non-conductive cylinder. This cylinder can then be rotated at varying rates. The rotation rate is directly related to the thickness of the product layer formed at the electrode surface and that blocks diffusion of fresh reactant. The disk rotation results in a centrifugal force that pushes electrolyte away from the centre of the electrode in the radial direction and a liquid movement from the bulk of the electrolyte to the electrode surface, thus refreshing reactants at the surface. Rotation

rate is related to the mass limited current by the Koutecky-Levich equation [56]:

$$\frac{1}{j} = \frac{1}{j_l} + \frac{1}{j_k} \quad (1.9)$$

where j is the measured current density, j_l is the Levich current density and j_k is the kinetic current density. The Levich current density is given by equation:

$$j_l = 0.62nFD^{2/3}\omega^{1/2}\nu^{-1/6}C \quad (1.10)$$

where D is the diffusion coefficient of the reactant in the electrolyte, ω is the rotation rate, ν is the electrolyte's kinematic viscosity and C the reactant's concentration. This equation allows the determination of the kinetic current density at a given overpotential and has been used to determine electrocatalytic parameters [54].

In this work, several electrochemistry techniques have been used to study electrocatalytic and electrochemical properties of the systems under investigation. Electrochemical activity to ORR has been assessed by means of the RDE technique and different materials have been compared using their onset potential.

1.4. Outlook of this thesis

In the next chapters, several aspects of PEM fuel cells will be discussed. From a "macro" point of view, i.e. transport properties in a cell, down to atomic and mechanistic insights on the relevant reactions.

Chapter 2 will discuss the ambiguity found in the literature when discussing transport properties. We emphasize that the intrinsic values of these properties cannot be properly discussed unless interfacial effects are taken into account. We propose an approach based on non-equilibrium thermodynamics in order to disentangle interface from bulk contributions to these properties. We do a demonstration exercise with values for different properties taken from the literature, where we show that the discrepancy found across different measuring techniques is due to the interfaces formed during measurements.

Chapter 3 will dig further into interfacial effects on mass transport. Here, water transport in a half MEA has been studied through water sorption experiments. We demonstrate how the lag in water sorption of the membrane, i.e. non-Fickian behaviour, is due to interfacial effects, where at smaller scales resistance to water transport increases due to several factors, i.e. confinement effects, rearrangement of the polymer at the surface, etc.

From here on, we will devote the remaining chapters of this thesis to the study of a novel electrocatalyst based on a spinel lithium manganate for PEM fuel cell applications.

Chapter 4 will describe the proposed electrocatalysts. We propose that proton insertion in a spinel LiMn_2O_4 can make it active towards ORR and HOR. In this chapter we describe the synthesis methods and proton insertion. We study the crystal structure, confirm protonation and its mechanism using neutron diffraction

and solid-state NMR techniques. We finalize by studying the electrocatalytic activity of these materials towards ORR and hypothesize on the possible reasons for increased reactivity based on the results obtained from all the different techniques.

Chapter 5 will continue on the study of protonated LMOs as electrocatalysts. Here, the materials are tested in an actual fuel cell and *operando* x-ray absorption measurements are used to elucidate the role of Mn in catalysis as well as the indirect role of protons or other species. We discuss changes in Mn oxidation state during operation as a HOR or ORR electrocatalyst. The combination of structural and chemical parameters allows drawing hypotheses on the particular combination of parameters in order to optimise these materials so that they are active towards one or the other reaction.

The results shown in this thesis open new pathways in the discussion of fuel cells in the community based on the effect of interfaces that cannot be neglected. At the same time it offers interesting insights on the physical and chemical properties of electrocatalytic materials while suggesting a novel bi-functional electrocatalyst in the field based on a cheap and abundant material, in contrast with the current choice of platinum-group metals.

References

- [1] H. Ritchie and M. Roser, "Energy," *Our World in Data*, 2020. <https://ourworldindata.org/energy>.
- [2] H. R. Max Roser and E. Ortiz-Ospina, "World population growth," *Our World in Data*, 2013. <https://ourworldindata.org/world-population-growth>.
- [3] M. Liakopoulou, "Towards an EU Hydrogen Economy : Policy and Energy Security Perspectives Towards an EU Hydrogen Economy ;," no. November, 2020.
- [4] L. Du, V. Prabhakaran, X. Xie, S. Park, Y. Wang, and Y. Shao, "Low-PGM and PGM-Free Catalysts for Proton Exchange Membrane Fuel Cells: Stability Challenges and Material Solutions," *Advanced Materials*, vol. 33, no. 6, pp. 1–18, 2021.
- [5] D. Sperling and J. Cannon, *The Hydrogen Energy Transition: Cutting Carbon from Transportation*. Elsevier Science & Technology, 2004.
- [6] A. Jadhav, "Hydrogen Fuel Cell Vehicle Market," tech. rep., 2020.
- [7] N. Sazali, W. N. W. Salleh, A. S. Jamaludin, and M. N. M. Razali, "New perspectives on fuel cell technology: A brief review," *Membranes*, vol. 10, no. 5, 2020.
- [8] D. Wu, C. Peng, C. Yin, and H. Tang, "Review of System Integration and Control of Proton Exchange Membrane Fuel Cells," *Electrochemical Energy Reviews*, vol. 3, no. 3, pp. 466–505, 2020.

- [9] S. T. Thompson, B. D. James, J. M. Huya-Kouadio, C. Houchins, D. A. DeSantis, R. Ahluwalia, A. R. Wilson, G. Kleen, and D. Papageorgopoulos, "Direct hydrogen fuel cell electric vehicle cost analysis: System and high-volume manufacturing description, validation, and outlook," *Journal of Power Sources*, vol. 399, no. July, pp. 304–313, 2018.
- [10] Z. Xia, L. An, P. Chen, and D. Xia, "Non-Pt Nanostructured Catalysts for Oxygen Reduction Reaction: Synthesis, Catalytic Activity and its Key Factors," *Advanced Energy Materials*, vol. 6, no. 17, pp. 1–29, 2016.
- [11] Y. Wang, H. Yuan, A. Martinez, P. Hong, H. Xu, and F. R. Bockmiller, "Polymer electrolyte membrane fuel cell and hydrogen station networks for automobiles: Status, technology, and perspectives," *Advances in Applied Energy*, vol. 2, p. 100011, may 2021.
- [12] C. Wei, Z. Feng, G. G. Scherer, J. Barber, Y. Shao-Horn, and Z. J. Xu, "Cations in Octahedral Sites: A Descriptor for Oxygen Electrocatalysis on Transition-Metal Spinels," *Advanced Materials*, vol. 29, no. 23, pp. 1–8, 2017.
- [13] C. Goswami, K. K. Hazarika, and P. Bharali, "Transition metal oxide nanocatalysts for oxygen reduction reaction," *Materials Science for Energy Technologies*, vol. 1, no. 2, pp. 117–128, 2018.
- [14] K. K. Hazarika, C. Goswami, H. Saikia, B. J. Borah, and P. Bharali, "Cubic Mn₂O₃ nanoparticles on carbon as bifunctional electrocatalyst for oxygen reduction and oxygen evolution reactions," *Molecular Catalysis*, vol. 451, pp. 153–160, 2018.
- [15] K.-D. Kreuer, S. J. Paddison, E. Spohr, and M. Schuster, "Transport in Proton Conductors for Fuel-Cell Applications," *Chemical Reviews*, vol. 104, no. 10, pp. 4637–4678, 2004.
- [16] Q. Zhao, P. Majsztrik, and J. Benziger, "Diffusion and interfacial transport of water in Nafion," *Journal of Physical Chemistry B*, vol. 115, no. 12, pp. 2717–2727, 2011.
- [17] R. K. Hocking, R. Brimblecombe, L. Y. Chang, A. Singh, M. H. Cheah, C. Glover, W. H. Casey, and L. Spiccia, "Water-oxidation catalysis by manganese in a geochemical-like cycle," *Nature Chemistry*, vol. 3, no. 6, pp. 461–466, 2011.
- [18] A. Bergmann, I. Zaharieva, H. Dau, and P. Strasser, "Electrochemical water splitting by layered and 3D cross-linked manganese oxides: Correlating structural motifs and catalytic activity," *Energy and Environmental Science*, vol. 6, no. 9, pp. 2745–2755, 2013.
- [19] P. P. Patel, M. K. Datta, O. I. Velikokhatnyi, R. Kuruba, K. Damodaran, P. Jampani, B. Gattu, P. M. Shanthi, S. S. Damle, and P. N. Kumta, "Noble metal-free bifunctional oxygen evolution and oxygen reduction acidic media electrocatalysts," *Scientific Reports*, vol. 6, no. February, pp. 1–14, 2016.

- [20] S. Ghosh, P. Kar, N. Bhandary, S. Basu, T. Maiyalagan, S. Sardar, and S. K. Pal, "Reduced graphene oxide supported hierarchical flower like manganese oxide as efficient electrocatalysts toward reduction and evolution of oxygen," *International Journal of Hydrogen Energy*, vol. 42, no. 7, pp. 4111–4122, 2017.
- [21] A. Bonnefont, A. S. Ryabova, T. Schott, G. Kéranguéven, S. Y. Istomin, E. V. Antipov, and E. R. Savinova, "Challenges in the understanding oxygen reduction electrocatalysis on transition metal oxides," *Current Opinion in Electrochemistry*, vol. 14, pp. 23–31, 2019.
- [22] J. P. Brenet, "Electrochemical behaviour of metallic oxides," *Journal of Power Sources*, vol. 4, no. 3, pp. 183–190, 1979.
- [23] Z. J. Zhao, S. Liu, S. Zha, D. Cheng, F. Studt, G. Henkelman, and J. Gong, "Theory-guided design of catalytic materials using scaling relationships and reactivity descriptors," *Nature Reviews Materials*, vol. 4, no. 12, pp. 792–804, 2019.
- [24] D. G. Nocera, "The artificial leaf," *Accounts of Chemical Research*, vol. 45, no. 5, pp. 767–776, 2012.
- [25] S. Y. Reece, J. A. Hamel, K. Sung, T. D. Jarvi, A. J. Esswein, J. J. Pijpers, and D. G. Nocera, "Wireless solar water splitting using silicon-based semiconductors and earth-abundant catalysts," *Science*, vol. 334, no. 6056, pp. 645–648, 2011.
- [26] J. Suntivich, H. A. Gasteiger, N. Yabuuchi, and Y. Shao-Horn, "Electrocatalytic measurement methodology of oxide catalysts using a thin-film rotating disk electrode," *Journal of the Electrochemical Society*, vol. 157, no. 8, 2010.
- [27] D. M. Robinson, Y. B. Go, M. Mui, G. Gardner, Z. Zhang, D. Mastrogiovanni, E. Garfunkel, J. Li, M. Greenblatt, and G. C. Dismukes, "Photochemical water oxidation by crystalline polymorphs of manganese oxides: Structural requirements for catalysis," *Journal of the American Chemical Society*, vol. 135, no. 9, pp. 3494–3501, 2013.
- [28] G. R. Mirshekari and A. P. Shirvanian, "Electrochemical behavior of titanium oxide nanoparticles for oxygen reduction reaction environment in PEM fuel cells," *Materials Today Energy*, vol. 9, no. 8, pp. 235–239, 2018.
- [29] K. A. Stoerzinger, M. Risch, B. Han, and Y. Shao-Horn, "Recent Insights into Manganese Oxides in Catalyzing Oxygen Reduction Kinetics," *ACS Catalysis*, vol. 5, no. 10, pp. 6021–6031, 2015.
- [30] A. Ramírez, P. Hillebrand, D. Stellmach, M. M. May, P. Bogdanoff, and S. Fiechter, "Evaluation of MnOx, Mn2O3, and Mn 3O4 electrodeposited films for the oxygen evolution reaction of water," *Journal of Physical Chemistry C*, vol. 118, no. 26, pp. 14073–14081, 2014.

- [31] I. M. Mosa, S. Biswas, A. M. El-Sawy, V. Botu, C. Guild, W. Song, R. Ramprasad, J. F. Rusling, and S. L. Suib, "Tunable mesoporous manganese oxide for high performance oxygen reduction and evolution reactions," *Journal of Materials Chemistry A*, vol. 4, no. 2, pp. 620–631, 2015.
- [32] Y. Nie, L. Li, and Z. Wei, "Recent advancements in Pt and Pt-free catalysts for oxygen reduction reaction," *Chemical Society Reviews*, vol. 44, no. 8, pp. 2168–2201, 2015.
- [33] A. Harriman, I. J. Pickering, J. M. Thomas, and P. A. Christensen, "Metal oxides as heterogeneous catalysts for oxygen evolution under photochemical conditions," *Journal of the Chemical Society, Faraday Transactions 1: Physical Chemistry in Condensed Phases*, vol. 84, no. 8, pp. 2795–2806, 1988.
- [34] I. Zaharieva, P. Chernev, M. Risch, K. Klingan, M. Kohlhoff, A. Fischer, and H. Dau, "Electrosynthesis, functional, and structural characterization of a water-oxidizing manganese oxide," *Energy and Environmental Science*, vol. 5, no. 5, pp. 7081–7089, 2012.
- [35] C. Ottone, M. Armandi, S. Hernández, S. Bensaid, M. Fontana, C. F. Pirri, G. Saracco, E. Garrone, and B. Bonelli, "Effect of surface area on the rate of photocatalytic water oxidation as promoted by different manganese oxides," *Chemical Engineering Journal*, vol. 278, pp. 36–45, 2015.
- [36] F. H. Lima, M. L. Calegaro, and E. A. Ticianelli, "Investigations of the catalytic properties of manganese oxides for the oxygen reduction reaction in alkaline media," *Journal of Electroanalytical Chemistry*, vol. 590, no. 2, pp. 152–160, 2006.
- [37] F. Cheng, J. Shen, B. Peng, Y. Pan, Z. Tao, and J. Chen, "Rapid room-temperature synthesis of nanocrystalline spinels as oxygen reduction and evolution electrocatalysts," *Nature Chemistry*, vol. 3, no. 1, pp. 79–84, 2011.
- [38] M. Risch, K. A. Stoerzinger, B. Han, T. Z. Regier, D. Peak, S. Y. Sayed, C. Wei, Z. Xu, and Y. Shao-Horn, "Redox Processes of Manganese Oxide in Catalyzing Oxygen Evolution and Reduction: An in Situ Soft X-ray Absorption Spectroscopy Study," *Journal of Physical Chemistry C*, vol. 121, no. 33, pp. 17682–17692, 2017.
- [39] S. K. Ghosh, "Diversity in the family of manganese oxides at the nanoscale: from fundamentals to applications," *ACS omega*, vol. 5, no. 40, pp. 25493–25504, 2020.
- [40] I. Roche, E. Chaînet, M. Chatenet, and J. Vondrák, "Carbon-supported manganese oxide nanoparticles as electrocatalysts for the Oxygen Reduction Reaction (ORR) in alkaline medium: Physical characterizations and ORR mechanism," *Journal of Physical Chemistry C*, vol. 111, no. 3, pp. 1434–1443, 2007.

- [41] J. Vondrák, B. Klápště, J. Velická, M. Sedlaříková, V. Novák, and J. Reiter, "Carbon/manganese oxide based fuel cell electrocatalyst using "flywheel" principle," *Journal of New Materials for Electrochemical Systems*, vol. 8, no. 1, pp. 1–4, 2005.
- [42] A. Flegler, S. Hartmann, H. Weinrich, M. Kapuschinski, J. Settelein, H. Lormann, and G. Sextl, "Manganese Oxide Coated Carbon Materials as Hybrid Catalysts for the Application in Primary Aqueous Metal-Air Batteries," *C*, vol. 2, no. 1, p. 4, 2016.
- [43] S. J. Venkata, G. A., and R. K., "Morphological and structural analysis of manganese oxide nanoflowers prepared under different reaction conditions," *Applied Surface Science*, vol. 449, pp. 228–232, aug 2018.
- [44] Y. Dessie, S. Tadesse, R. Eswaramoorthy, and B. Abebe, "Recent developments in manganese oxide based nanomaterials with oxygen reduction reaction functionalities for energy conversion and storage applications: A review," *Journal of Science: Advanced Materials and Devices*, vol. 4, no. 3, pp. 353–369, 2019.
- [45] H. Antoni, D. M. Morales, Q. Fu, Y. T. Chen, J. Masa, W. Schuhmann, and M. Muhler, "Oxidative Deposition of Manganese Oxide Nanosheets on Nitrogen-Functionalized Carbon Nanotubes Applied in the Alkaline Oxygen Evolution Reaction," *ACS Omega*, vol. 3, no. 9, pp. 11216–11226, 2018.
- [46] T. Hayashi, N. Bonnet-Mercier, A. Yamaguchi, K. Suetsugu, and R. Nakamura, "Electrochemical characterization of manganese oxides as a water oxidation catalyst in proton exchange membrane electrolyzers," *Royal Society Open Science*, vol. 6, no. 5, 2019.
- [47] M. Pourbaix, *Thermodynamique des solutions aqueuses diluées. Représentation graphique du rôle du pH et du potentiel*. 1945.
- [48] R. Frydendal, E. A. Paoli, I. Chorkendorff, J. Rossmeisl, and I. E. Stephens, "Toward an Active and Stable Catalyst for Oxygen Evolution in Acidic Media: Ti-Stabilized MnO₂," *Advanced Energy Materials*, vol. 5, no. 22, 2015.
- [49] M. Huynh, C. Shi, S. J. Billinge, and D. G. Nocera, "Nature of Activated Manganese Oxide for Oxygen Evolution," *Journal of the American Chemical Society*, vol. 137, no. 47, pp. 14887–14904, 2015.
- [50] K. E. Sickafus, J. M. Wills, and N. W. Grimes, "Structure of spinel," *Journal of the American Ceramic Society*, vol. 82, no. 12, pp. 3279–3292, 1999.
- [51] R. Li and C. Li, "Photocatalytic Water Splitting on Semiconductor-Based Photocatalysts," pp. 1–57, 2017.
- [52] A. Groß, "Computational Modeling of Electrocatalytic Reactions," in *Encyclopedia of Interfacial Chemistry*, pp. 455–465, Elsevier, 2018.

- [53] R. Cardaña, B. Cercado, and G. Buitrón, "Microbial Electrolysis Cell for Biohydrogen Production," *Biohydrogen*, pp. 159–185, 2019.
- [54] A. Lavacchi, H. Miller, and F. Vizza, *Supported Metal Nanoparticles*. 2013.
- [55] C. Song and J. Zhang, "Electrocatalytic oxygen reduction reaction," *PEM Fuel Cell Electrocatalysts and Catalyst Layers: Fundamentals and Applications*, pp. 89–134, 2008.
- [56] A. J. Bard and L. R. Faulkner, *Electrochemical methods: Fundamentals and applications*. John Wiley & Sons, Inc., 2001.

2

A systematic non-equilibrium approach to transport in PEM fuel cells

What happens but once may have not happened at all.

Milan Kundera, *The Unbearable Lightness of Being*

We hypothesize that the properties of proton-exchange membranes for fuel cell applications cannot be described unambiguously unless interface effects are taken into account. In order to prove this, we first develop a thermodynamically consistent description of the transport properties in the membranes, both for a homogeneous membrane and for a homogeneous membrane with two surface layers in contact with the electrodes or holder material. For each subsystem, homogeneous membrane, and the two surface layers, we limit ourselves to four parameters as the system as a whole is considered to be isothermal. We subsequently analyse the experimental results on some standard membranes that have appeared in the literature and analyse these using the two different descriptions. This analysis yields relatively well-defined values for the homogeneous membrane parameters and estimates for those of the surface layers and hence supports our hypothesis. As demonstrated, the method used here allows for a critical evaluation of the literature values. Moreover, it allows optimization of stacked transport systems such as proton-exchange membrane fuel cell units where interfacial layers, such as that between the catalyst and membrane, are taken into account systematically.

Parts of this chapter have been published in *Materials* **10**, 6 (2017) [1].

2.1. Introduction

Proton-conducting, polymer electrolyte membranes (PEM), play an important role in fuel cell applications as they serve not only the function of separation between the anode and cathode sides, but also act as a solid electrolyte allowing the transport of charge. The most common material used for these applications is Nafion™ (DuPont, Wilmington, DE, USA), which consists of a tetrafluoroethylene (TFE) backbone and perfluoroalkyl ether (PFA) side chains terminated in sulfonic acid groups [2, 3]. The combination of the hydrophobicity of the backbone with the hydrophilicity of the sulfonic acid functional group in one macromolecule confers Nafion™ the properties necessary for this application.

Given the evident importance of PEM membranes, a plethora of studies on their different properties has been done over the last few decades. However, it proves difficult to reach a consensus on their meaning as research aimed at understanding the underlying phenomena describing the behaviour of membrane properties is performed in many different ways and under different conditions which often do not match the reality of a membrane in an operating fuel cell. Within this framework, and from the very intrinsic interest in membrane performance, it would be advantageous to have a systematic approach for assessment that facilitates description and posterior optimization of the technology.

A powerful tool to study systems that are not in global equilibrium, such as electrochemical systems, is non-equilibrium thermodynamics (NET). This approach consists of a reformulation of the second law of thermodynamics in terms of entropy production [4]. In this formulation, originally proposed by Onsager [11], the entropy production is given by the product sum of conjugate fluxes, J_i , and forces, X_i , in the system. In his theory, each flux is defined as a linear combination of all forces related by a coefficient L_{ij} . Onsager later proved that the relations between these coefficients were reciprocal: $L_{ij} = L_{ji}$. These coefficients are also known as Onsager's coefficients. (See next section).

This theory provides a more accurate description of transport in systems where pressure, concentration, and temperature gradients exist as it also includes the coupling between these processes. Furthermore, it quantifies the entropy, or lost work, that is produced during transport [5]. The need to design systems that waste less work, such as fuel cells, makes this approach even more appropriate. However, despite the advantages that irreversible thermodynamics can offer, its use has been quite limited [3–6]. Kreuer et al. [3] did impressive work at using this approach to describe membranes for fuel cell applications; they provided an extensive survey on methods from simulation to experimentation and transport mechanisms as understood to the date. However, the formalism they propose is not entirely consistent as the number of independent driving forces has to equal the number of independent fluxes, which is not the case in their approach [3].

Here we present a transport coefficient matrix method (TCM) that allows a systematic approach to the problem and a literature survey of the properties considered meaningful for PEM fuel cell systems. We do so for a Nafion™ 117 type of membrane and our purpose is to demonstrate that the “contact resistance” information can be extracted from bulk values for different membrane properties and that this

information is already available in experiments performed by others although not always accounted for. Solutions to eliminating contact resistances have been presented in earlier works for proton conductivity in bare membranes [29] and for the effect of mass transport at the interfaces on diffusivity and permeability [7, 8]. However, in practice, contact resistances are always present and the values for bare membranes become less meaningful; it is in this scenario that interfacial effects become critical and need to be understood if our goal is to systematically quantify energy losses in a fuel cell as a means to achieve more efficient, cheaper devices. Moreover, the method offers the possibility to extend the study to stacked systems, thus also allowing the assessment of fuel cell stacks and the disentanglement of interfacial effects. Some authors have attempted to study the electrical and mass interfaces [2, 15, 18, 19, 28, 39], but, as with membranes, there is no consensus on the whole picture and these phenomena are not yet fully understood.

2.2. Transport Coefficient Matrix Method (TCM)

Here, we shall model the membrane as a slab of ionomer, component 0, of thickness d and cross sectional area A . Thereby, we shall strictly follow the rules of non-equilibrium thermodynamics as laid down in the monograph of de Groot and Mazur [9] or Kondepudi and Prigogine [10] albeit that we use molar quantities here. The membrane contains water, component 1, and hydrogen, component 2, that pass through the membrane. Due to the water, the ionomer dissociates and protons become available for transport of charge, component 3. This charge transport occurs by means of electrodes at the extremities of the membrane. We fix our frame of reference to the ionomer material of the membrane so that fluxes of water, hydrogen, and charge are transported through the membrane in the direction perpendicular to the surface area. As the ionomer itself is stationary in the frame of reference, the number of components in the system is three: the two neutral species, water and hydrogen, and the charge. Temperature is assumed to be constant so that we will be able to map closely onto the work of Kreuer et al. [3]. As soon as transport takes place through the membrane, dissipation occurs which is quantified by means of the entropy production defined by

$$\dot{S} = \frac{1}{T} \int_V \mathbf{J}\mathbf{X}dV \quad (2.1)$$

where T is the temperature, $\mathbf{J}\mathbf{X}$ the flux-force conjugate, and V is the control volume. The fluxes are organized in a row vector as

$$\mathbf{J} = (J_w, J_h, j) \quad (2.2)$$

with the water flux as the first component, the hydrogen flux as the second component, and the current density as the third component. Likewise, the thermodynamic driving forces are defined by the column vector

$$\mathbf{X} = \begin{pmatrix} -\partial_x \mu_{w,T} \\ -\partial_x \mu_{h,T} \\ -\partial_x \phi \end{pmatrix} \quad (2.3)$$

with the chemical potential gradient of water and hydrogen, both at constant temperature, as the first and second component and the electric field as the third component. The fluxes and the driving forces are coupled and, considering the magnitudes of the driving forces, these may be considered as linear so that a relation exists as

$$\mathbf{J}^T = \mathbf{L}\mathbf{X} \quad (2.4)$$

where \mathbf{L} is the matrix of transport coefficients. Onsager symmetry [11] applies, so that of the nine elements of the matrix, there are only six that are independent. Note that the transformation of the driving forces produces a column vector that is mapped to the fluxes by matrix transposition. The experimentally accessible transport quantities are the volume flux J_V , of liquid water, and of hydrogen J_H . The latter is defined with respect to the aqueous volume rather than to the ionomer. The transformation \mathbf{B} , expressed as $\mathbf{J}' = \mathbf{B}\mathbf{J}$, changes the original flux vector in the new flux vector $\mathbf{J}' = (J_V, J_H, j)$ and has components

$$\mathbf{B} = \begin{pmatrix} V_w & V_h & 0 \\ -c_h V_h / c_w & V_h & 0 \\ 0 & 0 & 1 \end{pmatrix} \quad (2.5)$$

where V_w and V_h are the water and hydrogen volume, respectively; and c_w and $-c_h$ are the concentrations of water and hydrogen. The new thermodynamic variables are, apart from the remaining electric field, the experimentally accessible total pressure gradient and the partial pressure of hydrogen at constant total pressure. The old driving forces can be transferred into the new driving forces using the same transformation, i.e., $\mathbf{X} = \mathbf{B}\mathbf{X}'$ where

$$\mathbf{X}' = \begin{pmatrix} -\partial_x p \\ -\partial_x p_H \\ -\partial_x \phi \end{pmatrix} \quad (2.6)$$

The transformation to new fluxes and forces leaves the entropy production unchanged because $\mathbf{J}\mathbf{X} = \mathbf{J}'\mathbf{B}^{-1}\mathbf{B}\mathbf{X}' = \mathbf{J}'\mathbf{X}'$. The new transport coefficient matrix can be obtained from the old one through $\mathbf{L}' = \mathbf{B}^T\mathbf{L}\mathbf{B}$, and is symmetric because of Onsager symmetry and hence has six elements. It is written as

$$\begin{pmatrix} J_V \\ J_H \\ j \end{pmatrix} = \begin{pmatrix} R_V & 0 & \sigma K \\ 0 & P_H & 0 \\ \sigma K & 0 & \sigma \end{pmatrix} \begin{pmatrix} -\partial_x p \\ -\partial_x p_x \\ -\partial_x \phi \end{pmatrix} \quad (2.7)$$

where R_V and P_H are the water and hydrogen permeabilities through the membrane, respectively; σ is the proton conductivity; and, K is the electro-osmotic drag. The three main coefficients are on the diagonal of the matrix. The first to consider is the permeability defined as the coefficient relating volumetric flow to total pressure gradient, i.e.,

$$R_V = -\frac{J_V}{\partial_x p} \Big|_{\partial_x p_H=0, \partial_x \phi=0} \quad (2.8)$$

Likewise, there is the hydrogen permeability defined by

$$P_H = -\frac{J_H}{\partial_x p_H} \Big|_{\partial_x p=0, \partial_x \phi=0} \quad (2.9)$$

Note that this involves a hydrogen gradient in the absence of a total pressure gradient. The third main coefficient is the electric conductivity, canonically defined as

$$\sigma = -\frac{j}{\partial_x \phi} \Big|_{\partial_x p=0, \partial_x p_H=0} \quad (2.10)$$

The off-diagonal coefficients are known as cross-coefficients in the field of non-equilibrium thermodynamics. Of the three that can be defined, only one is known; the electro-osmotic drag defined as

$$K = -\frac{J_V}{j} \Big|_{\partial_x p=0, \partial_x p_H=0} \quad (2.11)$$

The other two coefficients are assumed to be small [4, 12] and therefore we have taken them to be zero in equation 2.7.

The transport coefficients defined above depend on the temperature and on the water content, apart from more material dependencies such as the porosity of the ionomer. One generally assumes these to be uniform across the membrane volume of the ionomer whereas it is generally known not to be the case [3]. Actually, one only determines averaged values by considering the volumetric flow and electrical current for a whole membrane as a function of the pressure and electric potential drops across the membrane. The values thus obtained are then corrected by the geometrically estimated cross sectional area and thickness.

There is, in general, not enough information available about membrane inhomogeneities to warrant a proper model. The most important inhomogeneities are the surfaces that are in contact with the electrodes or at least with a material to hold the ionomer in place. A well-known phenomenon that falls in this category is the "contact resistance" between a metallic electrode and a bulk material. Following Bedeaux and Kjelstrup [4, 9] a relatively successful, thermodynamically consistent, approach to describe interfacial inhomogeneities consists of considering the membrane to be composed of a uniform central "bulk" material between two thin interfacial layers. The fluxes are considered to be continuous through these layers and hence the "resistance" of the individual layers is additive, i.e.,

$$\mathbf{L}_{tot}^{-1} = \frac{\delta_{right} \mathbf{L}_{right}^{-1} + d \mathbf{L}_{mem}^{-1} + \delta_{left} \mathbf{L}_{left}^{-1}}{\delta_{right} + d + \delta_{left}} \quad (2.12)$$

where \mathbf{L}^{-1} is the inverse of the transport coefficient matrix and represents the resistivity of the membrane. The thicknesses of the interfacial layers, $\delta_{left/right}$, are generally not known and remain integrated within the coefficient matrix of the layers.

In the following we shall analyse the literature information on a standard ionomer membrane both on the bulk and on the interfacial coefficient values.

2.3. Membrane properties: a literature survey

Proton conductivity, water permeability and diffusivity, hydrogen permeability, and electro-osmotic drag of Nafion™ membranes for fuel cell applications are presented in this section. State of the art measurements and proceedings are summarized and discussed in order to give a global idea of where the technology stands and the shortcomings of the current methods. Here we attempt to show that the interfaces play a bigger role than attributed to them by disentangling their effects from existing results and why it is important to consider them in fuel cell engineering.

2.3.1. Proton conductivity

In PEM analysis, membrane properties are usually discussed in terms of water content, λ , a quantity expressed as the molar ratio of water molecules to sulfonate groups ($-SO_3^-$). When referring to proton conductivity it should be noted that charge transport happens through a hydrated membrane, that is, through the water held by a polymer matrix. Hence, the mechanism is not the same as in bulk water because of the additional forces exerted by the polymer matrix and sulfonate groups [3, 7, 13, 14]. Nevertheless, to understand proton transfer in acidic hydrated membranes, such as Nafion™ in PEM fuel cells, it is important to firstly understand the transfer mechanisms in bulk water. In general, there are two mechanisms that describe this phenomenon, namely structure diffusion and vehicle diffusion. Their relative prevalence in bulk water significantly differs from that in membranes albeit that it also depends on the water content.

The structure diffusion of protons, also known as the Grotthuss mechanism, refers to the transfer of protons by tunneling from one water molecule to the next via hydrogen bonding, which is not an actual movement of the ion through the solvent but a rearrangement of atoms; this mechanism is often referred to as "proton hopping" [3, 15, 16]. On the other hand, it should be noted that water has a high self-diffusion coefficient which has a contribution on the total proton conductivity as protonated water molecules, in the form of H_3O^+ or $H_9O_4^+$; this phenomenon is known as vehicle diffusion and it has a contribution of approximately 22% to the total conductivity assuming that the diffusion coefficients of H_2O and H_3O^+ are the same at Standard Temperature and Pressure (STP) conditions [3, 17].

In a hydrated acidic polymer, the ionomer material most used for PEM fuel cells, two types of domain can be recognized: hydrophobic domains constituting the polymer backbone that grant the membrane its morphological stability; and hydrophilic domains that allow the proton conduction and consist of protonated sulfonate groups ($-SO_3H$). This domain is described as well-connected through nanochannels even at a low water content. Hence, percolation in these membranes is very good because there are almost no dead-end pockets [3, 27, 30]. Moreover, a transition region has been identified between the hydrophobic and hydrophilic domains which is considered to be the consequence of the side-chain architecture of Nafion™. This region is believed to confer Nafion™ with its swelling characteristic as it has been suggested that there is a progressive side-chain unfolding with increasing water content. Water content can be seen as the hydration of the $-SO_3^-$ groups

and can be related to widening of the nanochannels and increasing conductivity as the membrane becomes more hydrated. At medium to high values of hydration, $\sim 10 < \lambda < 22$, the excess protons are located in the centre of the nanochannels where the water is bulk-like and, thus, the proton transfer is similar to the phenomena described above for aqueous solutions with structure diffusion prevalently occurring. However, as the degree of hydration decreases, the concentration of protons increases, which generates more proton-donor than acceptor sites; this fact creates a bias of the hydrogen bonds in the electrostatic field which in turn suppresses structure diffusion. Hence, at low water content the transport of protons is mostly due to vehicular diffusion [3]. The characterization of proton conductivity can be done by either creating a faradaic current, i.e., where there is mass transfer, or by inducing a non-faradaic current, i.e., no mass transfer; in the former case, a redox couple is used to generate electrons as in the case of running electrochemical cells, and in the latter, charge is induced at the electrode interface by an external electric field as it is done in techniques such as NMR or Electrochemical Impedance Spectroscopy (EIS). Commonly, proton conductivity is assessed by EIS, a technique that determines the resistance of a membrane by applying an oscillating electric potential and varying its frequency [15, 18–27]. However, properties determined by EIS are averaged quantities and its interpretation usually involves assuming isotropy of the material. The conductance of a membrane can be quantified by performing experiments in different configurations, namely in-plane [15, 18–20, 22–27] and through-plane measurements [21]. In-plane measurements quantify the conductance in the length of the membrane, while through-plane measurements do so across its thickness. Studies have shown that in-plane measurements are preferred over through-plane measurements as it will be discussed later.

Reported conductivity data in the literature is often difficult to assess as results vary from laboratory to laboratory depending on experimental conditions. Studies have shown that conductivity measurements are influenced by the technique employed and the geometry of the conductivity cell [15, 18, 19, 27]. In the first, conductivity values might be extracted by extrapolating the imaginary part of the measured impedance in the low frequency region [15, 18, 19, 21–24, 26, 27, 27] or extracted from fitting values for the components of an equivalent circuit [15, 19]. In the latter, different geometries of the conductivity cell include a 2-probe [15, 19, 21–24, 27, 28] or 4-probe cell [15, 19] where the distance between the measuring probes also plays a role. A summary of the possible configurations for EIS measurements is shown in figure 2.1.

In the 2-probe configuration, the voltage measuring electrodes also carry the current. Under an alternating electric field and particularly at low frequencies, a certain amount of ions reaches the electrode before the reversal of polarity which results in charge build up at the interfaces and, thus, lowers the electric field in the bulk of the membrane; this phenomenon is often referred to as electrode blocking [15, 19]. On the other hand, carrying out the impedance measurements using four probes helps diminish the effect of charge build up near the current carrying electrodes by using different electrodes sufficiently far away from the charge build-up region to measure the voltage across the bulk membrane material [15, 19]. The

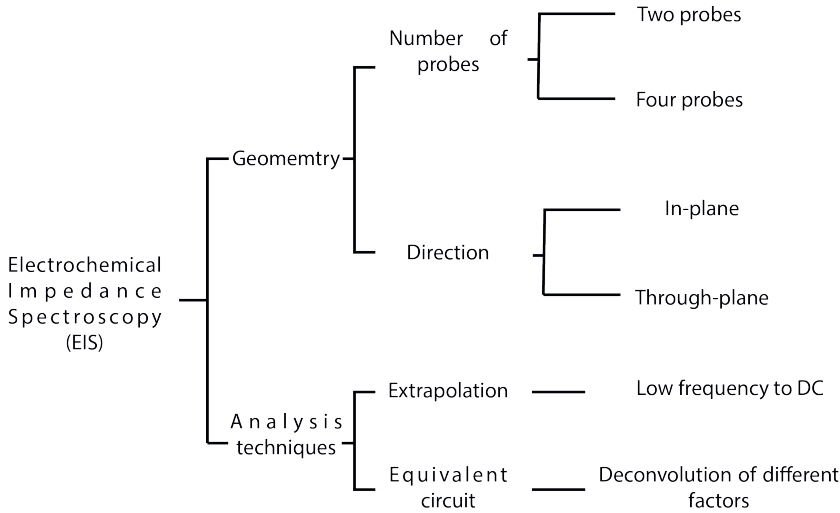


Figure 2.1: Electrochemical Impedance Spectroscopy: measurement and analysis techniques.

voltage measuring electrodes are connected through a high impedance device so that the current flowing through them is negligible [15, 19].

Conductivity measurements using the 4-probe method are appropriate for ionic conducting materials with low resistivity as the interfacial effects are diminished, whereas the 2-probe measurement is appropriate for high-resistance materials since other impedances present in the circuit can be neglected [15]. Furthermore, and regardless of the geometry of the cell, the subsequent analysis of the obtained data must be manipulated in order to retrieve the conductivity values. This is done either by extrapolating the obtained semicircle to its intercept with the real axis at low frequencies and taking this value as the bulk resistivity of the membrane; or, conversely, by fitting the obtained data to an equivalent circuit. In the latter, it is possible to disentangle the effects of the interfaces from those of the bulk material [15, 19]. An important aspect that is often overlooked in the assessment of membranes is that the faradaic conductivity and the non-faradaic conductivity differ when the ionic species do not play the same role. In the case of conductivity measurements involving charge transfer at electrodes—in the faradaic setting—some ions are current carrying and others are blocked. Hence, it is possible to have excellent values for non-faradaic conductivity (no mass transfer) and extremely bad values in a faradaic setting (with mass transfer). For the present case of proton conducting membranes with anions fixed to the membrane, this is not expected to play a role as there is only one charge carrier which is also involved in the charge transfer at the electrodes.

Despite the various different techniques with expected differing outcomes, it is found in the literature that conductivity measurements are done in many instances with disregard to the above mentioned potential errors. As a consequence, the lack of a standard measurement method and data analysis technique leads to vary-

ing results and imprecise estimations of the proton conductivity, which ultimately hinders the development of effective PEMs. In Figure 2.2 an example of different conductivity values for a bare Nafion™117 membrane found in the literature is presented. Even though the experiments were performed at different temperatures, it is evident that the values follow different trends for various measurement cell geometries. Zawodzinski et al. [20, 27] measured the proton conductivity at 30 °C in a 2-probe, in-plane set-up and later Springer et al. [13, 26, 28] correlated Zawodzinski's values for the water content and temperature according to

$$\sigma[mS/cm] = (5.139\lambda - 3.26)\exp\left\{1268\left(\frac{1}{303} - \frac{1}{T}\right)\right\} \quad (2.13)$$

The data and correlation from Zawodzinski and Springer, respectively, have been widely used ever since as a benchmark [15]. Lee et al. [15] performed a systematic investigation on the effect of using two or four probes to measure conductivity in-plane at 60 °C. Their results showed a clear difference between the two methods indicating the nature of the contact effects as shown separately in figure 2.2. However, their measured values are much lower than those of Zawodzinski even though Lee et al. performed them at higher temperatures. This fact clearly shows the discrepancy found in the experimental results and the difficulty of assessing them properly. Reasons for this variability include the irreproducibility of the membranes, where no two samples are equal, e.g., different thickness, different pre-treatment method, in addition to the largely irreproducible effects of contacts or interfaces. This indeed calls for the necessity of standard measurement methods.

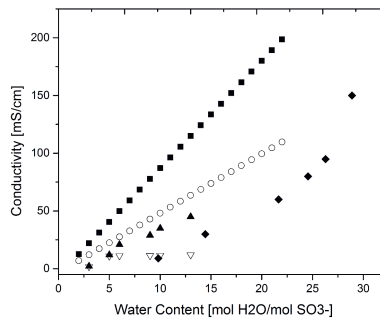
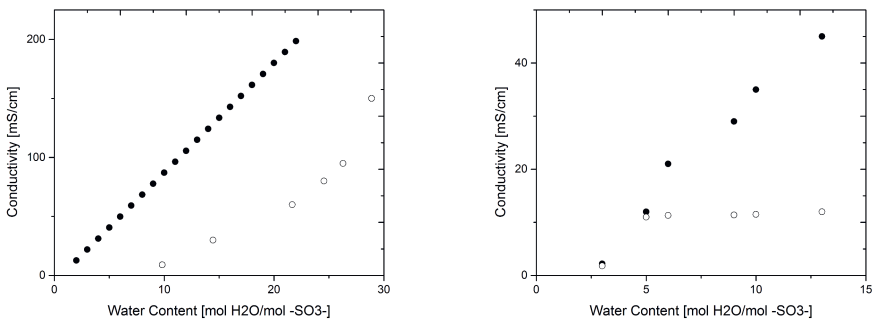


Figure 2.2: Nafion™ 117 conductivity value comparison. Springer et al. at 80 °C, in-plane, 2-probe (■) [26]; Zawodzinski et al. at 30 °C, in-plane, 2-probe (○) [20]; Lee et al. at 60 °C, in-plane, 4-probe (▲) [15]; Lee et al. at 60 °C, in-plane, 2-probe (▽) [15]; Alberti et al., through-plane, 2-probe (◆) [21].

Figure 2.3 presents the differences in proton conductivity results obtained by the different geometries of the measuring cell. The data were fitted to an average function in both cases and the mean-square and root-mean-square errors were calculated; additionally, the percentage error was averaged over the whole range (see section 2.4). A comparison of the 2-probe and 4-probe method yields an error of 34.6%, while the effect of the plane in which the measurement is done shows

an error of 32.8%. These errors are a representation of the variability between measurements and support the hypothesis that the interfaces play a much more important role than is usually attributed to them. These effects are particularly notorious when comparing the results between the 2-probe and the 4-probe case, where the effect of the interfaces are known to play a role. At higher water content, where the Grotthuss mechanism of transport is dominant, the proton conductivity was lower for the 2-probe case due to other impedances present in the system apart from that of the bulk membrane. All the same, when comparing the plane in which the measurement was carried out, through-plane measurements yielded lower values which can be related to the fact that the interfaces, or area over which the current is being transported, is larger; hence, having a bigger contribution on the overall resistance. This fact is supported by studies performed at Scribner Associates Inc. labs where the contact resistance's effect or "cell resistance" was eliminated by extrapolating the resistance at high frequencies to zero membrane thickness in a through-plane configuration. By doing this correction, they found that the membrane conductivity was the same for in- and through-plane measurements. This also provides evidence for the intrinsic isotropy of the material although this fact holds only for bare or untreated membranes as MEA (membrane electrode assembly) preparation processes such as hot-pressing may induce structural changes that affect charge transport in different directions [29].



(a) in-plane (●) vs. through-plane (○)[26]

(b) 2-probe (●) vs. 4-probe(○) [21].

Figure 2.3: Effect of geometry.

2.3.2. Water permeability

Water transport in proton-conducting membranes is of the most importance as water is mainly responsible for the transport of charges across the membrane. Therefore, the permeability of the membrane to water molecules and their diffusivity are properties that have been extensively studied [2, 7, 8, 20, 27, 30]. The water permeation process through a membrane can be expressed in terms of three different steps, namely (i) sorption of water into the membrane at the sorption side,

(ii) diffusion of water across the membrane, and (iii) desorption of water from the membrane at the dry side [7, 8]. The sorption and desorption steps represent interfacial resistances to mass transport and have been studied by several authors [2, 7, 8]. From their permeation studies, they have reported that reasons for this resistance to be significant include the membrane's surface being hydrophobic to water vapour and hydrophilic to liquid water. This has been proven by SAXS (Small Angle X-ray Scattering) experiments that corroborated structural changes of the membrane's interface according to the medium it was in contact with [7]. Majsztrik et al. reported that the rate limiting step in permeation experiments was water desorption at the membrane/gas interface [8].

There are various methods to estimate water permeability and diffusivity (see next subsection) through a membrane [7] and unfortunately literature results are found to vary with the measuring technique. Zhao et al. and Majsztrik et al. have reviewed them and shown that results for permeability and diffusivity vary up to three orders of magnitude [7, 8]. Water permeability is typically measured with a simple permeation experiment where two water-filled chambers are separated by the membrane and a total pressure difference is applied. The change in volume in the lower pressure chamber is measured with a capillary and related to the permeability of the membrane [3, 31]. Alternatively, water diffusivity through the membrane can be measured by NMR [2, 7, 8, 20, 30] and then related to the permeability using the following argument. From Fick's law, that relates mass flux to the concentration gradient, one obtains an expression in terms of the water diffusivity D_w as

$$J_w = -D_w \frac{\Delta c_w}{\delta} = -\frac{D_w c_w}{RT} \frac{\Delta \mu_w^v}{\delta} = -\frac{D_w}{p_w V_w} \frac{\Delta p_w}{\delta} \quad (2.14)$$

where p_w is the water vapor pressure in equilibrium with the water in the membrane. The water permeability defined in the previous section is then related to the diffusivity as $P_w = PV/V_w = D_w/(p_w V_w)$ assuming that the experiments are done in the absence of hydrogen so that the volume flow only involves water. The water permeability is usually given in $\text{mol cm}^{-1} \text{s}^{-1} \text{bar}^{-1}$ and the diffusivity in $\text{cm}^2 \text{s}^{-1}$.

Data gathered for permeability and diffusivity of water through a Nafion™117 membrane are shown in figure 2.4. For comparison, the diffusivity values were converted to permeability using the above argument. The data were fit to an average function to assess the variability among experiments.

The data are spread over several orders of magnitude, indicating underlying phenomena that were not accounted for. The highest values correspond to those measured by NMR for the intra-diffusion coefficient; however, those obtained by permeation experiments are much lower. The data from permeability measurements and the calculated values from diffusivity seem to follow the same trend which is expected from the above argument; nevertheless, at low water contents the trend seems to be different.

Two regimes can be identified in the permeability of the membrane, with a faster increase after a water content higher than 14. However, in the case of diffusivity there seems to be an inflexion point at a lower water content (~ 4). Zhao et al.

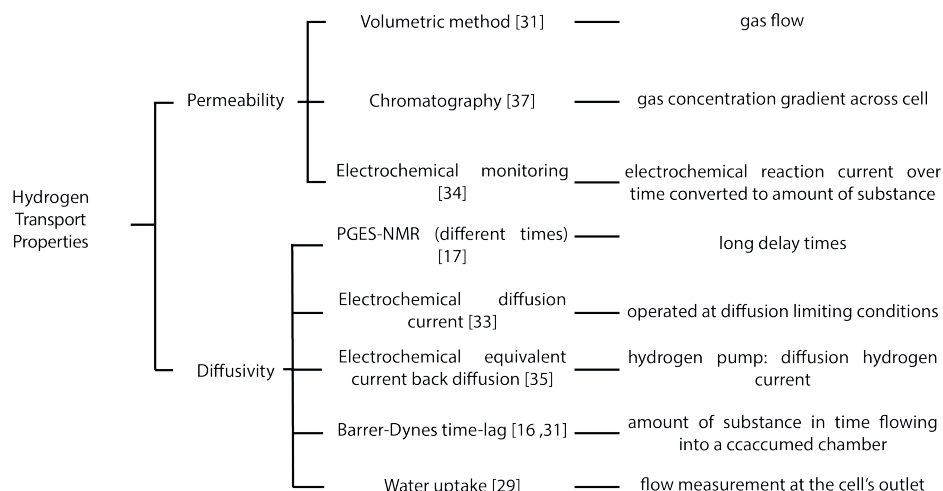


Figure 2.5: Permeability and Diffusivity measuring techniques.

extracted from results reported as permeation flux ($\text{mol cm}^{-2} \text{s}^{-1}$) by means of the hydrogen saturation pressure in water. Figure 2.6 shows different results from various measuring techniques for hydrogen permeability; for comparison, the points corresponding to a wet and a dry membrane are also shown. In this case, the variability was evaluated between experiments performed by an electrochemical technique [35] vs. chromatography [32] as the sample of data is spread over a larger range of water content values. The average relative error in this case was estimated to be $\sim 28\%$. The higher values are those reported by Broka et al. [38] who used a volumetric method to measure hydrogen permeability, whereas electrochemical methods presented lower, but varying, values. This difference could be attributed to the presence of electrical interfaces in the electrochemical measurements. In these cases, protons were allowed through the membrane and the current generated was related to the amount of substance through Faraday's law. Due to the electrical resistances at the interfaces, it is natural to assume electrical losses and thus, the measurements would yield lower values. This effect will be discussed further in the next section.

2.3.4. Electro-osmotic drag

The motion of water is not only caused by the chemical potential difference, but also by the motion of protons, which is in return proportional to the current flowing through the membrane. This coupling effect is known as electro-osmotic drag and it is defined as the number of water molecules dragged per charge carrier [3, 6, 13, 20, 27, 39–43]. Measuring this property is non-trivial and as a consequence it has not been widely studied. However, there have been some attempts in the literature which in turn might give some insights about the role the interfaces are playing. A summary of the methods used to measure the electro-osmotic drag to

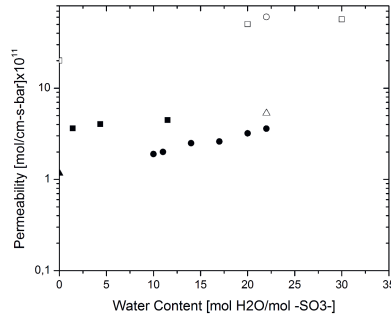


Figure 2.6: Hydrogen permeability. Schalenbach at 80 °C (●)[35]; Broka et al. at 80 °C (■)[38]; Sakai et al. at 80 °C (□)[32]; Jiang et al. at 80 °C (extrapolated) (○)[34]; Dry membrane (▲)[35]; Wet membrane (△)[35].

our knowledge is presented in figure 2.7.

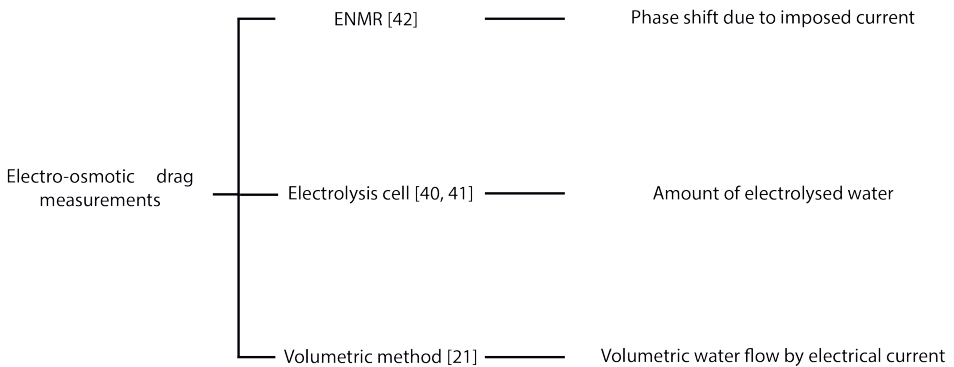


Figure 2.7: Electro-osmotic drag measuring techniques.

Figure 2.8 shows a compilation of data results that were rendered reliable for the analysis presented in this paper. The majority of the data have been gathered by Kreuer et al. over the course of years [3, 31, 41, 44], gathering information at various temperatures and different water contents using electrophoretic NMR (ENMR), a set-up that was built in their group for this purpose.

A comparison between results obtained by different techniques at 30 °C and 80 °C gives errors of about 27.6% and 30.2%, respectively (calculated as indicated in the Proton conductivity section). The information at low water contents is very limited, but regardless of this fact, some information can be extracted if looking at a common point among the three techniques. In figures 2.8 and 2.9, it can be seen that at a water content of $22 \text{ mol H}_2\text{O/mol -SO}_3^-$ the electro-osmotic drag values found were considerably different for each technique. The highest value was found by Onda et al. [43] where an electrochemical technique was employed for

this purpose, whereas the values found by Kreuer et al. were measured by ENMR. The nature of these differences could be due to the effect of electric interfaces interfering with the measurement, however more evidence is necessary to support this hypothesis.

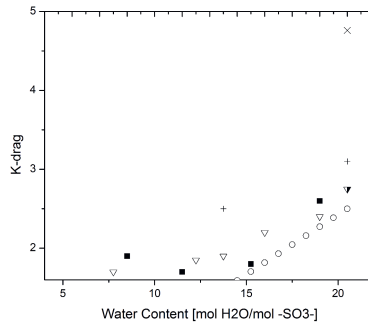
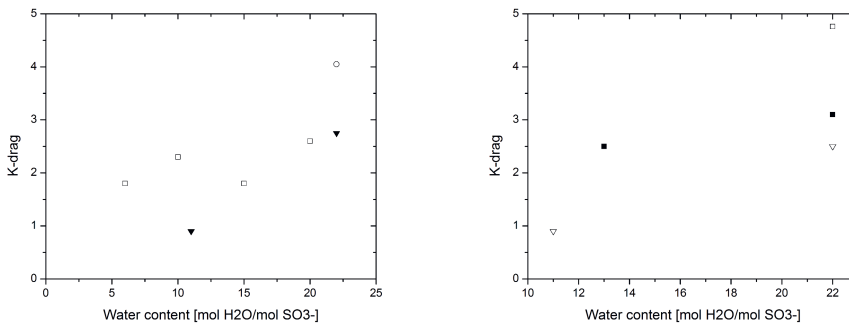


Figure 2.8: Electro-osmotic drag data compilation. Ise, Kreuer at 27 °C (■)[31]; Kreuer et al. at 27 °C (▽)[41]; Springer et al. at 80 °C (o)[26]; Onda et al. at 80 °C (x)[43]; Kreuer et al. at 80 °C (+)[3]; Zawodinski at 30 °C (▽)[27].



(a) 30 °C Electrophoretic NMR (□) [44]; Volumetric (b) 80 °C ENMR (■) [41]; Volumetric (▽) [26]; Electrolysis cell (o) [43]; Electrolysis cell (□) [43].

Figure 2.9: K-drag.

2.4. Discussion

In general, the assessment of membranes is not standardized which creates a chaotic amount of information that is difficult to assess and not entirely reliable as shown in the previous section. The data must be treated with special care and attention to the conditions and measuring techniques that were used, as these

Table 2.1: Summary of interfacial contributions.

Transport Coefficient	Bulk	Interface	Overall
Conductivity (mS/m)	45	0.88×10^{-3}	12
Water permeability (mol/cm-s-bar) $\times 10^9$	948	2.3×10^{-4}	4.2
Hydrogen permeability (mol/cm-s-bar) $\times 10^{11}$	50	2×10^{-4}	3.6
Electro-osmotic drag (molecule H ₂ O/charge carrier)	2.75	4.6×10^{-4}	4.05

reveal information about the suitability of property values for certain applications. For instance, the proton conductivity measured with two probes in figure 2.3a reflects mainly the resistances at the interfaces, whereas the measurement with four probes mainly reflects the bulk. For membrane science and development, the bulk measurement would be of most interest while in fuel cell engineering through-plane measurements would be more meaningful as a fuel cell operates in this configuration.

To illustrate this point further, the TCM methodology explained in Section 2 may be used to disentangle the effects of the bulk and interface for all properties. As proton conductivity remains constant after $\lambda \sim 5$ when measured with two probes (see figure 2.3a), one may argue that this value reflects the combined effects of the bulk and interfaces as the resistances were not further decreasing with increasing water content, whereas the tendency of conductivity to increase with the water content in the 4-probe case suggests values closer to the bulk. From equation 2.14, and considering the electro-osmotic drag to be negligible, it follows that

$$\frac{\delta_m}{\sigma_m} = \frac{2\delta_{if}}{\sigma_{if}} + \frac{\delta_b}{\sigma_b} \quad (2.15)$$

where the suffixes m , if , and b stand for the membrane, interface, and bulk, respectively. Studies have shown that the extension of the interface in a Nafion™/Pt catalyst layer system is of a few nanometers (~ 5 nm) [45]. Considering that a standard Nafion™ 117 membrane has a dry thickness of 186 μm , the total value of the membrane conductivity can be computed. Equation 2.15 can be written for the 2-probe (2p) and 4-probe (4p) cases, as follows:

$$\begin{aligned} \frac{d_m}{\sigma_{2p}} &= \frac{2d_{if}}{\sigma_{if}} + \frac{d_b}{\sigma_b} \\ \frac{d_m}{\sigma_{4p}} &= \frac{d_b}{\sigma_b} \end{aligned} \quad (2.16)$$

where the subindexes $2p$ and $4p$ refer to the 2-probe and 4-probe measurements, respectively. Bulk, interface, and overall values can be computed by solving this simple set (see table 2.1).

The same logic can be followed for water permeability, hydrogen permeability, and electro-osmotic drag. In the case of water permeability, Zhao et al. [7] characterized the water diffusivity by NMR, and subsequently calculated the permeability by correcting for the interfacial effects, i.e., based on varying water activities at

Table 2.2: Relative deviation from measurement of the overall values.

Transport Coefficient	Deviation from Bulk
Conductivity (mS/m)	-73.3%
Water permeability (mol/cm-s-bar) $\times 10^9$	-99.5%
Hydrogen permeability (mol/cm-s-bar) $\times 10^{11}$	-92.8%
Electro-osmotic drag (molecule H ₂ O/charge carrier)	+47.2%

the feed side, they estimated an interfacial mass transport coefficient as suggested in previous studies by Majzstrik et al. [8]. Therefore, the results found by Zhao et al. are approximated to be the bulk values, whereas those of Ise and Kreuer [41] found by a permeation experiment are considered to include large interfacial contributions. Consequently a corrected overall value for water permeability can be found from a procedure analogous to equations 2.15 and 2.16.

Schalenbach et al. [35] measured hydrogen permeability using an electrochemical technique. In their experiment, hydrogen is left to permeate through a membrane followed by an electrochemical cell that converts the permeated hydrogen into protons; the generated current thus represents the permeation of hydrogen through the membrane and it is related to the total amount of gas by Faraday's law. One may argue that due to the nature of the experiment, the overpotentials at the interfaces will consume a certain part of the voltage drop and hence the value that is being measured is lower than the actual charge transport due to permeability. If the permeability of hydrogen measured with a volumetric method [32] is assumed to have negligible interfacial contributions i.e. mainly bulk, and the electrochemical measurement to induce large losses at the interfaces, a similar treatment to that mentioned above applies in order to calculate a corrected overall hydrogen permeability of the membrane.

Similarly, for the electro-osmotic drag, the results by Zawodinski et al. [27] found by a volumetric method can be attributed to the bulk, whereas the measurements by Onda et al. [43] in an electrolysis cell would account for combined interfacial and bulk contributions. A summary of the overall property values is shown in table 2.1.

The corrected overall values show large deviations from measurements where the resistance contributions have been corrected for, and small differences with those where interfacial effects are thought to predominate. This behaviour depicts the fact that the role of contact resistances becomes increasingly important in measurements where conditions resemble more closely those of an operating fuel cell. A normalized comparison and deviation percentages are shown in figure 2.10 and table 2.2.

When corrected for interfacial contributions, the overall proton conductivity equals that from the 2-probe measurement where interfacial effects are thought to predominate and differs 73% from those where the set-up has been improved to reduce contact resistances (4-probe). Even though 4-probe measurements are the main geometry used to assess proton conductivity, the large difference with the overall value indicates that this property will be significantly lower when the membrane is

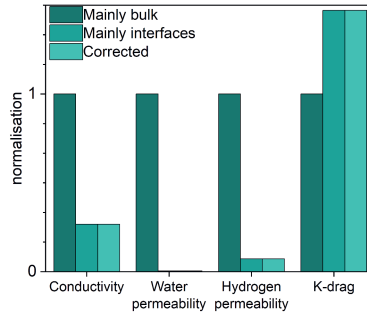


Figure 2.10: Comparison with measurements of bulk values as reference.

put into application. Similarly, water and hydrogen permeability show errors larger than 90% when corrected as compared to those where interfacial effects have been eliminated. This suggests that mass transfer at the interfaces is the limiting step. On the other hand, the electro-osmotic drag shows an opposite behaviour due to the nature of the experiment where the amount of molecules carried by the current can be easily overestimated by the amount of electrolysed water.

In general, these results highlight the necessity to assess membranes and MEAs in conditions as close as possible to those of an operating fuel cell, as measurements of bare membranes can be highly deceptive. A large part of the research on transport properties has focused on isolating bulk values, whereas less attention has been given to the role of the interfaces on the overall results. Nevertheless, a few studies have demonstrated a deviation of certain properties in bulk membranes with respect to thin films where the behaviour is expected to resemble the interfaces due to confinement effects [46, 47].

Here, it has been shown that the effect of interfaces can be unraveled using the transport coefficient matrix (TCM) method and their effect over the total values for properties of interest in fuel cell engineering should be treated carefully, as it was made evident by the variability of the results found in the literature (see table 2.3) and the large deviation of the overall values from the bare membranes. This fact supports the hypothesis that the interfaces play a greater role than commonly considered and highlight the necessity to further study interfaces in order to unravel and account for mechanisms of charge and mass transport if more efficient fuel cells are to be attained.

2.5. Conclusions

A systematic method to discriminate between bulk and interfacial resistances to mass and charge transport has been presented and exemplified for key membrane properties in PEM fuel cell applications. It was shown that this method allows unraveling of the interfacial effects and that this can be done from existing experimental results if critically assessed and handled. The proper handling of data highlights

Table 2.3: Summary of errors between measuring techniques for each property.

Transport Coefficient	Conditions	RMSE (unit)	% Error
Conductivity (mS/cm)	2- vs. 4-probe	9.3	35%
	In- vs. Through-plane	41.2	33%
Water permeability (mol/cm-s-bar) $\times 10^9$	-	3897	906%
Hydrogen permeability (mol/cm-s-bar) $\times 10^{11}$	-	0.9	28%
	T = 30 °C	0.6	28%
Electro-osmotic drag (molecule H ₂ O/charge carrier)	T = 80 °C	0.4	30%

the necessity to carefully choose and understand experiments when measuring bare membranes or MEAs to closely resemble a fuel cell.

Interfacial effects on mass and charge transport resistances are crucial in fuel cell engineering and including rather than eliminating them is of prime importance for fuel cell development. This is supported by the results of our analysis where interfacial effects account for significant percentages of the total measured values, particularly in permeability measurements. This suggests that studying membranes as close as possible to fuel cell operation would yield more efficient and possibly cheaper fuel cells, and knowing the effects of contact resistances on all relevant properties is a powerful tool for optimization in this scenario.

Furthermore, it was shown that the results reported in the literature are of an erratic nature often due to the method in which properties are measured. This fact creates a difficulty in assessing and comparing them which ultimately results in hindering the progress of fuel cell engineering. The TCM method herein demonstrated also offers a systematic way of presenting and analyzing the different properties and parameters deemed relevant for a certain system which could be advantageous for membrane and fuel cell studies by helping scientists and engineers gather more relevant and consistent data in a simpler, more accessible manner.

References

- [1] A. Rangel-Cárdenas, "Transport in Proton Exchange Membranes for Fuel Cell Applications—A Systematic Non-Equilibrium Approach," *Materials*, vol. 10, no. 6, p. 576, 2017.
- [2] D. Rivin, C. E. Kendrick, P. W. Gibson, and N. S. Schneider, "Solubility and transport behavior of water and alcohols in Nafion™," *Polymer*, vol. 42, no. 2, pp. 623–635, 2001.
- [3] K.-D. Kreuer, S. J. Paddison, E. Spohr, and M. Schuster, "Transport in Proton Conductors for Fuel-Cell Applications," *Chemical Reviews*, vol. 104, no. 10, pp. 4637–4678, 2004.
- [4] D. Kjelstrup, S.; Bedeaux, *Non-equilibrium thermodynamics of Heterogeneous Systems*.
- [5] "Scope," in *Non-Equilibrium Thermodynamics for Engineers*, pp. 1–5, WORLD SCIENTIFIC, apr 2017.
- [6] T. F. Fuller and J. Newman, "Experimental Determination of the Transport Number of Water in Nafion 117 Membrane," *Journal of the Electrochemical Society*, vol. 139, no. 5, pp. 1332–1337, 1992.
- [7] Q. Zhao, P. Majsztrik, and J. Benziger, "Diffusion and interfacial transport of water in Nafion," *Journal of Physical Chemistry B*, vol. 115, no. 12, pp. 2717–2727, 2011.
- [8] P. W. Majsztrik, M. B. Satterfield, A. B. Bocarsly, and J. B. Benziger, "Water sorption, desorption and transport in Nafion membranes," *Journal of Membrane Science*, vol. 301, pp. 93–106, sep 2007.
- [9] P. De Groot, S.R. and Mazur, *Non-equilibrium thermodynamics*. Courier Corporation, 2013.
- [10] Kondepudi, Dilip and I. Prigogine, *Modern thermodynamics: from heat engines to dissipative structures*. John Wiley & Sons, Inc., 2014.
- [11] L. Onsager, "Mbauaay 15, 1931 Volume, 37 Reciprocal Relations in Irreversible Processes. I," *Physical Review*, vol. 37, p. 405, 1931.
- [12] Newman, John and K. E. Thomas-Alyea, *Electrochemical systems*. John Wiley & Sons, Inc., 2012.
- [13] H. Ito, T. Maeda, A. Nakano, and H. Takenaka, "Properties of Nafion membranes under PEM water electrolysis conditions," *International Journal of Hydrogen Energy*, vol. 36, no. 17, pp. 10527–10540, 2011.
- [14] X. Wu, X. Wang, G. He, and J. Benziger, "Differences in water sorption and proton conductivity between Nafion and SPEEK," *Journal of Polymer Science, Part B: Polymer Physics*, vol. 49, no. 20, pp. 1437–1445, 2011.

- [15] C. H. Lee, H. B. Park, Y. M. Lee, and R. D. Lee, "Importance of proton conductivity measurement in polymer electrolyte membrane for fuel cell application," *Industrial and Engineering Chemistry Research*, vol. 44, no. 20, pp. 7617–7626, 2005.
- [16] A. A. Kornyshev, A. M. Kuznetsov, E. Spohr, and J. Ulstrup, "Kinetics of Proton Transport in Water," *The Journal of Physical Chemistry B*, vol. 107, pp. 3351–3366, apr 2003.
- [17] Y.-K. Choe, E. Tsuchida, T. Ikeshoji, S. Yamakawa, and S.-a. Hyodo, "Nature of proton dynamics in a polymer electrolyte membrane, nafion: a first-principles molecular dynamics study," *Physical Chemistry Chemical Physics*, vol. 11, no. 20, p. 3892, 2009.
- [18] B. D. Cahan and J. S. Wainright, "AC Impedance Investigations of Proton Conduction in Nafion™," *Journal of the Electrochemical Society*, vol. 140, no. 12, pp. L185–L186, 1993.
- [19] Z. Xie, C. Song, B. Andreaus, T. Navessin, Z. Shi, J. Zhang, and S. Holdcroft, "Discrepancies in the measurement of ionic conductivity of PEMs using two- and four-probe AC impedance spectroscopy," *Journal of the Electrochemical Society*, vol. 153, no. 10, pp. 6–11, 2006.
- [20] T. A. Zawodzinski, M. Neeman, L. O. Sillerud, and S. Gottesfeld, "Determination of water diffusion coefficients in perfluorosulfonate ionomeric membranes," *Journal of Physical Chemistry*, vol. 95, no. 15, pp. 6040–6044, 1991.
- [21] G. Alberti, M. Casciola, L. Massinelli, and B. Bauer, "Polymeric proton conducting membranes for medium temperature fuel cells (110–160°C)," *Journal of Membrane Science*, vol. 185, no. 1, pp. 73–81, 2001.
- [22] C. A. Edmondson, J. J. Fontanella, S. H. Chung, S. G. Greenbaum, and G. E. Wnek, "Complex impedance studies of S-SEBS block polymer proton-conducting membranes," *Electrochimica Acta*, vol. 46, no. 10–11, pp. 1623–1628, 2001.
- [23] J. J. Fontanella, C. A. Edmondson, M. C. Wintersgill, Y. Wu, and S. G. Greenbaum, "High-pressure electrical conductivity and NMR studies in variable equivalent weight NAFION membranes," *Macromolecules*, vol. 29, no. 14, pp. 4944–4951, 1996.
- [24] R. W. Kopitzke, C. A. Linkous, H. R. Anderson, and G. L. Nelson, "Conductivity and water uptake of aromatic-based proton exchange membrane electrolytes," *Journal of the Electrochemical Society*, vol. 147, no. 5, pp. 1677–1681, 2000.
- [25] T. Navessin, M. Eikerling, Q. Wang, D. Song, Z. Liu, J. Horsfall, K. V. Lovell, and S. Holdcroft, "Influence of membrane ion exchange capacity on the catalyst layer performance in an operating PEM fuel cell," *Journal of the Electrochemical Society*, vol. 152, no. 4, pp. 796–805, 2005.

- [26] T. E. Springer, T. A. Zawodzinski, and S. Gottesfeld, "Polymer Electrolyte Fuel Cell Model," *Journal of the Electrochemical Society*, vol. 138, no. 8, pp. 2334–2342, 1991.
- [27] Thomas A. Zawodzinski Jr., D. Charles, R. Susan, J. S. Ruth, T. S. Van, E. S. Thomas, and G. Shimshon, "Water Uptake by and Transport Through Nafion[®] 117 Membranes," *Journal of the Electrochemical Society*, vol. 140, no. 4, pp. 1041–1047, 1993.
- [28] T. E. Springer, M. S. Wilson, and S. Gottesfeld, "Modeling and Experimental Diagnostics in Polymer Electrolyte Fuel Cells," *Journal of The Electrochemical Society*, vol. 140, pp. 3513–3526, dec 1993.
- [29] K. R. Cooper, "Progress Toward Accurate Through-Plane Ion Transport Resistance Measurement of Thin Solid Electrolytes," *Journal of The Electrochemical Society*, vol. 157, no. 11, p. B1731, 2010.
- [30] C. A. Edmondson and J. J. Fontanella, "Free volume and percolation in S-SEBS and fluorocarbon proton conducting membranes," *Solid State Ionics*, vol. 152-153, pp. 355–361, 2002.
- [31] M. Ise, *Polymer electrolyte membranes: Investigations into the microstructure and the transport properties for protons and water*. PhD thesis, Universit t Stuttgart: Stuttgart, Germany, 2000.
- [32] T. Sakai, H. Takenaka, and E. Torikai, "Gas Diffusion in the Dried and Hydrated Nafions," *Journal of the Electrochemical Society*, vol. 133, no. 1, pp. 88–92, 1986.
- [33] T. Sakai, H. Takenaka, N. Wakabayashi, Y. Kawami, and E. Torikai, "Gas Permeation Properties of Solid Polymer Electrolyte (SPE) Membranes," *Journal of the Electrochemical Society*, vol. 132, no. 6, pp. 1328–1332, 1985.
- [34] J. Jiang and A. Kucernak, "Investigations of fuel cell reactions at the composite microelectrode | solid polymer electrolyte interface. I. Hydrogen oxidation at the nanostructured Pt | Nafion[®] membrane interface," *Journal of Electroanalytical Chemistry*, vol. 567, no. 1, pp. 123–137, 2004.
- [35] M. Schalenbach, T. Hoefner, P. Paciok, M. Carmo, W. Lueke, and D. Stolten, "Gas Permeation through Nafion. Part 1: Measurements," *Journal of Physical Chemistry C*, vol. 119, no. 45, pp. 25145–25155, 2015.
- [36] M. Oszcipok, M. Fasil, B. Rohland, L. Jo, J. Garche, and R. Stro, "The compression of hydrogen in an electrochemical cell based on a PE fuel cell design," *Journal of Power Sources*, vol. 105, pp. 208–215, 2002.
- [37] C. Felice, S. Ye, and D. Qu, "Nafion-montmorillonite nanocomposite membrane for the effective reduction of fuel crossover," *Industrial and Engineering Chemistry Research*, vol. 49, no. 4, pp. 1514–1519, 2010.

- [38] P. Broka, K.; Ekdunge, "Oxygen and hydrogen permeation properties and water uptake of Nafion 117 membrane and recast film for PEM fuel cell," *J. Appl. Electrochem*, vol. 27, pp. 117–123, 1997.
- [39] M. J. Cheah, I. G. Kevrekidis, and J. Benziger, "Effect of interfacial water transport resistance on coupled proton and water transport across Nafion," *Journal of Physical Chemistry B*, vol. 115, no. 34, pp. 10239–10250, 2011.
- [40] X. Ye and C. Y. Wang, "Measurement of water transport properties through membrane-electrode assemblies: I. Membranes," *Journal of the Electrochemical Society*, vol. 154, no. 7, pp. 676–682, 2007.
- [41] K. D. Kreuer, "On the development of proton conducting polymer membranes for hydrogen and methanol fuel cells," *Journal of Membrane Science*, vol. 185, no. 1, pp. 29–39, 2001.
- [42] M. Santarelli, P. Medina, and M. Cali, "Direct high pressure hydrogen production: A laboratory scale PEM electrolyser prototype," *17th World Hydrogen Energy Conference 2008, WHEC 2008*, vol. 2, no. 1, pp. 938–941, 2008.
- [43] K. Onda, T. Murakami, T. Hikosaka, M. Kobayashi, R. Notu, and K. Ito, "Performance analysis of polymer-electrolyte water electrolysis cell at a small-unit test cell and performance prediction of large stacked cell," *Journal of the Electrochemical Society*, vol. 149, no. 8, 2002.
- [44] M. Ise, K. D. Kreuer, and J. Maier, "Electroosmotic drag in polymer electrolyte membranes: An electrophoretic NMR study," *Solid State Ionics*, vol. 125, no. 1, pp. 213–223, 1999.
- [45] Z. Siroma, T. Ioroi, N. Fujiwara, and K. Yasuda, "Proton conductivity along interface in thin cast film of Nafion®," *Electrochemistry Communications*, vol. 4, no. 2, pp. 143–145, 2002.
- [46] S. A. Eastman, S. Kim, K. A. Page, B. W. Rowe, S. Kang, C. L. Soles, and K. G. Yager, "Effect of confinement on structure, water solubility, and water transport in Nafion thin films," *Macromolecules*, vol. 45, no. 19, pp. 7920–7930, 2012.
- [47] X. Y. Zhang and Y. H. Ding, "Thickness-dependent structural and transport behaviors in the platinum-Nafion interface: A molecular dynamics investigation," *RSC Advances*, vol. 4, no. 83, pp. 44214–44222, 2014.

3

Anomalous water sorption kinetics in carbon-supported Nafion thin-films

*In our constant pursuit of something, we do not know
what is it that we want until we get it.
"The goals we pursue are always veiled"*

(Sabina in *The unbearable lightness of being*)

To understand the role of interfacial resistance to water transport in a system geometry comparable to that of a PEM fuel cell, water sorption kinetics in carbon-supported Nafion thin-films has been studied at different temperatures and relative humidities while varying the membrane thickness. We have found anomalous water sorption kinetics at short time scales, i.e. deviation from the Fickian diffusion characteristic of these systems. We observe two different time scales with a delayed onset to Fickian behaviour that can be understood as the existence of two regimes with different diffusion coefficients. We attribute them to an interfacial diffusivity, D_i , and a bulk diffusivity, D_b . The onset delay is more pronounced on thinner films due to increased interfacial resistance. Here, we show with a simple mathematical model based on Crank's solution to Fick's second law, that the presence of two regimes where water transport at the interface is orders of magnitude slower than at the bulk can simulate the anomalous behaviour in sorption curves. The onset times decay rapidly with increasing thickness of the films and scale linearly with the resistance to water transport.

Rangel-Cárdenas, A.L., G.J.M Koper and S.J Picken. Anomalous water sorption kinetics in a carbon-supported Nafion thin-film membrane-electrode assembly. **In preparation.**

3.1. Introduction

The attractiveness of polymer membrane fuel cells (PEMFCs) as a clean energy solution in the market has been widely hampered by their still somewhat expensive character. Performance losses due to contact resistance, fuel crossover (H_2 , CH_4), electro-osmotic drag and water management, i.e. membrane hydration and flooding, have been extensively studied as a means to improve efficiency [1–6]. Nafion™ is the most commonly used proton exchange membrane (PEM) in PEM fuel cells, electrolyzers and other electrochemical devices [7, 8]. This ionomer consists of a hydrophobic poly-tetrafluoroethylene (PTFE) backbone with perfluoroalkyl ether (PFA) side chains terminated in sulfonic acid groups [7–9]. The combination of the hydrophobicity of the backbone with the hydrophilicity of the sulfonic groups gives Nafion the chemical, thermal and proton-exchange properties that have made it the standard for this application.

In this framework, water transport plays a particularly important role as charge transport in the membrane depends heavily on its hydration level [4, 9–11]. Water is fed into the device in the form of humidified gases that must travel through the porous carbon gas diffusion layer (GDL), through the composite catalyst layer – comprised of a combination of catalyst material, electronic support and Nafion binder –, and finally transfer from the electrode into the membrane where it acts as the vehicle for charge transport (see Figure 3.1).

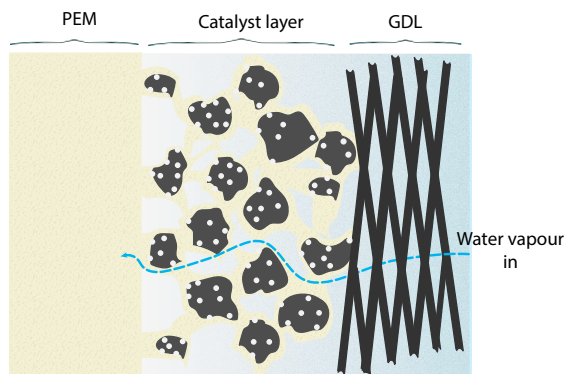


Figure 3.1: Schematic of the water vapour pathway.

However, in this area of study, we systematically fail to account for the interfacial effects and their relation to efficiency losses in energy devices. This is evidenced by the vast amount of studies on different electronic and mass transport properties whose values fall in ranges that differ by orders of magnitude as a consequence of experimental conditions where the interfaces are thought to play a significant role [1, 5, 6, 9, 12, 13]. This brings about the importance of understanding the role of interfacial effects under conditions and geometries that resemble more closely a PEMFC working environment.

It has been suggested that the interfaces affect the overall performance of a fuel

cell as much as the individual components [14] with the water/ionomer interfacial resistance being the primary contributor to losses in the system [2, 15, 16]. The membrane's resistance varies depending on its hydration level and contact between the different materials, which in turn depends on the fabrication method and treatment of the membrane-electrode assembly (MEA) [12]. It is for this reason that it is key to understand interfaces in simple models that can be easily combined with the wide range of experimental conditions that are used to characterize membrane properties.

Water sorption kinetics are routinely studied in polymer science, where the solutions to the diffusion equation are tabulated for a vast range of initial and boundary conditions [17]. Kinetics in humidified polymers commonly follow a Fickian solution where the relative mass of the polymer increases exponentially with time and the average diffusion coefficient can be related to the slope of the exponential (see section 3.3.3). However, despite the number of studies on Nafion bulk membranes, just a handful of studies on water transport properties in Nafion thin-films can be found in the literature. Eastman et al. (2012) [18] studied Nafion thin-films in the range of 20 – 222 nm thickness. They find anomalous water sorption behaviour characterized by a sigmoidal curve that is thickness-dependent, similar to bulk Nafion, and ascribe it to contributions from interfacial transport resistance and restrictions in internal diffusion due to confinement effects. This was evidenced by a sharp turning point at thicknesses <50 – 60 nm in the effective diffusion coefficient. At this short distance, confinement effects were found to be more dominant than interfacial effects, i.e. due to restricted mobility of the polymer. Similarly, Kongkanand (2011) [15] found that at Nafion thickness >500 nm the behaviour of water content in the polymer was very similar to its bulk counterpart. However, at a thickness <33 nm it was found that water content was lower overall and tended to decrease further with increasing water activity, although the reasons why remained unclear. Interactions with the substrate and surface confinement effects were hypothesized as responsible for this characteristic of their films. Furthermore, they find that the interfacial mass transport resistance ($1/k_{int}$) increased with water activity and was a result of contributions from the mass transport resistance at the gas boundary layer ($1/k_{bl}$) and the membrane interfacial resistance ($1/k_{bl}$). While transport at the membrane interface is the primary contributor, it was shown that the gas boundary layer can contribute to as much as 47% to the total interfacial mass-transport coefficient, k_{int} .

Contrastingly, Davis et al. (2014) [8] have measured water diffusion using in-situ polarization modulation infrared reflection absorption spectroscopy (PM-IRRAS), instead of the most common quartz crystal method. They found that the interfacial mass transport is minimally limited as evaluated by the mass-transfer Biot number (Bi), while the effective diffusion coefficient was 4 – 5 orders of magnitude lower than that in bulk membranes. However, it should be noted that this applies for the type of experiment that they have performed, as opposed to other studies that find water transport as mainly governed by interfacial mass transport [15, 18]. Regarding the effect of the substrate, scattered information is available. In some instances, the substrate was found to not affect on water transport properties [15],

while in others the substrate was found to have significant effects [7]. However, by studying several different supports, Abuin et al. [7] found that water uptake of Nafion thin-films in the range of 17 – 1000 nm is independent of thickness when supported in glass, but slightly dependent when supported on Au. Substrates had even bigger effects when they were Si, graphite and ITO with the last two showing the lowest water contents. The effect of the substrate has been put forward before by other authors where neutron reflectometry experiments showed that hydrophobic domains form on the Nafion surface when in contact with Pt and glassy carbon [19–21].

In this work, we observe that in a PEMFC geometry the Fickian solution to the diffusion equation does not apply over the entire time scale but there exists an anomalous behaviour at short times before Fickian diffusion takes off. Thus, we will address the question of whether the polymer/electrode interface is responsible for this anomaly. To find this out, Nafion membranes were cast onto a home-made electrode consisting of platinum catalyst on a carbon GDL that mimics a half fuel cell. This assembly was subjected to water sorption experiments in temperatures from 20 to 80 °C while the relative humidity was varied between 20% and 80%. To distinguish between interfacial and bulk properties, we performed these experiments on assemblies with varying thickness of the Nafion layer, ranging from 1.8 μm to 13.3 μm . We expect that the effect of the interface will be more pronounced on thinner films as their thickness approaches the thickness of the interface [15, 22]. We propose a different, simplified formulation to the problem based on Crank's solution [17] where we consider these two regimes to have different average diffusion coefficients, i.e. at the interface (D_i) and in the bulk (D_b).

3.2. Experimental

3.2.1. Home-made electrode fabrication

Inks with the active material were prepared by stirring 0.9529 g Nafion™ solution (PFSA 5 wt.% in low aliphatic alcohols, Quintech) in 30 ml acetone for 15 minutes. The solution was then dispersed in an ultrasound bath for another 15 minutes where 0.2719 g Pt on Vulcan XC-72 (40%, Sigma Aldrich) were intermittently added to the flask to avoid burning of the catalyst during sonication. The sonication process was then continued for another hour. The resulting ink was sprayed onto a carbon gas diffusion layer (Toray™, Quintech) and left to dry on a hotplate to obtain electrodes with a loading of 1 $\text{mg}\cdot\text{cm}^{-2}$.

3.2.2. MEA preparation and characterization

The membrane-electrode assemblies (MEA) with different membrane thickness were prepared by drop-casting different volumes of Nafion solution (5 wt%, Sigma Aldrich) onto clean home-made Pt electrodes. Before casting, the Pt electrodes were cut into squares of 4 cm^2 and treated under 0.3 mbar in a plasma cleaner for 5 min to ensure a clean surface. Finally, volumes of 0.1, 0.2, 0.3 and 0.6 ml of Nafion solution were cast onto the clean electrodes and left to dry at room temperature in a fume hood. An estimation for the films thickness was calculated by estimating the

amount of solid Nafion spread onto the electrode area and corrected by the weight of solvents.

SEM micrographs of the assemblies were obtained using a JEOL JSM-6010 LA with a standard beam potential of 5 kV. Spot and map analyses were obtained by the energy-dispersive X-ray spectroscopy (EDS) function using the backscatter detector and 20 kV. Finally, the surface roughness of the cast Nafion thin-films was measured using a Dektak 8 stylus profiler (Veeco Instruments).

3.2.3. Water sorption measurements

Circular samples of 5 mm diameter were cut out of the membrane-electrode assemblies and placed inside a TGA Q5000SA (TA Instruments). Water sorption measurements were performed at four temperatures, namely 20 °C, 40 °C, 60 °C and 80 °C. An equilibration time at 60 °C and 1% RH of 1 h was allowed to ensure the sample was free of moisture. Next, the temperature in the chamber was set and the relative humidity was allowed to rise by increments of 20% (i.e. 20%, 40%, 60% and 80% RH were measured at each temperature). At each RH step, the weight change of the sample was measured for a maximum of 300 min unless the change in weight was less than 2 µg for 10 minutes; in this case the next step was immediately activated. At the end of each temperature measurement the RH was allowed to return to 1%. The desorption process continued for 800 minutes and the same condition of weight change of less than 2 µg for 10 minutes applied.

3.3. Results

3.3.1. MEA preparation and characterization

The estimated final Nafion film thicknesses are 1.8 µm, 4.4 µm, 6.7 µm and 13.3 µm. Micrographs of the bare carbon gas diffusion layer (GDL), Pt electrode and a half MEA can be found in Supplementary Information, as well as the mean roughness of the films as measured by AFM. In general, thicker films were less rough as the electrode pores filled with more solution.

3.3.2. Equilibrium water sorption

Figure 3.2 shows a typical mass change vs. time curve where the relative humidity has been stepped up by 20% at 20 °C. The mass change data were used to evaluate the equilibrium water content of the Nafion films as the number of water moles per exchange site ($\text{mol H}_2\text{O}/\text{mol} - \text{SO}_3^-$):

$$\lambda = \frac{m_w M_0}{m_d M_w} \quad (3.1)$$

here M_w and M_0 are the water and Nafion molecular weight ($18.016 \text{ g} \cdot \text{mol}^{-1}$ and $1100 \text{ g} \cdot \text{mol}^{-1}$), respectively.

Water uptake by the Nafion thin-films is shown in figure 3.3 as a fit to a third-degree polynomial as suggested by Springer et al. [4] at 20 °C and 80 °C. It is worth noting that the typical BET pattern would become more clear with the addition

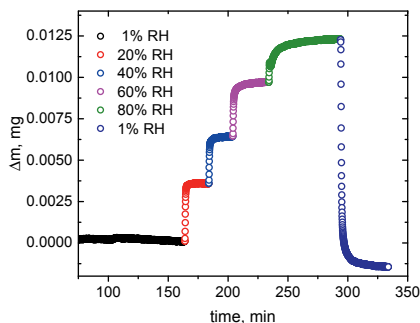


Figure 3.2: Mass change in time in steps of 20% RH at 20 °C

of water uptake at 100 %RH, however as seen in previous work, the correlation between water uptake and water activity is nearly linear in the range of 20 to 80 %RH [7, 15, 23]. Furthermore, measurement at 100 %RH is found to be less reliable due to possible condensation inside the instrument.

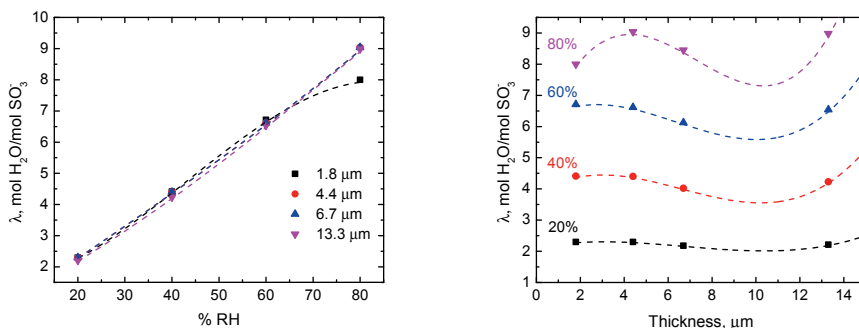


Figure 3.3: Water uptake at 20 °C).

For the thinnest film, i.e. 1.8 μm , water uptake seems to decrease at $\text{RH} \geq 80\%$ opposite to the other films, suggesting an uptake threshold limited by thickness. In figure 3.3b, water uptake as a function of thickness is shown as a fit to a third-degree polynomial. These results suggest indeed a thickness threshold at $\sim 4.4 \mu\text{m}$ that becomes more evident at higher water activity.

3.3.3. Water sorption kinetics

According to Fick's second law, the diffusion equation within the membrane is given by

$$\frac{\partial C}{\partial t} = \frac{\partial}{\partial x} \left(D \frac{\partial C}{\partial x} \right) \quad (3.2)$$

Solutions to this equation have been widely tabulated for a variety of initial and boundary conditions [17]. The simplest solution is obtained by assuming a constant initial concentration ($C = C_0$ at $t = 0$) and a constant concentration at the film surfaces at times $t > 0$. Symmetry of the concentration at the centre of the membrane is assumed. The solution to this equation with fractional weight uptake as a function of time is as follows [24]:

$$\frac{M_t}{M_\infty} \Big|_F = 1 - \sum_{n=0}^{\infty} \frac{8}{(2n+1)^2 \pi^2} \exp \left(- \frac{D_{av} (2n+1)^2 \pi^2 t}{l^2} \right) \quad (3.3)$$

where M_t is the water uptake at time t , M_∞ is the equilibrium water uptake (i.e. at infinite time), D_{av} is the effective diffusion coefficient ($cm^2 \cdot s^{-1}$) averaged over the concentration interval and l is the film total thickness (cm). This solution is the classical Fickian solution and represents the weight uptake of a penetrant that enters due to the concentration gradient created by the initial surface concentration [25]. This solution is known to describe the kinetic sorption behaviour of relatively non-condensable gases in polymer materials and some vapours at low activity [24] and is widely used in polymer science [24–26].

The kinetics of water sorption is shown in figure 3.4 as a plot of the normalized mass change in a relative humidity step from 1-20% at 20 °C versus the square root of diffusion time scaled by a) the film thickness, and b) the thickness squared. Scaling by the thickness or thickness squared would collapse sorption curves into one single master curve if the diffusion coefficients were independent of the film thickness and governed by either internal or interface diffusion. In contrast, neither scaling collapses the sorption curve suggesting that there is more than one contribution to the thickness-dependent transport at these length scales. This agrees with what other authors have found on nanometric and bulk Nafion membranes [18, 27], where transport resistance at the interface and confinement effects are responsible for this behaviour [15, 18].

The thickness dependence also seems to affect the onset time to Fickian diffusion, i.e. the linear part of the water sorption curves. This anomalous behaviour where diffusion does not follow the Fickian pattern has been observed before in Nafion films as well as in other glassy polymers [18, 28]. Authors have attributed its causes to water clustering in the polymer channels, surface concentration variability, confinement effects or instrument control lag. Furthermore, this behaviour is not constrained only to the beginning of sorption but to any regime where a deviation from linearity exists and the relative magnitude of the rates of diffusion and relaxation processes are determinant in the anomalous effects [8, 18, 24, 25, 28].

Despite the anomalous behaviour, the Fickian regime can be used to estimate an average diffusion coefficient. Equation 3 can be solved by iterative calculations and lead to a best-fit of the experimental data. Alternatively, it can also be solved in different domains, i.e. the linear and exponential parts of the curve. In the present

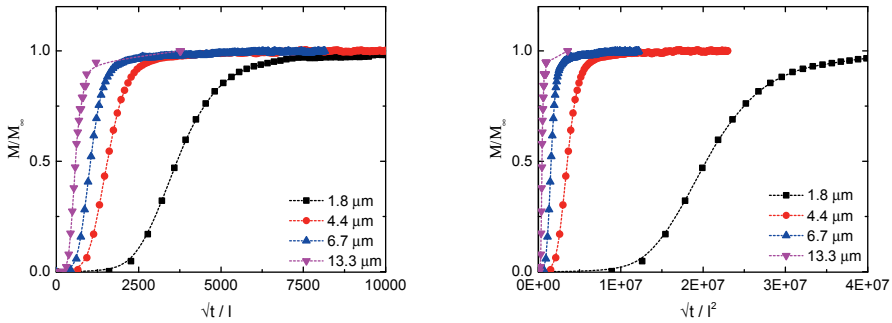


Figure 3.4: Water sorption curves scaled by l and l^2 , respectively.

work, an estimation of the average diffusion coefficient in the Nafion thin-films was done by approximation of equation 3 to its solution in the linear domain at values of $M_t/M_\infty < 0.5$ [28]:

$$\frac{M_t}{M_\infty} \Big|_F = \frac{4}{l} \sqrt{\frac{D_{av} t}{\pi}} \quad (3.4)$$

The average diffusion coefficient was determined for all films in the range of 1 – 80% relative humidity. An example of this analysis at 20 °C is shown in figure 3.5. Here it is clear that at larger thicknesses the effect of relative humidity on diffusion is more pronounced, while in the thinnest film it seems to be independent on hydration of the membrane. These results suggest either confinement effects in the polymer film or increasing interfacial resistance at smaller thicknesses. As confinement effects have been reported to be significant at the nanometric scale, well below a 500 nm threshold [8, 15, 18], we believe that at the micron scale interfacial effects are more likely to be the determining step. Especially if we consider that at thicknesses > 10 nm, where films are considered to have more of a bulk-like behaviour [15, 22], we also observe improved diffusion with water content.

Furthermore, diffusion tends to decrease with increasing relative humidity. This effect is more evident in figure 3.5 where D_{av} is shown against %RH for all film thicknesses. Typically, diffusion would increase as the polymer becomes more hydrated and resistance to water transport decreases, however, Nafion is a polymer that can be thought of as a bi-continuous emulsion, with hydrophobic and hydrophilic domains that create a network of pockets interconnected by channels. The water mobility in these two regions is likely to be different thus making it possible that the rate-determining step is the water transfer in and out of the channels, which primarily accumulate water at low and medium water activities [23]. Studies on porous materials such as $CaCl_2$ -in-silica-gel have shown water sorption kinetics such as seen in our experiments with the slope of the sorption curve decreasing with water content and has been attributed to increased pore tortuosity

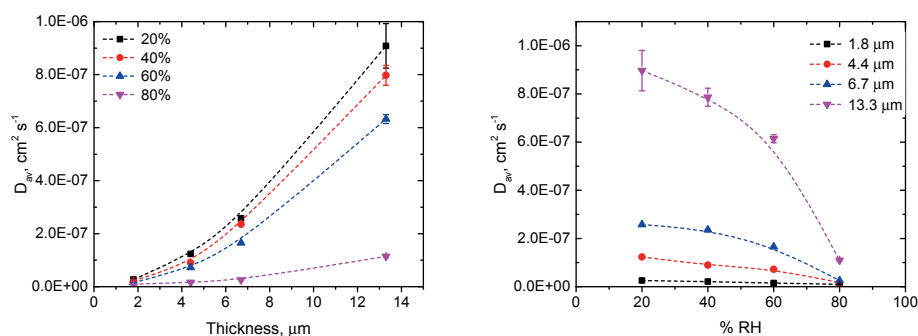


Figure 3.5: D_{av} variation with thickness (left) and % RH (right).

caused by interactions of water molecules with the salt [29]. Even though, the opposite behaviour has been observed in Nafion thin-films [6], it should be noted that these studies were done on self-supporting films or films cast onto a QCM substrate. Contradictory opinions are found in the literature on the effect of the substrate in water sorption. In one study, the quartz support of the microbalance has been coated with either Au or Pt before Nafion casting with no major effect on water sorption kinetics [15]. However, as the metals were deposited onto the same kind of quartz crystal, the morphology and microstructure of the substrate essentially did not change. Abuin et al. [7] did a more comprehensive study on the effect of different substrates with different morphologies and found that graphite and ITO supports yielded the lowest water contents in their Nafion thin-films. In our case, Nafion films were cast onto an electrode consisting of a porous carbon substrate that was subsequently coated with a platinum layer. This electrode substrate was then plasma-cleaned before Nafion film casting. The plasma cleaning process in particular aids with making surfaces hydrophilic which ultimately may result in an orientation of the Nafion hydrophilic domains towards the substrate, while the hydrophobic domains end up oriented towards the surface in contact with water vapour. The most common morphologies of block copolymers are lamellar and cylindrical packing of ionic and non-ionic phases. In the case of Nafion, several studies have shown layering in hydrophobic/hydrophilic planar clusters, or stratification, depending on various factors such as membrane thickness or substrate's surface energy [14, 19, 22, 30–33]. For instance, da Silva et al. [30] have recently shown a SAXS signature pattern for lamellar phase separation of the ionic domains in Nafion. Aided by infrared spectroscopy and wide-angle X-ray scattering (WAXS), they conclude that lamellar arrangement is the most representative morphology of Nafion. Furthermore, Dura et al. [19] studied interfacial structures of Nafion at the substrate boundary by neutron reflectivity. They found that Nafion lamellae formation was dependent on the substrate, observing multilamellar structures in SiO_2 substrates, while only a single water-rich lamella was observed on Pt and Au

substrates. However, Kim et al. [14] have claimed that interfacial structures seem to be strongly dependent on surface energy, resulting in no lamellae observed on hydrophobic surfaces and interfacial lamellae formation on hydrophilic substrates. In summary, it follows that a combination of ion cluster formation at low hydration levels and the resistance at the surface likely due to the hydrophobicity inflicted by interfacial polymer stratification might prevent water diffusion more strongly in thinner films. We can rationalize that the thinner the film, the higher the hydrophobic lamella thickness to total thickness ratio, thus the more resistance to water sorption and the faster the film saturation with water, thereby providing an explanation for the behaviour we observe. Even though, more experimental data would be necessary to prove the existence of a stratified surface, e.g. SAXS experiments, we will discuss further support in this direction in section 3.3.5.

3.3.4. Interfacial effects in a simplified mathematical model

Diffusion in two steps as seen in the sigmoidal curves in figure 3.4 has been observed in glassy polymers before such as PHEMA membranes (poly(2-hydroxyethyl methacrylate)), chitosan, PET and PEF [24, 25, 28]. In addition, this sigmoidal behaviour has also been reported in porous media and attributed to increased tortuosity within the water pores [29].

Even though the second step may be well explained by Fickian diffusion, the relationship between the interface and non-fickian behaviour has been less explored in Nafion thin-films [15, 27]. A few models have been used to explain the sigmoidal nature of water sorption in other glassy polymers such as the one proposed by Long and Richman [34] where the water concentration at the surface is considered to be variable. The model proposed by Berens and Hopfenberg [35] considers the sorption process to be a linear superposition of independent contributions from Fickian diffusion and polymeric relaxation. And a third model, the diffusion-reaction model, considers the penetrant to be distributed in two types of sorption modes, one that allows penetrant to diffuse freely, and one that immobilizes the sorbed penetrant limiting its movement. The key assumption in this model is that the transfer between two modes is equivalent to a first-order reversible reaction [36].

However, the role of the vapour/Nafion interface in an actual fuel cell configuration has not been studied to the best of our knowledge. Here, we propose a simplified model where the two time constants in the sigmoidal curve correspond to regions with different average diffusion coefficients, i.e. the interface and bulk. We consider the interface and bulk to be two subsequent polymer slabs so that the diffusion equation (3.2) can be differenced as follows:

$$\frac{(u_j^{n+1} - u_j^n)}{\Delta t} = \frac{D}{2} \left[\frac{(u_{j+1}^{n+1} - 2u_j^{n+1} + u_{j-1}^{n+1}) + (u_{j+1}^n - 2u_j^n + u_{j-1}^n)}{(\Delta x)^2} \right] \quad (3.5)$$

Which is a forward time-centred scheme (FCTS) averaged on its explicit and implicit forms thus combining the accuracy of the explicit, and the second order in time and space of the implicit. This is the Crank-Nicolson scheme which is centred at timestep $n + 1/2$ and is stable for any size of Δt . This can be solved by a set of

simultaneous linear equations at each timestep for u_j^{n+1} . What turns this into a simple problem is the fact that the system can be written as a tridiagonal matrix by grouping the terms appropriately:

$$-\alpha u_{j-1}^{n+1} + 2(1 + \alpha)u_j^{n+1} - \alpha u_{j+1}^{n+1} = \alpha u_{j-1}^n + 2(1 - \alpha)u_j^n + \alpha u_{j+1}^n, \quad j = 1, 2, \dots, J - 1 \quad (3.6)$$

Where u represents the concentration, and

$$\alpha \equiv \frac{D\Delta t}{(\Delta x)^2} \quad (3.7)$$

Defining new parameters

$$b = c = \alpha \quad (3.8)$$

$$a = 2(1 + \alpha) \quad (3.9)$$

$$d_j = \alpha u_{j-1}^n + 2(1 + \alpha)u_j^n + \alpha u_{j+1}^n = c(u_{j-1}^n) + 2(1 - c)u_j^n + bu_{j+1}^n \quad (3.10)$$

Then

$$-c(u_{j-1}^{n+1}) + au_j^{n+1} - bu_{j+1}^{n+1} = d_j \quad (3.11)$$

Note that a, b, c are constant coefficients, while d_j varies with the index. The main diagonal is a ; the sub-diagonal is b ; c is the super-diagonal. The right-hand side (RHS) vector is d_j . This system can be solved by tridiagonal matrix algorithm (also known as Thomas algorithm) which is a simplified form of Gaussian elimination (for further reading refer to Numerical Recipes, ch. 20.2 [37]).

The system was solved using the initial condition

$$u(+l/2 < x < -l/2, t = 0) = 0 \quad (3.12)$$

And boundary conditions

$$u(\pm l/2, t > 0) = u_0 \quad (3.13)$$

$$D(\pm l/2, t) = \frac{Bi}{l} D_b = D_i \quad (3.14)$$

Where D_i and D_b are the average diffusion coefficients at the interface and bulk, respectively. These are related by Biot's number, defined as the ratio of the internal and interfacial resistances, $Bi = R_b/R_i$. Assuming thickness to be unity, when $Bi = 1$, then the Fickian solution shown in equation 3.3 is obtained. Figure 3.6 shows the effect of decreasing Bi down to $1E-06$. As Bi decreases, i.e. interfacial resistance increases, the sigmoidal behaviour that was seen earlier becomes more evident. This is the equivalent of making the interfacial resistance 10^3 times larger than the internal resistance, showing that the anomalous water sorption behaviour is at least partially caused by the vapour/Nafion interface.

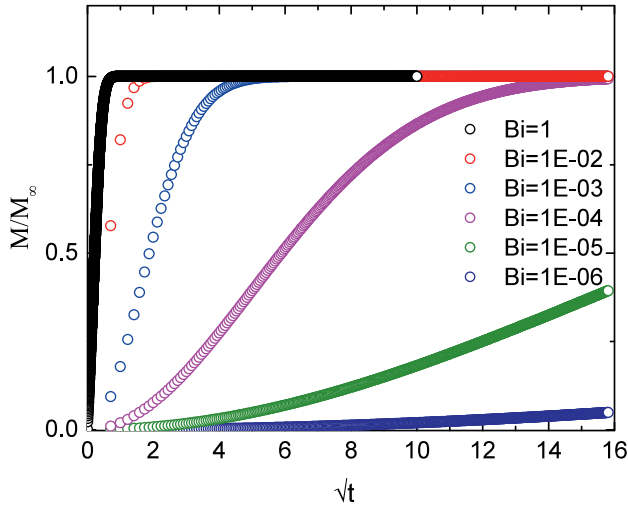


Figure 3.6: Simulation of water sorption curves with varying Bi number.

3.3.5. Analysis of interfacial effects

The most important inhomogeneities in an MEA are the surfaces that are in contact with the electrodes or with water vapour. A well-known phenomenon that can be used to characterize these inhomogeneities is the “contact resistance” between two materials where transport of some kind occurs. Following Bedeaux and Kjelstrup [38, 39] a relatively successful, thermodynamically consistent, approach to describe interfacial inhomogeneities consists of considering the membrane to be composed of a uniform central “bulk” material between two thin interfacial layers. The fluxes are considered to be continuous through the layers and hence the “resistance” of the individual layers are additive [12]:

$$\mathbf{L}_{tot}^{-1} = \frac{l_i \mathbf{L}_i^{-1} + d \mathbf{L}_b^{-1} + l_i \mathbf{L}_i^{-1}}{l_i + d + l_i} \quad (3.15)$$

where \mathbf{L}^{-1} is the inverse of any transport coefficient and represents the resistivity of the membrane; l is the thickness of the interface layer, d is the thickness of the bulk, and the suffixes i and b denote the interface and bulk. The thicknesses of the interfacial layers are generally not known and remain integrated within the coefficient matrix of the layers.

Considering the resistance to water transport to be the inverse of water permeation through the membrane, it follows that:

$$\frac{l_m}{P_{w,m}} = \frac{(2l_i)}{P_{w,i}} + \frac{l_b}{P_{w,b}} \quad (3.16)$$

where P_w is the water permeation coefficient and the suffix m denotes the measured values. The experimentally measured permeability and the diffusion coefficient are related by the solubility:

$$P_w = \frac{D_w}{p_w V_w} \quad (3.17)$$

where p_w is the water partial pressure and V_w is the water volume. Then equation 3.16 can be written as:

$$(p_{w,m} V_{w,m}) \frac{l_m}{D_m} = (p_{w,i} V_{w,i}) \frac{2l_i}{D_i} + (p_{w,b} V_{w,b}) \frac{l_b}{D_b} \quad (3.18)$$

Assuming the partial pressure to be uniform across the membrane at a given temperature (constant solubility), then we define the interfacial resistance coefficient:

$$\beta = \frac{2l_i}{D_i} \quad (3.19)$$

Estimations of D_b have been done using the diffusion coefficient expression given by Fuller [40] as a function of λ and temperature (in K)

$$D_{w,f} = 2.1 \times 10^{-3} \lambda \exp(-2436/T) \quad (3.20)$$

In figure 3.7, the change in the interfacial resistance coefficient, β , with water content, λ , is depicted for water sorption measurements at 20 °C. The interfacial effects are more pronounced on the thinnest film except for the 6.7 μm film. At this thickness and for $\lambda > 6$, the interfacial effects increase rapidly with increasing hydration of the membrane. A similar effect was observed in figure 3.5b and 3.3b where D_{av} decreased with increasing hydration of the membrane and there seemed to be a transition region between 4 – 6 μm . The increase in the interfacial resistance coefficient with λ , supports the theory of increased pore tortuosity by transport limitations in water pockets and the hydrophobic polymer surface by stratification near it.

Furthermore, increasing thickness of the films decreases the interfacial resistance coefficient rapidly following a power decay with a rate between 0.78 – 0.87 as shown in figure 3.7b. From the coefficient β an estimation of the average diffusion coefficient at the interface, D_i , can be done by giving the interface a certain thickness. For the purpose of our analysis, we shall assume an interfacial thickness of 5 nm, which is not an unreasonable length scale considering studies that suggest the ionomer/Pt interface to extend a few (to tens of) nanometres [14, 20, 41]. Even more, recently this interface and its degradation has been visualized by high-resolution STXM where it seemingly extends just a few nm [42]. The results of the change in the average diffusion coefficient at the interface with thickness of the films are shown in figure 3.7c.

This estimation shows a sharp decrease in D_i between 4.4 – 6.7 μm , consistent with the average diffusion coefficient (see figure 3.5a) which increases further at thicknesses $> 6.7 \mu\text{m}$ as water content increases too (see figure 3.3a).

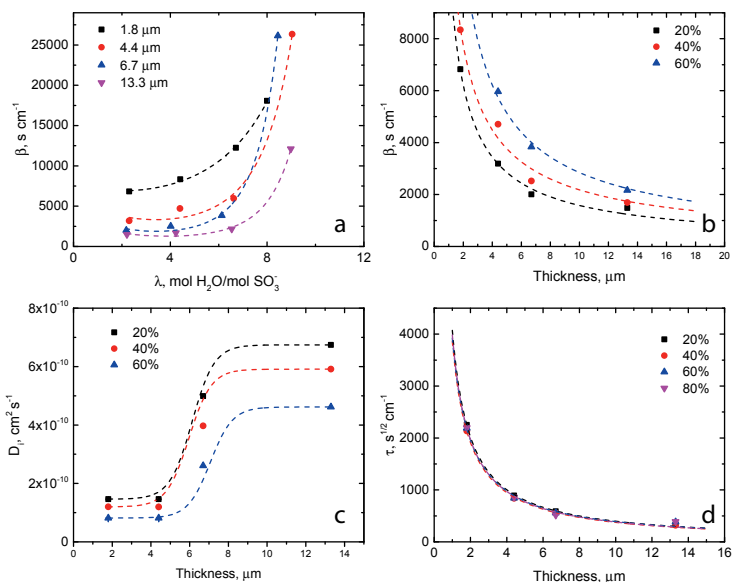


Figure 3.7: a) Interfacial resistance coefficient vs. water content and b) vs. film thickness; c) interfacial diffusion coefficient vs. thickness; d) onset time vs. thickness

Finally, the resistance of the film can be evaluated in terms of the onset time to Fickian diffusion in the water sorption curves, defined as $\tau = \sqrt{\bar{t}}/l$. The onset time increases linearly with interfacial resistance (see figure S4). In figure 3.7d, the onset time against thickness is presented. Regardless of water activity (or hydration of the membrane), the delay to Fickian diffusion decays rapidly with an increasing thickness (at a rate of ~ 0.88), meaning thicker membranes approach bulk diffusion faster, and likewise validating the study of interfaces at film thicknesses of a few μ m ($< 6.7 \mu$ m).

3.4. Discussion

Water sorption kinetics on supported Nafion thin-films has been studied by casting membranes with varying thickness onto a Pt/GDL electrode in a similar fashion to an MEA in a PEM fuel cell. We find that these Nafion thin-films hydrate mostly similar to self-supporting membranes following a BET pattern. However, we find hydration to be a function of the thickness with suggestions of a threshold in the region between 4.4 – 6.7 μ m. Furthermore, the kinetics of water sorption show an anomalous behaviour that deviates from Fickian diffusion at small time scales. As a result, sigmoidal curves that are strongly dependent on thickness are characteristic of water sorption in Nafion thin-films supported on a typical FC electrode. We find

that this anomaly can be explained by the existence of two regimes where the average diffusion coefficient takes different values, i.e. bulk and interface. We find that simulations with a diffusion coefficient at the interface that is orders of magnitude lower than that at the bulk of the membrane can reproduce the sigmoidal shape seen in our experiments.

Further analysis of the interface shows that the interfacial resistance increases significantly as the thickness of the film decreases, following a power law with a rate of ca. 0.78 – 0.87. At the same time, estimations of the average interfacial diffusion coefficient, D_i , corroborate the existence of a transition region between 4.4 and 6.7 μm , with D_i decreasing sharply below this region. This is consistent with our findings on hydration of the films where we saw that above 6.7 μm , water content (λ) and therefore the average diffusion coefficient (D_{av}) increase at a faster rate. Our observations of the tendency of D_{av} to decrease with increased water activity can be explained by the known limitations at low hydration levels due to transport in and out of water pockets formed in Nafion membranes [23] and the resistance exerted by a possibly stratified outer layer. This phenomenon is supported by the fact that the interfacial resistance coefficient (β) also increases as the membrane becomes more hydrated. Even though, stratification at the surface has not been investigated in the present work, there is strong evidence from our results and previous findings on Nafion's tendency to form stratified layers to believe this to be a contributing factor on the increased resistance found in thinner films. Finally, the resistance of the membrane to water transport can be assessed in terms of the delay time to Fickian diffusion (τ) that follows a power decay with increasing thickness and scales linearly with the interfacial resistance coefficient (β).

In general, we find that the interfaces are responsible for the anomalous water sorption behaviour and the effects of the interfaces become significantly stronger as thickness is decreased further. To illustrate this effect, figure 3.8 shows a comparison of our results and diffusion coefficient values found in the literature at different thicknesses of the membrane. There is a remarkable difference of almost seven orders of magnitude between the smallest thickness reported (of a few nm) and standard Nafion membranes of $\sim 180 \mu\text{m}$ thickness. In our work, where Nafion thin-films have been cast on a Pt electrode and GDL, we find that $< \text{ca. } 4.4 \mu\text{m}$ thickness the effects of the interface are more pronounced, while effects above 6.7 μm are more bulk-like.

3.5. Conclusion

In short, we have studied Nafion water sorption kinetics in a geometry that resembles that of a PEM fuel cell by using a Pt/C/GDL support and intermediate thicknesses of the Nafion films, i.e. where confinement effects are not thought to play a role ($< 500 \text{ nm}$) and bulk behaviour is not dominant ($> 10 \mu\text{m}$). Studies of the Nafion/vapour interface in a membrane electrode assembly have revealed anomalous water sorption behaviour as opposed to self-standing membranes that can be found in the literature. This behaviour can be explained by interfacial resistance to water transport as the existence of a regime near the surfaces where the aver-

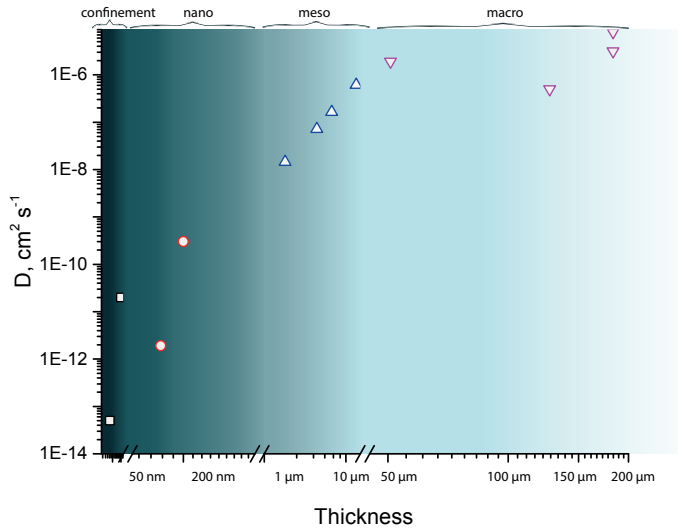


Figure 3.8: Water diffusion coefficient in Nafion membranes as a function of thickness. 20 nm [23], 50 nm [18], 176 nm [8], 200 nm [18], 1.8 to 13.3 μm (this work), 50.8 μm [43], 127 μm [43], 183 μm [11], 183 μm [44]

age diffusion coefficient is orders of magnitude lower than that at the bulk of the membrane. We find that these interfacial effects become significantly stronger at smaller thicknesses as assessed by the average interfacial diffusion coefficient (β) and the delay time (τ). For Nafion thin-films supported on a Pt/C/GDL electrode, these effects become stronger at $l < 4.4 \mu\text{m}$, and at $l > 6.7 \mu\text{m}$ the behaviour is more bulk-like.

Appendix

3.A. SEM micrographs of electrodes

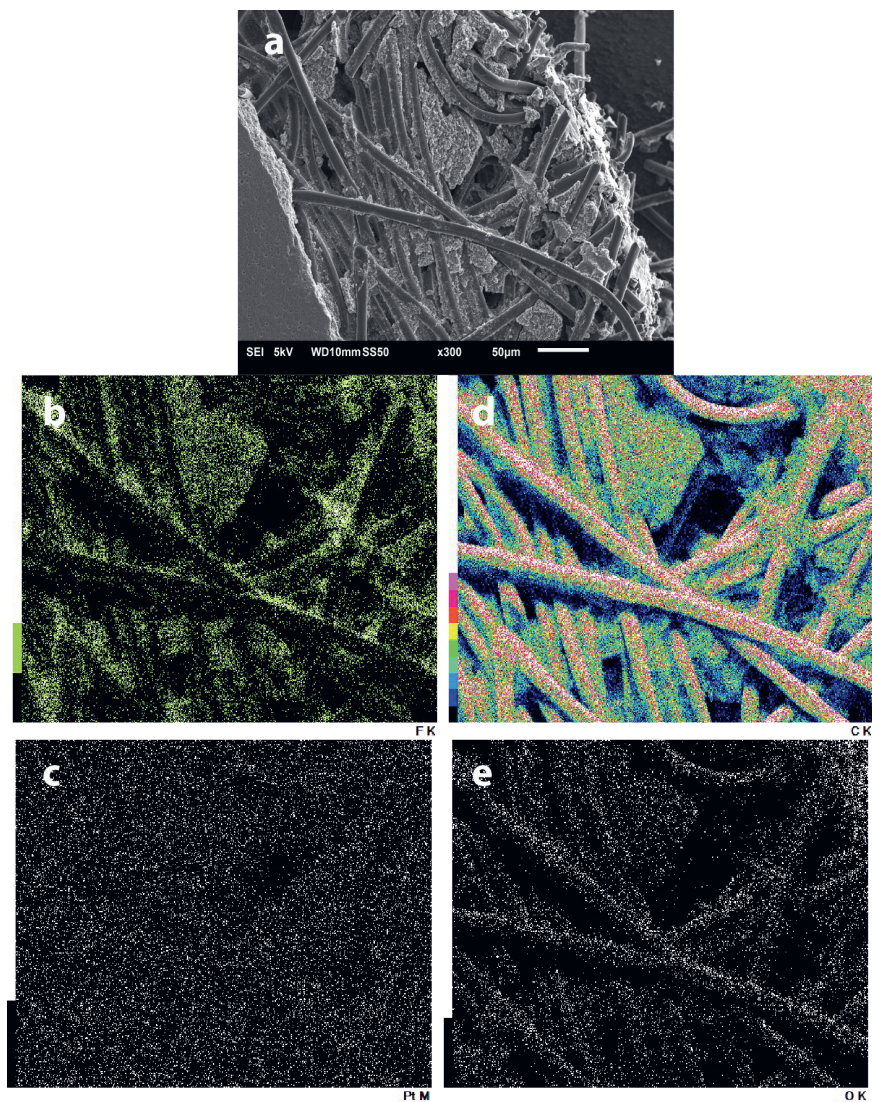


Figure 3.9: SEM micrographs of a) scraped electrode and b-e) elemental mapping.

3.B. SEM micrographs pristine electrode vs. MEA

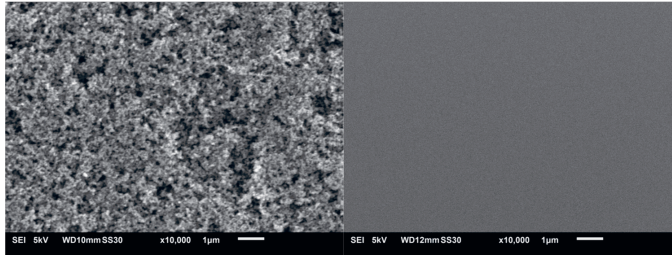


Figure 3.10: SEM micrographs of (a) pristine electrode and (b) electrode after Nafion film casting.

3.C. Mean surface roughness

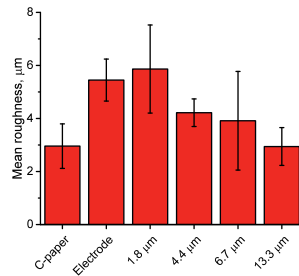


Figure 3.11: Mean surface roughness.

3.D. Onset time as a function of interfacial resistance

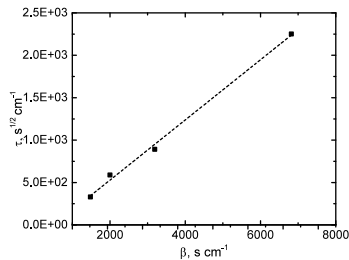


Figure 3.12: Onset time vs. interfacial coefficient resistance. $R^2=0.9949$.

References

- [1] M. J. Cheah, I. G. Kevrekidis, and J. Benziger, "Effect of interfacial water transport resistance on coupled proton and water transport across Nafion," *Journal of Physical Chemistry B*, vol. 115, no. 34, pp. 10239–10250, 2011.
- [2] P. W. Majsztrik, M. B. Satterfield, A. B. Bocarsly, and J. B. Benziger, "Water sorption and transport in Nafion membranes," *ECS Transactions*, vol. 11, no. 1 PART 1, pp. 609–621, 2007.
- [3] D. Rivin, C. E. Kendrick, P. W. Gibson, and N. S. Schneider, "Solubility and transport behavior of water and alcohols in Nafion™," *Polymer*, vol. 42, no. 2, pp. 623–635, 2001.
- [4] T. E. Springer, T. A. Zawodzinski, and S. Gottesfeld, "Polymer Electrolyte Fuel Cell Model," *Journal of the Electrochemical Society*, vol. 138, no. 8, pp. 2334–2342, 1991.
- [5] Thomas A. Zawodzinski Jr., D. Charles, R. Susan, J. S. Ruth, T. S. Van, E. S. Thomas, and G. Shimshon, "Water Uptake by and Transport Through Nafion^{[sup [registered sign]]} 117 Membranes," *Journal of the Electrochemical Society*, vol. 140, no. 4, pp. 1041–1047, 1993.
- [6] Q. Zhao, P. Majsztrik, and J. Benziger, "Diffusion and interfacial transport of water in Nafion," *Journal of Physical Chemistry B*, vol. 115, no. 12, pp. 2717–2727, 2011.
- [7] G. C. Abuin, M. Cecilia Fuertes, and H. R. Corti, "Substrate effect on the swelling and water sorption of Nafion nanomembranes," *Journal of Membrane Science*, vol. 428, pp. 507–515, 2013.
- [8] E. M. Davis, C. M. Stafford, and K. A. Page, "Elucidating water transport mechanisms in nafion thin films," *ACS Macro Letters*, vol. 3, no. 10, pp. 1029–1035, 2014.
- [9] K.-D. Kreuer, S. J. Paddison, E. Spohr, and M. Schuster, "Transport in Proton Conductors for Fuel-Cell Applications," *Chemical Reviews*, vol. 104, no. 10, pp. 4637–4678, 2004.
- [10] C. H. Lee, H. B. Park, Y. M. Lee, and R. D. Lee, "Importance of proton conductivity measurement in polymer electrolyte membrane for fuel cell application," *Industrial and Engineering Chemistry Research*, vol. 44, no. 20, pp. 7617–7626, 2005.
- [11] T. A. Zawodzinski, M. Neeman, L. O. Sillerud, and S. Gottesfeld, "Determination of water diffusion coefficients in perfluorosulfonate ionomeric membranes," *Journal of Physical Chemistry*, vol. 95, no. 15, pp. 6040–6044, 1991.
- [12] A. L. Rangel-Cárdenas and G. J. Koper, "Transport in Proton Exchange Membranes for Fuel Cell Applications—A Systematic Non-Equilibrium Approach," *Materials*, vol. 10, no. 6, p. 576, 2017.

- [13] Z. Xie, C. Song, B. Andreaus, T. Navessin, Z. Shi, J. Zhang, and S. Holdcroft, "Discrepancies in the measurement of ionic conductivity of PEMs using two- and four-probe AC impedance spectroscopy," *Journal of the Electrochemical Society*, vol. 153, no. 10, pp. 6–11, 2006.
- [14] S. Kim, K. A. Page, and C. L. Soles, "Structure and properties of proton exchange membrane fuel cells at interfaces," *ACS Symposium Series*, vol. 1096, pp. 267–281, 2012.
- [15] A. Kongkanand, "Interfacial water transport measurements in Nafion thin films using a quartz-crystal microbalance," *Journal of Physical Chemistry C*, vol. 115, no. 22, pp. 11318–11325, 2011.
- [16] S. Didierjean, J. C. Perrin, F. Xu, G. Maranzana, M. Klein, J. Mainka, and O. Lottin, "Theoretical evidence of the difference in kinetics of water sorption and desorption in Nafion® membrane and experimental validation," *Journal of Power Sources*, vol. 300, pp. 50–56, 2015.
- [17] J. W. Westwater and H. G. Drickamer, "The Mathematics of Diffusion," *Journal of the American Chemical Society*, vol. 79, no. 5, pp. 1267–1268, 1957.
- [18] S. A. Eastman, S. Kim, K. A. Page, B. W. Rowe, S. Kang, C. L. Soles, and K. G. Yager, "Effect of confinement on structure, water solubility, and water transport in Nafion thin films," *Macromolecules*, vol. 45, no. 19, pp. 7920–7930, 2012.
- [19] J. A. Dura, V. S. Murthi, M. Hartman, S. K. Satija, and C. F. Majkrzak, "Multilamellar interface structures in Nafion," *Macromolecules*, vol. 42, no. 13, pp. 4769–4774, 2009.
- [20] D. L. Wood, J. Chlistunoff, J. Majewski, and R. L. Borup, "Nafion structural phenomena at platinum and carbon interfaces," *Journal of the American Chemical Society*, vol. 131, no. 50, pp. 18096–18104, 2009.
- [21] V. S. Murthi, J. Dura, S. Satija, and C. Majkrzak, "Water Uptake and Interfacial Structural Changes of Thin Film Nafion® Membranes Measured by Neutron Reflectivity for PEM Fuel Cells," *ECS Transactions*, pp. 1471–1485, 2008.
- [22] M. A. Modestino, D. K. Paul, S. Dishari, S. A. Petrina, F. I. Allen, M. A. Hickner, K. Karan, R. A. Segalman, and A. Z. Weber, "Self-assembly and transport limitations in confined nafion films," *Macromolecules*, vol. 46, no. 3, pp. 867–873, 2013.
- [23] P. Krtil, A. Trojánek, and Z. Samec, "Kinetics of water sorption in nafionthin films - Quartz crystal microbalance study," *Journal of Physical Chemistry B*, vol. 105, no. 33, pp. 7979–7983, 2001.
- [24] S. K. Burgess, D. S. Mikkilineni, D. B. Yu, D. J. Kim, C. R. Mubarak, R. M. Kriegel, and W. J. Koros, "Water sorption in poly(ethylene furanoate) compared

- to poly(ethylene terephthalate). Part 2: Kinetic sorption," *Polymer*, vol. 55, no. 26, pp. 6870–6882, 2014.
- [25] Y. M. Sun, "Sorption/desorption properties of water vapour in poly(2-hydroxyethyl methacrylate): 2. Two-stage sorption models," *Polymer*, vol. 37, no. 17, pp. 3921–3928, 1996.
- [26] Y. M. Sun and H. L. Lee, "Sorption/desorption properties of water vapour in poly(2-hydroxyethyl methacrylate): 1. Experimental and preliminary analysis," *Polymer*, vol. 37, no. 17, pp. 3915–3919, 1996.
- [27] M. B. Satterfield and J. B. Benziger, "Non-Fickian water vapor sorption dynamics by nafion membranes," *Journal of Physical Chemistry B*, vol. 112, no. 12, pp. 3693–3704, 2008.
- [28] P. Bébin and R. Prud'Homme, "Effect of comp drif," *Journal of Polymer Science Part B: Polymer Physics*, vol. 39, no. 1, pp. 2363–2377, 2001.
- [29] Y. I. Aristov, I. S. Glaznev, A. Freni, and G. Restuccia, "Kinetics of water sorption on a CaCl₂-in-silica-gel-pores sorbent: The effects of the pellet size and temperature," *Kinetics and Catalysis*, vol. 47, no. 5, pp. 770–775, 2006.
- [30] J. S. da Silva, S. G. M. Carvalho, R. P. da Silva, A. C. Tavares, U. Schade, L. Puskar, F. C. Fonseca, and B. R. Matos, "SAXS signature of the lamellar ordering of ionic domains of perfluorinated sulfonic-acid ionomers by electric and magnetic field-assisted casting," *Physical Chemistry Chemical Physics*, vol. 22, no. 24, pp. 13764–13779, 2020.
- [31] H.-G. Haubold, T. Vad, H. Jungbluth, and P. Hiller, "Nano structure of NAFION: a SAXS study," *Electrochimica Acta*, vol. 46, pp. 1559–1563, mar 2001.
- [32] A.-L. Rollet, O. Diat, and G. Gebel, "A new insight into nafion structure," *The Journal of Physical Chemistry B*, vol. 106, pp. 3033–3036, mar 2002.
- [33] J. Zheng, Q. He, C. Liu, T. Yuan, S. Zhang, and H. Yang, "Nafion-microporous organic polymer networks composite membranes," *Journal of Membrane Science*, vol. 476, pp. 571–579, feb 2015.
- [34] F. A. Long and D. Richman, "Concentration Gradients for Diffusion of Vapors in Glassy Polymers and their Relation to Time Dependent Diffusion Phenomena," *Journal of the American Chemical Society*, vol. 82, no. 3, pp. 513–519, 1960.
- [35] A. R. Berens and H. B. Hopfenberg, "Diffusion and relaxation in glassy polymer powders: 2. Separation of diffusion and relaxation parameters," *Polymer*, vol. 19, no. 5, pp. 489–496, 1978.
- [36] Y. S. Kang, J. H. Meldon, and N. Sung, "Transport of hexane vapor in polystyrene at 25°C i. analysis of integral sorption data," *Journal of Polymer Science Part B: Polymer Physics*, vol. 28, pp. 1093–1103, jun 1990.

- [37] B. P. Press, William H.; Teukolsky, Saul A.; Vetterling, William T.; Flannery, *Numerical Recipes - The art of Scientific Computing*. Cambridge University Press, 2007.
- [38] D. Kjelstrup, S.; Bedeaux, *Non-equilibrium thermodynamics of Heterogeneous Systems*. World Scientific, 2008.
- [39] S. Kjelstrup, D. Bedeaux, E. Johannesen, and J. Gross, "Non-equilibrium thermodynamics for engineers," in *Non-Equilibrium Thermodynamics for Engineers*, pp. 1–5, WORLD SCIENTIFIC, mar 2017.
- [40] T. F. Fuller, *Solid-Polymer-Electrolyte Fuel Cells*. PhD thesis, University of California, 1992.
- [41] I. Yagi, K. Inokuma, K. Kimijima, and H. Notsu, "Molecular Structure of Buried Perfluorosulfonated Ionomer/Pt Interface Probed by Vibrational Sum Frequency Generation Spectroscopy," *Journal of Physical Chemistry C*, vol. 118, no. 45, pp. 26182–26190, 2014.
- [42] I. Martens, L. G. A. Melo, M. M. West, D. P. Wilkinson, D. Bizzotto, and A. P. Hitchcock, "Imaging Reactivity of the Pt – Ionomer Interface in Fuel-Cell Catalyst Layers," *ACS Catalysis*, 2020.
- [43] Y. S. Kim and K.-S. Lee, "Fuel cell membrane characterizations," *Polymer Reviews*, vol. 55, pp. 330–370, apr 2015.
- [44] C. Edmondson, J. Fontanella, S. Chung, S. Greenbaum, and G. Wnek, "Complex impedance studies of s-SEBS block polymer proton-conducting membranes," *Electrochimica Acta*, vol. 46, pp. 1623–1628, mar 2001.

4

Proton exchange in spinel LiMn_2O_4 for ORR in acidic environments - Structure and activity insights

*In the long history of humankind those who learned to
collaborate and improvise most efficiently have prevailed.*

Charles Darwin, *The Origin of Species*

Rangel-Cárdenas, A. L., S. Ganapathy, G.J.M. Koper, S.J. Picken, M. Wagemaker and E.M. Kelder. Proton exchange in spinel LiMn_2O_4 for ORR in acidic environments characterized by neutron diffraction and solid state NMR. ***In preparation***

Despite their recent re-found popularity as green energy technology, PEM fuel cells still have various obstacles to overcome. One of their most relevant downsides is still their high cost due to the use of precious metals as electrocatalysts. A lot of research is focused on ways to lower Pt loading in electrodes or in finding alternative materials. Transition metal oxides (TMOs) as an alternative in similar electrochemical systems have gained a lot of attention recently due to their availability and low cost. Different TMOs have been studied for alkaline fuel cells, photoelectrochemical water oxidation, among other applications. In spite of the good prospects offered by these materials, research of their use as electrocatalysts in PEMFCs is not common. Here we present a spinel-type material with formula $\text{H}_z\text{Li}_{1-x}\text{Mn}_2\text{O}_4$ (HLMO). We have protonated a cubic spinel LiMn_2O_4 through an ion-exchange reaction in acid. Proton insertion in the crystal lattice of the spinels was confirmed by neutron diffraction (ND) and solid-state NMR (ssNMR). In addition, Rietveld refinements yielded the final stoichiometry of our materials. A combination of ND, ssNMR and electrochemical tests for oxygen reduction (ORR) activity give a positive outlook on the use of HLMOs as electrocatalysts in PEMFCs. In general, we have found that electrocatalytic activity increases with protonation. In addition, there are strong suggestions that formation of high-spin Mn^{3+} centres is aided by proton insertion. We hypothesize that inserted protons modify the local magnetic field experienced by Mn centres allowing the formation of its high-spin electronic structure, and that the resulting electrocatalytic activity is a synergistic effect between H^+ and high-spin Mn^{3+} ions as active sites. Furthermore, we report, to the best of our knowledge, characteristic proton resonances in spinel HLMOs for the first time. These results open the way to a new class of low-cost, alternative electrocatalysts for PEMFC applications.

4.1. Introduction

Proton-exchange membrane fuel cells (PEMFCs) commercial use has been hampered due to their still high costs. The use of precious metals such as platinum or ruthenium as electrocatalysts in both, Hydrogen Oxidation and Oxygen Reduction reactions (HOR and ORR, respectively) is one of the main downsides of these devices. This is why research in the field focuses a lot of attention in the search of ways to reduce the loading of precious metal catalysts or into finding alternative materials [1–3]. Recently, transition metal oxides (TMOs) have attracted attention due to their availability and low cost in many applications, e.g. semiconductors, (electro-)catalysis, energy storage. They are found in several natural catalytic cycles and the spread of their applications is mainly due to the various oxidation states they can take, thus giving them a variety of chemical properties that ultimately aid electron transfer where necessary [4–7].

In this regard, manganese oxides have been extensively studied as catalysts in many different applications, e.g. in the conversion of CO, NO_x, SO_x and other volatile organic compounds, decomposition of ozone and hydrogen peroxides, organic reduction and oxidation, removal of bacterial pathogens, epoxidation of olefins, photo-/electrochromics and oxygen evolution and reduction reactions (OER and ORR) [5–12]. In fact, different manganese oxides, e.g. MnO, MnO₂, Mn₃O₄, MnOOH, Mn₂O₃ and Mn₅O₈, have been shown to be highly active in alkaline conditions [10, 11, 13–15]. However, despite their potential as catalysts to ORR and OER in alkaline and neutral media in e.g. metal-air batteries [16–20], alkaline fuel cells [15, 17, 20], microbial fuel cells [16, 20] and electrolyzers [15, 21, 22], research on manganese oxides as catalysts in PEMFCs has been rather limited.

Catalysis in alkaline media often suggests that active materials have in common the fact that they allow reversible proton insertion, and in that regard several manganese oxides have been studied, e.g. Mn₂O₃, Mn₃O₄ and MnO₂ [7, 9, 11]. In particular, manganese oxides with cubic crystal structures have been shown as promising alternatives to ORR in alkaline conditions [4, 6, 7, 10, 23–25]. Cubic structures such as spinel with formula AMn₂O₄ have been shown to be more catalytically active than their tetragonal counterparts as they have better affinity towards oxygen adsorption as well as higher density of active sites [4, 23]. In this regard, the ratio of Mn⁴⁺/Mn³⁺ ions has been found to be vital for the four-electron pathway of ORR where higher catalytic activity has been attributed to larger amounts of Mn³⁺ species. In addition, Jahn-Teller distortion is a well-known phenomenon in manganese oxides, where the presence of one extra electron results in stretching of the y-axis in MnO₆ octahedra. This extra unpaired electron has been linked to higher catalytic activity because of its ease of transfer [5, 15, 26, 27].

A commonly used spinel type manganese oxide in energy storage is cubic LiMn₂O₄ (LMO). In this crystal Mn exists as both Mn³⁺ and Mn⁴⁺ and has an average oxidation state (OS) of 3.5+. These spinel-types are commonly used cathodes in Li-ion batteries, but have been shown to be selective absorbents [28–30], useful catalysts to the oxidation of methane and butane as well as good electrocatalysts for water oxidation in photocatalytic systems [31, 32]. Additionally, LMO has been found to increase proton conductivity of proton-conducting membranes (PEM) when used as

a filler [30].

One interesting characteristic of spinel LMOs is the possibility of ion-exchange by chemical de-lithiation in acidic media. Much like electrochemical Li extraction in a Li-ion battery cathode, Li is removed from the crystal lattice while preserving its structure, however, in this case protons are simultaneously inserted by exchange with the acid [33–37]. Therefore, this is a two-step process with lithium extraction as the result of a disproportionation reaction where Mn^{3+} turns into Mn^{2+} and Mn^{4+} (as proposed by Hunter [38]) and a reaction where Li^+ and H^+ ions are exchanged [34, 35]. The result is a spinel crystal with overall stoichiometry $\text{H}_2\text{Li}_{1-x}\text{Mn}_2\text{O}_4$ (HLMO). This proton-exchanged LMO has been shown to improve catalytic activity in methane and n-butane oxidation [31]. In addition, it has been shown that protons can be thermally desorbed as H_2 gas from HLMO to form a stable spinel phase up to 200 °C [31].

The combination of these properties, e.g. tuneable $\text{Mn}^{4+}/\text{Mn}^{3+}$ ratio, Li^+/H^+ ion-exchange in acidic media, H^+ recombination into H_2 , and their ability to act as (electro-)catalysts together with their availability and low cost, make spinel HLMOs an interesting alternative material as electrocatalyst for PEMFCs. The ionic substitution in an LMO structure induces local structural and electronic perturbations, which can affect lithium and proton dynamics in the lattice due to changes in the local magnetic fields experienced by the active sites. Thus, we hypothesize that from the range of chemical compositions that can be obtained, a range of chemical and physical properties that have an effect on electrochemical performance can also be obtained.

In catalysis, unpaired electron density transfer or induction to ligand orbitals is information of interest as understanding electronic spin states in a metal centre is key to controlling them and therefore reaction mechanisms [39]. Changes in local structure, structure of active sites and electron configuration are valuable molecular information that can aid the rational improvement of heterogeneous (electro-)catalysts through structure-activity relationships [39–41]. Magnetic resonance spectroscopic techniques such as NMR or EPR provide useful information in this regard as chemical shifts (δ) and scalar J couplings provide enough information to resolve complex structures. Nevertheless, when dealing with solid-state systems obtaining this information becomes more difficult because of the presence of large anisotropic interactions like dipolar couplings and chemical shift anisotropies, which lead to a significant broadening of the signals. In solid-state NMR (ssNMR), magic angle spinning (MAS) has been used to average the anisotropic broadening down to zero so that spectra have narrower lines resembling more closely NMR in liquid media [41, 42]. In heterogeneous (electro-)catalysis transition metals are commonly used due to the valency versatility discussed earlier, nevertheless, this makes them paramagnetic in many instances. In techniques such as (ss-)NMR, the use of paramagnetic nuclei complicates spectra interpretation further. NMR on paramagnetic environments, those with unpaired electron spins, has long been considered inconvenient due to signals so wide that useful information was hard to obtain [39, 40]. However, the field of paramagnetic NMR has widely expanded in the last few years as paramagnetic centres are common in many different applications,

e.g. organometallic complexes, solid battery electrode materials, metalloproteins, or pharmaceutical formulations, where characterization of structural and electronic properties is essential to understanding the system [40]. An important property of paramagnetic systems is that a hyperfine interaction between unpaired electrons and the observed nucleus exists. This causes large paramagnetic shifts, shift anisotropy (SA) and large broadening due to bulk magnetic susceptibility effects [40]. As a consequence, the use of fast MAS, low magnetic fields and nuclei with low gyromagnetic ratios has been key to recent developments in the area of electrode materials for batteries, where paramagnetic NMR can be used to determine the metal oxidation state, local environment as well as nuclei dynamics within a structure [39]. In addition, the possibility to assess hyperfine shifts in paramagnetic materials can help explain structure-activity relationships [41].

In this work we present a study of protonated spinel LiMn_2O_4 (HLMOs) that we have prepared by chemical de-lithiation through titration with an acid. We have varied the amount of acid added in order to obtain HLMOs with various compositions in the form of $\text{H}_z\text{Li}_{1-x}\text{Mn}_2\text{O}_4$. We aim to find out whether protonation of a spinel LMO can improve their electrocatalytic activity to ORR and if so, how are the crystal structure and electronic configuration of Mn centres related to it. We have used several techniques to resolve the structure of the resulting materials and gain some fundamental insight on the structure-activity relationships. For this, we use a combination of Neutron Diffraction (ND) and solid-state NMR to characterize proton insertion in cubic spinel HLMOs and get information about the electronic environment of Mn centres. In addition, we use electrochemical techniques to assess HLMOs activity in acidic electrolyte. The combination of these techniques provides unique information since neutrons are more sensitive to light elements than X-rays, thus being an appropriate probe for protons in a structure. We have corroborated proton insertion and resolved stoichiometry of our samples as a result from Rietveld refinement of our ND data. Furthermore, proton/deuteron exchange was done in our samples prior to ssNMR measurements as deuterium's lower gyromagnetic ratio offers better resolution and narrower lines which aids in spectral interpretation.

In short, we report a protonated spinel LMO (HLMO) in various compositions, where an increasing amount of protons is related to a higher concentration of Mn^{3+} centres which is, in turn, related to improved electrocatalytic activity towards ORR. From our results we hypothesize that higher amounts of high-spin Mn^{3+} exist as a result of protonation and that improved electrocatalytic activity is a result of a synergistic effect between H^+ and Mn^{3+} ions. Furthermore, and to the best of our knowledge, we report on the signature ^2H resonances of crystal protons in a spinel structure.

4.2. Experimental

4.2.1. Synthesis of $\text{Li}_{1+\delta}\text{Mn}_{2-\delta}\text{O}_4$ (LMO δ)

Three different spinel types with the form $\text{Li}_{1+\delta}\text{Mn}_{2-\delta}\text{O}_4$ were prepared by a solid state reaction as detailed in [43]. Shortly, $\text{LiOH}\cdot\text{H}_2\text{O}$ (Merck) and $\text{Mn}(\text{CH}_3\text{COO})_2\cdot 4\text{H}_2\text{O}$ (Fluka) were mixed in an appropriate molar ratio of Li:Mn so as to obtain spinel types

$\text{Li}_1\text{Mn}_2\text{O}_4$ (LMOd0), $\text{Li}_{1.1}\text{Mn}_{1.9}\text{O}_4$ (LMOd01) and $\text{Li}_{1.3}\text{Mn}_{1.7}\text{O}_4$ (LMOd03). The solid reactants dissolve in their own crystal water when heated to 100 °C under constant stirring. The resulting slurries were dried up at 110 °C in an oven for 5 h and subjected to two calcination steps afterwards. In the first step, all samples were calcinated at 500 °C for 5 h. In the second step, the samples were calcinated for 10 h at different temperatures depending on the δ value, i.e. 700 °C, 600 °C and 500 °C for $\delta = 0, 0.1$ and 0.3 , respectively. All samples were ground with mortar and pestle after each calcination step, while the final powders were ball-milled at 750 rpm for 30 min in 2 cycles of 15 min with opposing directions. In table 4.1, an overview of the starting materials is shown.

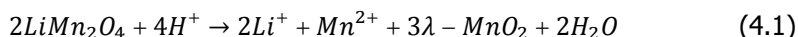
Table 4.1: Starting materials.

δ value	Stoichiometry	Short name
0	$\text{Li}_1\text{Mn}_2\text{O}_4$	LMOd0
0.1	$\text{Li}_{1.1}\text{Mn}_{1.9}\text{O}_4$	LMOd01
0.3	$\text{Li}_{1.3}\text{Mn}_{1.7}\text{O}_4$	LMOd03

4

4.2.2. De-lithiation/Protonation

All spinel types were chemically delithiated by two different processes. Initially, the 3 samples were leached in an acid solution in order to obtain reference samples of very low Li content, yielding $\text{H}_2\text{Li}_{1-x+\delta}\text{Mn}_{2-\delta}\text{O}_4$ (HLMO-I) spinel types. Leaching was done by mixing 4 g LMOd in 75 ml 5% HCl for 24 h under constant stirring at room temperature. The amount of solution was chosen to be at least twice the stoichiometric protons necessary to achieve complete de-lithiation following equation 5.1:



The resulting samples were vacuum filtered and washed several times with demineralized water and finally dried in a vacuum oven at different temperatures for at least 24 h. In order to study spinel phase stability at higher temperatures, as would be required in PEMFC, different drying temperatures were studied, namely 55 °C, 90 °C, 150 °C and 190 °C. In table 4.2, an overview of the reference samples used for temperature studies.

Table 4.2: Reference samples used for temperature studies.

Starting materials	T drying, °C	Short names
LMOd0	55, 90, 150, 190	LMOd0-55, LMOd0-90, LMOd0-150, LMOd0-190
LMOd01	55, 90, 150, 190	LMOd01-55, LMOd01-90, LMOd01-150, LMOd01-190
LMOd03	55, 90, 150, 190	LMOd03-55, LMOd03-90, LMOd03-150, LMOd03-190

On a second stage, the initial LMOd samples were titrated with H_2SO_4 1 M with different volumes of acid in order to obtain HLMOs with varying compositions for each δ value. The titrations were done using a Metrohm DMS Titrino 716 titrator.

The samples were prepared by mixing 4 g of each LMOd with 75 ml demineralized water followed by titration under constant stirring. The titration rate was 0.04 ml \cdot min⁻¹ and the amounts of acid added were 1.4 ml, 12 ml and 18 ml for LMOd0 and 6 ml and 18 ml for LMOd01 and LMOd03. The added acid volumes were chosen from a calibration curve so that spinels in different phases and compositions would result. The pH of the solution was monitored during titration vs. an Ag/AgCl (3 M KCl) electrode. All samples were vacuum filtered and washed several times with demineralized water and finally dried in a vacuum oven at 55 °C for at least 24 h. Table 4.3 shows a summary of nomenclature used for these samples based on the Li content found from ICP measurements.

Table 4.3: Details of de-lithiated samples from titration and immersion and nomenclature used.

δ value	Sample	V acid, ml	Li content	Short name
0	HLMOd0 1	1.4	0.99	HLMOd0-099
	HLMOd0 2	12	0.58	HLMOd0-058
	HLMOd0 3	18	0.29	HLMOd0-029
	HLMOd0 4 ¹	NA	0.13	HLMOd0-013L
0.1	HLMOd01 1	12	0.87	HLMOd01-087
	HLMOd01 2	18	0.35	HLMOd01-035
0.3	HLMOd03 1	12	0.98	HLMOd03-098
	HLMOd03 2	18	0.32	HLMOd03-032

4.2.3. Deuteration

A sample of HLMOd0-029 was washed several times with D₂O (99%, Sigma Aldrich). In short, 100 mg were sonicated in 5 mL of D₂O for 30 min and centrifuged 3 times at 7000 rpm. The resulting slurry was dried at 90 °C in a vacuum oven.

Alternatively, fresh samples were prepared where ion exchange of D/Li⁺ was done instead of H⁺/Li⁺ by leaching 500 mg of LMOd in 5 mL of D₂SO₄ 1 M for 24 h. All δ values were exchanged with deuterons so as to obtain samples DLMOd0-90, DLMOd01-90 and DLMOd03-90, respectively. The resulting slurries were vacuum filtered and centrifuged several times with heavy water at 7000 rpm and finally dried in a vacuum oven at 90 °C for at least 24 h.

Finally, a set of titrated LMOs from LMOd0 was also prepared by titration with D₂SO₄ 1 M (prepared by diluting D₂SO₄ 99%, Sigma Aldrich in D₂O) under Argon. Two titration points were chosen as follows: for 2 g LMOd0 in 35 ml of D₂O, 6 and 9 mL of heavy acid were added at a rate 0.02 ml/min. The samples were centrifuged with 5 mL of heavy water 3 times. After each centrifuge cycle, the remaining water was collected, fresh heavy water was added and sonicated for 5 min before centrifuging again. In table 4.4, a summary of deuterated samples is shown.

¹Samples that were leached in solution as described in the previous section.

Table 4.4: Deuterated samples.

δ value	Method	Short name
0	Leaching in solution	DLMOd0-007L
0	Titration	DLMOd0-040
0	Titration	DLMOd0-009
0	HLMOd0-029 washed with D_2O	DLMOd0-029-w

4.2.4. XRD, SEM and ICP measurements

The samples were analysed by XRD with a Bruker D8 ADVANCE diffractometer (Co $K\alpha$, $\lambda = 0.1789$ nm) and the SEM micrographs were obtained using a JEOL JSM-6010 LA with a standard beam potential of 5 kV. Lithium and manganese content were analysed by ICP-OES using a Perkin Elmer Optima 5300DV instrument.

4.2.5. Neutron Diffraction

Subtle changes in structure and composition are expected in the de-lithiated spinel types as Li^+ ions are extracted and H^+ are inserted. Neutrons are more sensitive to light elements, such as H, in comparison to X-rays. Thus, as hydrogen coherent cross-section is significantly different (negative) from that of O and Mn (positive), neutron diffraction was used in order to verify proton insertion in the structures and quantify their composition. Neutron experiments were performed in the PEARL neutron powder diffractometer at the research reactor of Delft University of Technology, using the (533) reflection of the germanium monochromator (1.667 Å). A whole set of samples was measured at room temperature, i.e. HLMOd0 series (HLMOD0-099, HLMOd0-058, HLMOd0-029 and HLMOd0-013L) in order to study the progression of proton insertion with de-lithiation. Furthermore, final states of titrated samples with different δ values were also measured, i.e. HLMOd0-029, HLMOd01-035 and HLMOd03-032. The de-lithiated sample from $\delta=0.1$, HLMOd01-035, was also measured at low temperature, i.e. $T = 165$ K. Rietveld refinement fittings were done using GSAS [44, 45]. Atomic and lattice parameters were fit together with line broadening parameters (particle size and strain) as well as the background of the measurements. All refinements resulted in residuals $R_{wp} < 10\%$. In order to determine the proton positions, the differences between observed and calculated structure factor were obtained. Fourier density maps were obtained from the structure factors for the most de-lithiated sample, i.e. HLMOd0-013L. The H positions found from this calculation were used as input for Rietveld refinement upon addition of an H atom to the crystal lattice. The resulting refinement improved by 1-2%. All drawings of crystals and maps were done using free software VESTA [46].

4.2.6. Solid-state NMR

Solid-state NMR measurements were performed using a Bruker Ascend wide-bore 500 MHz (11.7 T) magnet equipped with a NEO console. Two channel 3.2 and 1.9 mm probeheads from Bruker were used for the measurements. The operating frequencies for ^6Li , ^1H and ^2H were 73.60 MHz, 500.13 MHz and 76.773 MHz re-

spectively, and all measurements were performed within a spinning speed range of 20 - 38 kHz and $\pi/2$ pulse lengths of 4.5 μs , 2.5 μs and 3.3 μs were determined for ^6Li , ^1H and ^2H , respectively. The chemical shifts of ^6Li spectra were referenced with respect to a 0.1 M LiCl solution, and those of ^1H and ^2H spectra against H_2O and D_2O , respectively. Based on the spin-lattice (T_1) relaxation time, recycle delays of 0.2 s were used, collecting between 128 and 11,264 scans for each sample. A spin-echo pulse sequence ($90^\circ - \tau - 180^\circ - \tau - \text{aq}$, where τ is an integer multiple of the rotor period) was used to collect data for ^6Li and ^2H nuclei, while a single pulse was used for ^1H measurements (see appendix 4.A).

4.2.7. Electrochemical tests

The HLMOs were tested in a three-electrode electrochemical cell using the rotating disk electrode technique (RDE) with a 5 mm glassy carbon disk (PINE Instruments) and an Autolab potentiostat. The working electrode was prepared by coating the glassy carbon electrode (0.196 cm²) with an ink of the active material. The ink consisted of 4 mg HLMO, 2 mg Vulcan XC-72R and 4.56 μL Nafion™ (solution at 5 wt.%) dispersed in 12 mL IPA by sonication for 30 minutes. Finally, a 13 μL aliquot was deposited onto the glassy carbon and left to dry at room temperature inside a fume hood. A Pt wire was used as counter electrode and all measurements were taken against a RHE electrode in 0.1 M HClO_4 electrolyte. The electrolyte was purged with either argon or oxygen for 30 min prior to any experiment. Cyclic voltammetry (CV) measurements were recorded at a scan rate of 50 mV $\cdot\text{s}^{-1}$ and linear sweep voltammograms (LSV) were taken in the cathodic direction at 5 mV $\cdot\text{s}^{-1}$ at 1600 rpm and materials were compared based on ORR onset potential.

4.3. Results

The crystal structure of the $\text{Li}_{1+\delta}\text{Mn}_{2-\delta}\text{O}_4$ synthesized was verified by XRD as a spinel type, whereas expected stoichiometry was verified by ICP (See Appendix 4.B).

4.3.1. Leaching in acid solution and temperature stability of crystal structure

Reaction rates increase with temperature, which is why it is desirable to operate fuel cells at temperatures that generate the fastest output charge without damaging the materials and components. Currently, the limiting material is the polymer membrane (Nafion®) that cannot withhold temperatures higher than 100 °C. As a consequence, PEMFCs operate at mild temperatures, between 80 – 90 °C, which makes it necessary that all materials be stable at this temperature. We confirmed by XRD (see Appendix 4.B) that all leached materials, i.e. different δ values in an HCl solution (5%), retain the spinel crystal structure. To study structure stability at higher temperatures, all resulting slurries were dried in a vacuum oven at temperatures from 55 to 190 °C for 24 h, including a leached commercial sub-micron LMO as reference (HLMO-com). In general, all samples retain the spinel type crystal structure up to 150 °C, whereas at 190 °C we see a significant loss of crystallinity

(See Appendix 4.C). Lithium content of leached samples as obtained from ICP measurements are given in table 4.3.

4.3.2. Controlled ion-exchange (Li^+/H^+) by titration

We prepared *spinel*s of different compositions by titration with different amounts of acid. Titration curves of all δ values are shown in Appendix 4.D and a summary of all prepared samples is shown in 4.3. For simplicity, sample short names will be used from here on.

X-ray diffractograms for all de-lithiated samples at all δ values are shown in figure 4.1. Li extraction is associated with the oxidation process of Mn as Mn^{3+} undergoes a disproportionation reaction to give Mn^{2+}aq and Mn^{4+} , according to equation 5.1.

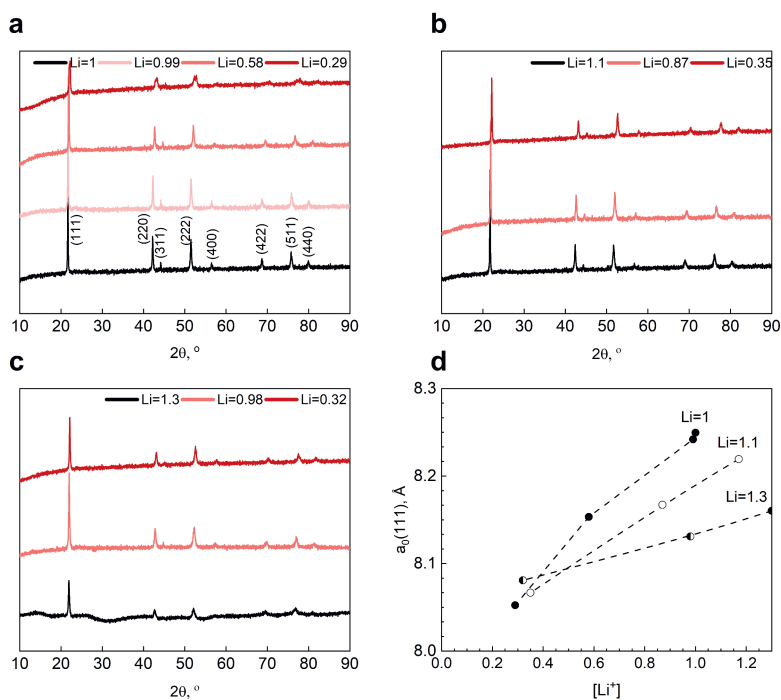


Figure 4.1: X-ray diffractograms of de-lithiated samples (a) HLMOd0 ($\delta = 0$); (b) HLMOd01 ($\delta = 0.1$); (c) HLMOd03 ($\delta = 0.3$); (d) Lattice parameter, a_0 calculated from reflection (111).

Diffractograms on leached samples confirm that the spinel structure is retained as Li^+ extraction proceeds. Extraction of Li^+ ions from 8a sites is known to induce a decrease in the a lattice parameter [47], which can be confirmed by a shift in reflections to higher 2θ degrees. Figure 4.1b shows the change in the a lattice parameter with Li composition as calculated from the shift in reflection (111). In general, Li

extraction seems to occur more readily at lower δ values, i.e. when there is no Li^+ substitution in 16d sites. Furthermore, as Li^+ content decreases and H^+ insertion is presumably increasing, we see a loss of crystallinity as indicated by peak broadening, most visible in (220), (222) and (511) reflections, along with a decrease in intensity and a shift to lower interplanar distances, d , (or higher 2θ) meaning a contraction of the unit cell (2.7%). Bach et al [47] studied electrochemical protonation of LMOs and also observed peak broadening as concentration of protons increased in the unit cell. In our case, the most notable change is broadening of the aforementioned reflections, as well as peak splitting in reflections (220) and (222). This can be due to inhomogeneous de-lithiation resulting in different spinel types with slightly different compositions and lattice parameters. At the same time, this effect is more prominent as more Li^+ is extracted and more protons presumably inserted. According to our results and those of Bach et al., peak splitting has been observed when protons were inserted and could be used as an indirect measure of proton insertion. Nevertheless, peak splitting has also been observed for LiMn_2O_4 at low lithium content in electrochemical cells, due to two coexisting spinel phases with different lattice parameters [48–50].

In Appendix 4.E, SEM micrographs of powders before and after de-lithiation by titration for LMOd0 are shown. The most notable difference is an apparent change in particle size after leaching and apparent increased porosity, which ultimately may increase catalytic activity.

4.3.3. Structure and composition analysis by neutron diffraction

As neutrons are more sensitive to light elements such as hydrogen, neutron diffraction was used to verify proton insertion in the crystal lattice. The $\delta=0$ series of de-lithiated samples, i.e. from stoichiometric LMO, was measured at room temperature as well as the most de-lithiated titration points of starting materials with $\delta = 0.1$ and 0.3 . Appendix 4.F shows the resulting diffractograms of series HLMOd0, HLMOd0-099, HLMOd0-58, HLMOd0-029 and HLMOd0-013L. Results from Rietveld refinement of diffraction patterns are shown in figure 4.2.

Initial fittings with a spinel LMO CIF file were done assuming no protons or Li atoms were present in the lattice, thus only the Mn-O framework was considered. Results are shown in figure 4.2a, where an $R_{wp} = 0.08$ was obtained. In order to find missing elements, scattering length density differences were calculated from the observed versus calculated intensities using GSAS software. The resulting Fourier maps are shown in figures 4.2c and 4.2d. Scattering length density is missing at the tetrahedral positions where Li_{8a} is expected. However, there is also density missing in positions surrounding the centre of the tetrahedra (8a position) and oriented towards the oxygen corners (32e positions). In total there are 12 distinguishable spots around each 8a position whose coordinates were introduced in the next fitting cycle when inserting H atoms into the model structure. The new fitting converged to $R_{wp} = 0.07$ (figure 4.2b) with the new coordinates corresponding to 96g positions. In addition, the resulting -O-H bond length is $\sim 1.2 \text{ \AA}$ which is in good agreement with values found in literature of $\sim 1.1 \text{ \AA}$, [51]. R_{wp} values < 0.1

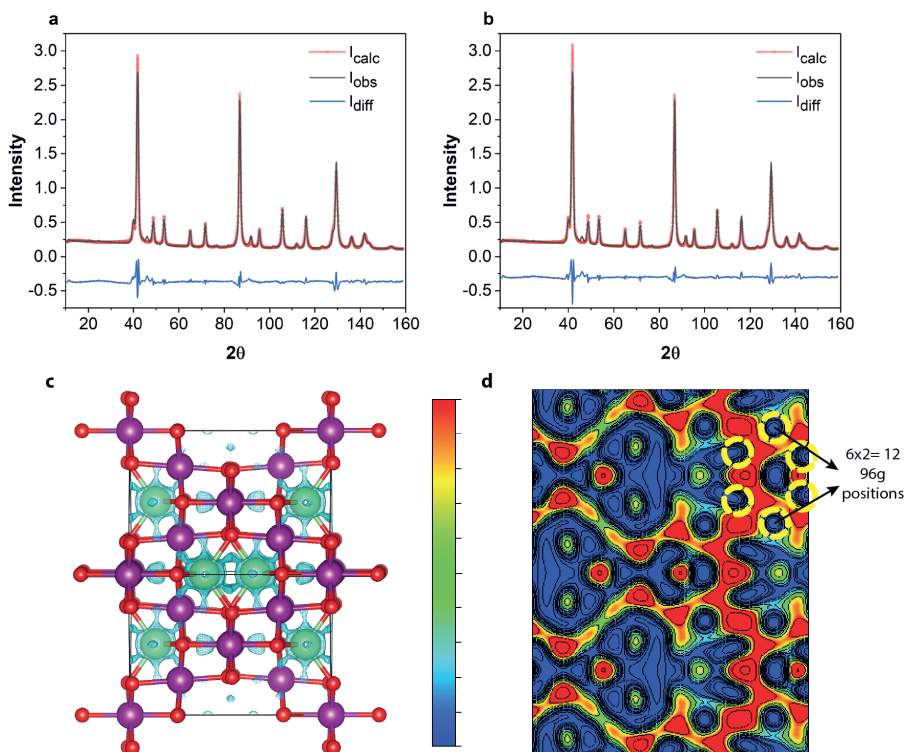


Figure 4.2: Neutron diffraction fittings (a) before including Li and H atoms, and (b) after including them. (c) Fourier map of calculated missing intensity in the unit cell. (d) 2D Fourier map from a slice taken at -1.6 .

are considered good fits, however, it is noteworthy that our refinements have been performed with as few variables as possible. From ND and XRD diffractograms we see that there is line broadening and peak splitting in some reflections (511) and (222) in XRD measurements) as ion-exchange progresses further. This is due to inhomogeneous de-lithiation which results in a distribution of crystallites with slightly different compositions. For simplicity, we have considered only one spinel phase which yields a good fit with a relatively low amount of variables. Indeed, when smaller amounts of Li are removed from the lattice, refinements result in lower R_{wp} values (i.e. $<5\%$).

The position where scattering density was missing around tetrahedral centres is known to be a preferential site for protons in spinel crystals [47, 51–55]. Therefore, these results confirm that protonation has taken place in the spinel structure and the structure is shown in figure 4.3. The resulting compositions of protonated spinel types are shown in table 4.5 and all raw data and refinements as well as a summary of all results can be found in Appendix 4.F.

Table 4.5: Final stoichiometry with H content of de-lithiated HLMOd0.

Sample	Stoichiometry
HLMOd0	LiMn_2O_4
HLMO-099	$(\text{H}_{0.02})\text{Li}_{0.99}\text{Mn}_2\text{O}_4$
HLMO-029	$(\text{H}_{0.36})\text{Li}_{0.29}\text{Mn}_2\text{O}_4$
HLMO-013L	$(\text{H}_{0.68})\text{Li}_{0.13}\text{Mn}_2\text{O}_4$

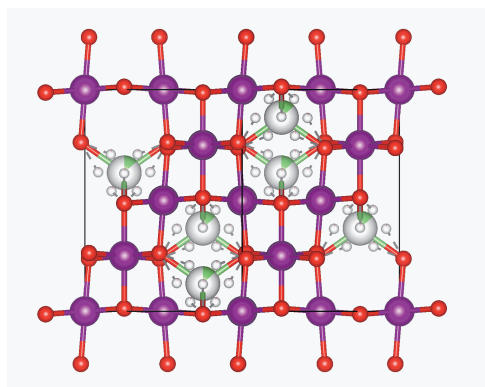


Figure 4.3: Final spinel HLMO crystal structure.

In general, we find that proton insertion is minimal at Li^+ content > 0.6 . Most of it occurs at Li^+ content < 0.3 with onset of the exponential trend below Li^+ content < 0.1 . Proton insertion as a function of Li^+ content follows equation 4.2 (see figure 4.4a and b). These results can also be correlated to the titration curves, where two plateaus can be observed (see Appendix 4.D). The first plateau, at $\text{pH} \sim 3 - 4$, coincides with low H^+ insertion but large amounts of Li^+ have been extracted ($\sim 40\%$). On the other hand, the second plateau, at $\text{pH} \sim 2 - 3$ coincides with H^+ insertion take-off.

$$[\text{H}^+] = -0.35405 \ln([\text{Li}^+] + 0.00963) \quad (4.2)$$

Furthermore, de-lithiation/protonation results in shortening of the lattice parameter of max. 2.0% by titration and 2.5% by leaching in solution. Furthermore, no strain was found to happen by either process (see Appendix 4.F). In general, leaching with an acid also results in reduced crystallite sizes as seen in figure 4.4c. There was a considerable decrease of $\sim 60\%$ resulting in crystals of ~ 10 nm when leaching with H_2SO_4 1 M. Contrastingly, there was only $\sim 18\%$ reduction in crystallite size to ~ 21 nm when leaching with HCl 5 % for 24 h even though larger amounts of Li^+ were extracted with this method. Sulfuric acid is a stronger acid, thus attacking the surface of the crystals more aggressively which can also be seen in the SEM micrographs in Appendix 4.E where smaller particles and apparent higher porosity are visible. Even though sulfuric acid is more aggressive, larger surface area is a desired property in catalytic materials.

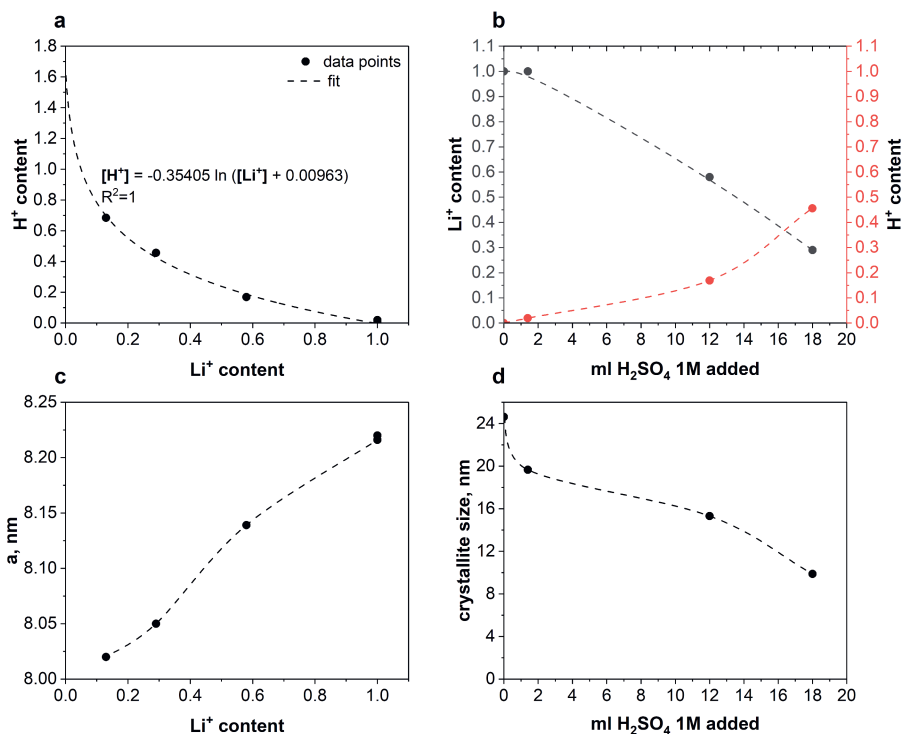


Figure 4.4: ND analysis. (a) H⁺ content vs. Li⁺ content; (b) Li⁺ and H⁺ content vs. acid added; (c) Lattice parameter, *a* vs. Li⁺ content; and, (d) Average crystallite size vs. acid added.

4.3.4. Chemical shift of protonated LMOs

De-lithiation/proton insertion was monitored with solid state NMR. Figure 4.5 shows the results for ⁶Li spectra obtained with one pulse sequences as described in the Methods section. Centre bands are indicated with an inverted triangle, while sidebands are marked with a star. The main Li signal was found at ~520 ppm in standard LMO and it is associated with Li in 8a positions as the site with highest occupancy from ND refinements. This result is also in agreement with literature values for Li in 8a positions [56, 57].

However, there is a less intense resonance at ~600 ppm that seems to shift downfield and increase intensity with de-lithiation/protonation. This resonance has been attributed before to Li atoms in the 16c positions [57]. We observe that as ion exchange proceeds, the resonances of Li_{8a} and Li_{16c} shift downfield as a new resonance at ~790 ppm develops. This new resonance has been attributed in other studies to Li atoms in 16d positions [42]. The evolution of chemical shift with de-lithiation of each site is presented in figure 4.6. It is noteworthy that in sample HLMO-058 which corresponds to the transition region in the de-

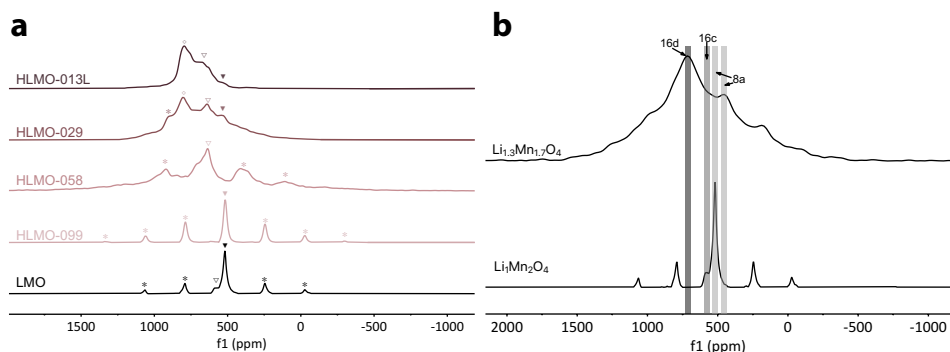


Figure 4.5: ^6Li solid-state NMR of (a) protonated samples (\blacktriangledown 8a, ∇ 16c, \diamond 16d) and (b) Comparison of $\text{Li}_1\text{Mn}_2\text{O}_4$ with Li in 8a position vs. $\text{Li}_{1.3}\text{Mn}_{1.7}\text{O}_4$ with 8a positions full and excess Li in 16d positions replacing Mn octahedral centres.

lithiation/protonation reaction only presents one resonance at the 16c position. Li_{8a} and Li_{16d} seem to be barely occupied in this region.

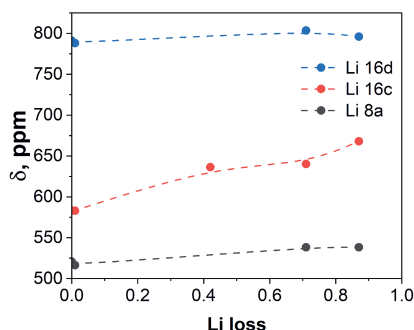


Figure 4.6: ^6Li solid-state NMR: Chemical Shift at each Wyckoff site vs. Li loss.

On the other hand, protonation was monitored during de-lithiation by ^2H NMR. Deuteron is chosen to probe proton insertion into our material because of spectroscopic advantages of using low gyromagnetic ratio nuclei to observe paramagnetic lattices [58]. Deuterated samples analogous to their protonated counter-parts were prepared following the same protocols but using 1 $M\text{D}_2\text{SO}_4$ instead. The final samples are shown in table 4.6.

Figure 4.7a shows a typical ^2H spectra taken with a Hahn-echo pulse sequence for sample DLMOd0-007L. In general, we observe a wide signal (~ 4000 ppm) in itself suggesting deuteron insertion. Proton spectra are typically ~ 40 kHz in a static measurement of a solid sample. This is due to strong dipolar coupling interactions

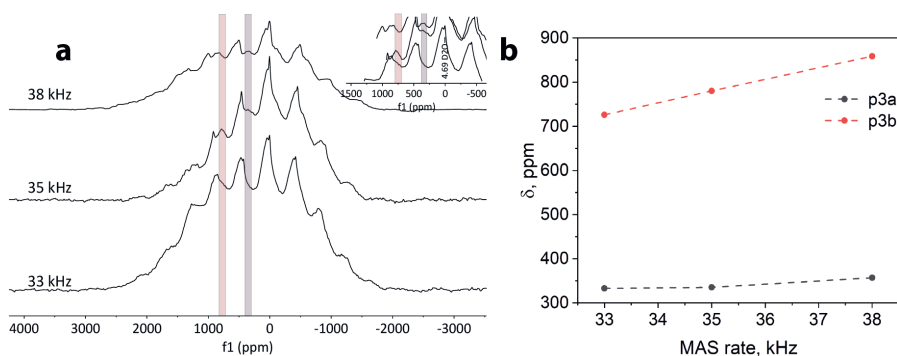
²Per 2 g starting LMO.

³Prepared in solution.

Table 4.6: Stoichiometry of deuterated samples.

Sample	V acid ² , ml	Li content	Short name
DLMOd0 1	6	0.404	DLMOd0-040
DLMOd0 2	9	0.089	DLMOd0-009
DLMOd0 3 ³	NA	0.077	DLMOd0-007L

resulting from ^1H spins [41]. Broad lines are worsened by the paramagnetic environment due to Mn centers creating a hyperfine interaction between its unpaired electrons and ^1H nuclei, which in turn creates large chemical shifts, shift anisotropy and large broadening due to bulk magnetic susceptibility [40]. Even though protons/deuterons in paramagnetic environments are hard to resolve, we were able to observe 3 different environments, e.g. 4.69 ppm, ~ 65 ppm and ~ 350 ppm (see Appendix 4.G). Deuterons in a diamagnetic environment are expected at higher fields, i.e. 4.69 ppm and ~ 65 ppm, that can be attributed to residual ^2H (from solution, washing, etc), i.e. non-lattice accumulation [58]. The resonance at 4.69 ppm has been assigned to adsorbed D_2O and all spectra were referenced against this value. The next resonance, i.e. ~ 65 ppm, has been assigned to chemisorbed -OD by a simple H/D exchange experiment (see Appendix 4.Gb). Finally, deuterons in a paramagnetic environment are indicative of lattice ^2H . Paramagnetic resonances are expected to have a large chemical shift towards lower fields mainly due to Fermi-contact interactions resulting from larger hyperfine coupling which is directly related to the magnetic susceptibility of the material (this will be detailed further in the next section). According to findings in similar materials, e.g. layered Li_2MnO_3 , where lattice protons/deuterons were found at a large chemical shift of ~ 290 - 380 ppm [58], we expect to find the lattice ^2H at a similarly large chemical shift .

Figure 4.7: ^2H solid-state NMR of DLMO-007L at different MAS rates.

Other than the low chemical shift resonances and their sidebands, we observe another resonance and its sideband at ~ 350 ppm and ~ 800 ppm (highlighted bands in figure 4.7a inset, referred to as p3a and p3b, respectively). To elucidate which of the two is the centre band, spectra at different MAS rates were recorded and

the chemical shift of those two resonances was compared. Figure 4.7b shows the chemical shift of these two resonances as a function of MAS rate. From this we have determined the centre band to be that at $\sim 341.6 \pm 10.9$ ppm as it is the resonance with the least variability –the resonance at lower field increases monotonically with MAS rate, thus it is a sideband.

Deuterium spectra for samples with different composition are shown in figure 4.8a. Based on the H^+ to Li^+ content correlation found in the previous section by neutron diffraction, we have estimated the proton/deuteron fraction in our deuterated samples (see equation 4.2). In figure 4.8b, the change of chemical shift with proton content is presented. In general, the more hydrogen bonding there is, the further downfield a resonance is found [59]. As Li atoms are removed from the lattice and replaced by H atoms, electron density is lost resulting in deshielded H nuclei whose resonance move further downfield as more bonds are created.

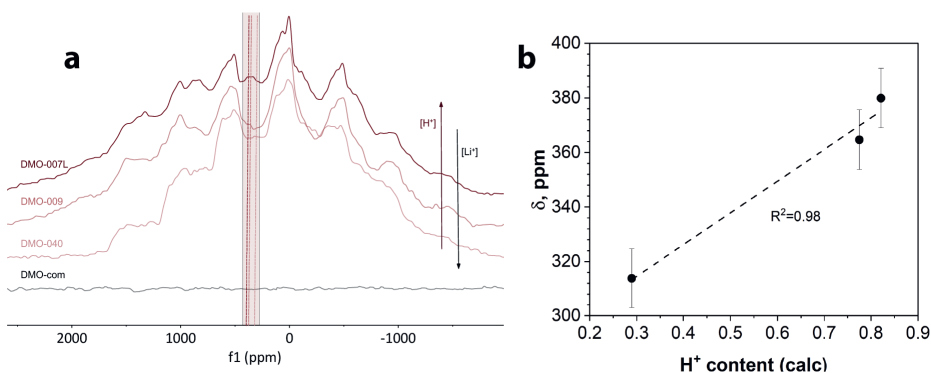


Figure 4.8: 2H solid-state NMR of samples with different compositions (left); and 2H chemical shift vs. H^+ fraction (right).

4.3.5. Electrochemical performance of HLMOs electrocatalysts for ORR in acidic media

Cyclic voltammograms of HLMOs with different proton content in acid media ($HClO_4$ 1 M) are shown in figure 4.9, left panel. In general, the more protons in the material, the higher the reduction current when cycled in oxygen-saturated electrolyte (red curves). Rotating-disk electrode measurements at a rotation speed of 1600 rpm in oxygen saturation were done in order to estimate the onset potential to oxygen reduction. In the bottom right panel of figure 4.9, the variation of onset potential, $V_{onset,ORR}$, with Li content is presented. Even though there are large overpotentials ($V_{ORR,ideal} = 1.23$ V), electrocatalytic activity to ORR increases with proton content, suggesting a synergistic effect between Mn centers and proton-aided charge transfer to oxygen reduction intermediates.

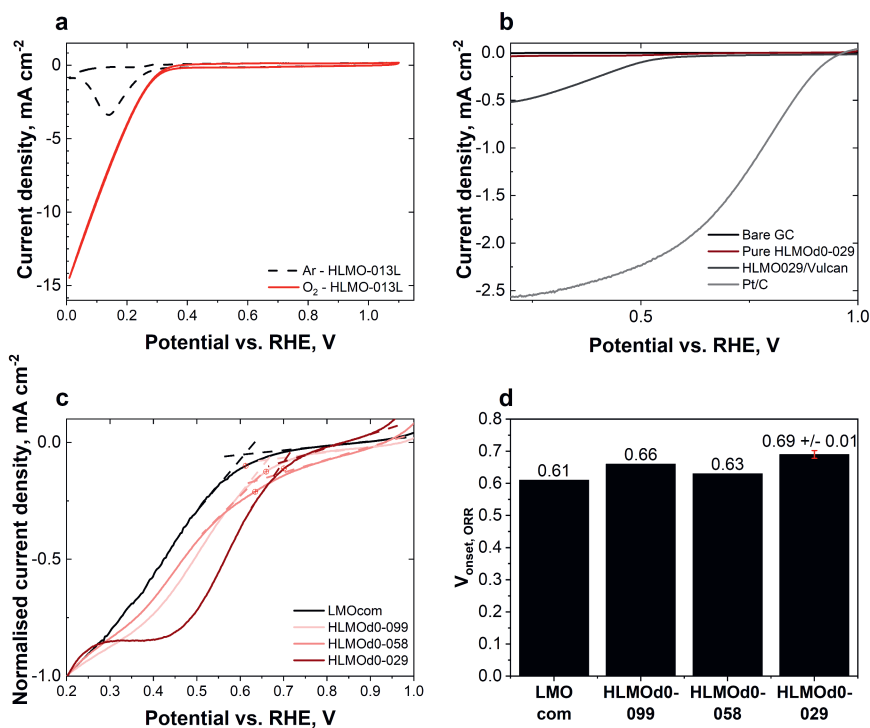
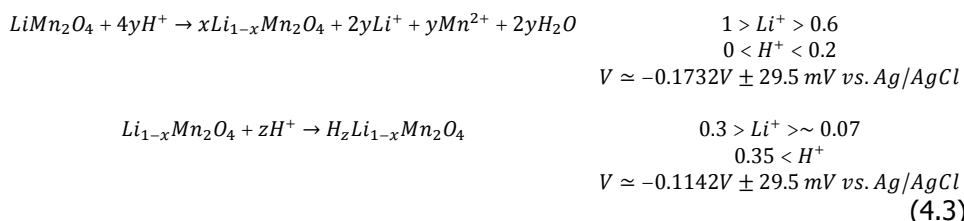


Figure 4.9: Electrochemistry results:(a) HLM0d0-013L electrode on GDL in Ar vs. O₂; (b) RDE HSVs of bare glassy carbon electrode vs. pure HLM0d0-029 vs. HLM0d0-029/Vulcan vs. JM Pt/C in O₂ saturated electrolyte @ 1600 rpm; (c) normalized HSVs of samples with different compositions in O₂ saturated electrolyte @ 1600 rpm; (d) ORR onset potential estimations.

4.4. Discussion

We have prepared a range of protonated spinel LMOs, referred to as HLMOs, with varying Li⁺ and H⁺ content. Lithium to proton ion-exchange was done by chemical leaching Li⁺ with an acid and the final composition, i.e. proton and lithium content, can be tuned by the amount of titrant added. Volume vs. pH (chemical potential) titration curves showed a 2-plateau curve suggesting ion-exchange occurs in two steps. In the first plateau (low potential vs. Ag/AgCl), the dominant process is Li extraction. This reaction is predominant down to Li⁺ content = ~0.6. There is a transition region between 0.6 > Li⁺ content > 0.3 where both, Li⁺ extraction and H⁺ insertion occurs at the same time, and finally a second plateau at higher potential where H⁺ insertion takes off (at Li⁺ < ~0.3). The reactions are shown in equations 4.3.



Leaching with acid also causes some morphology changes in the resulting powders such as smaller particle size and smaller crystals. Ultimately, this is a desired characteristic in (electro-)catalysts as activity is directly correlated to surface area. In general, ion exchange is linearly correlated to smaller crystallites and lattice parameter, a .

We have used a combination of neutron diffraction and solid-state NMR in order to characterize the proton insertion in spinel LMOs. Neutron diffraction measurements have confirmed the ion-exchange reaction and we have been able to locate structural protons in the spinel lattice at the 96g site (in Wyckoff notation). In this position, protons surround a tetrahedral 8a site and are oriented towards the corners of the tetrahedron where the oxygen atoms reside. Ion-exchange results in a linear decrease of the lattice parameter from 8.24 Å in LMO to 8.02 Å in HLMO-013L. Resulting compositions estimated by ND have shown that most of proton insertion occurs at pH < 3 where proton content starts to increase exponentially following equation 4.2. Furthermore, we did not observe any strain inflicted on the materials by treatment with acid, and the resulting O—H bond length was 1.1 Å, which is in agreement with values found in the literature [51] and measured by us in a different study (see Chapter 5). Furthermore, we have identified in proton/deuterium solid-state NMR three signature resonances in spinel (D)HLMOs. Two diamagnetic resonances that have been assigned to adsorbed water and chemisorbed -OH groups and an extra paramagnetic resonance at a large chemical shift. This resonance at ~341 ppm was assigned to structural protons in the spinel structure, i.e. protons in the 96g site. This large chemical shift is the result of the paramagnetic nature of LMO due to its unpaired electrons in Mn³⁺ and Mn⁴⁺ ions. An estimation of Mn average oxidation state (OS) can be done from the resulting compositions obtained by ND experiments. The resulting values are in agreement with those found for samples similar to HLMOD0-013 and HLMOD0-029 by X-ray absorption spectroscopy in a different work (see Chapter 5 and Appendix 4.H). It has been previously shown that Li_{8a} chemical shift increases linearly with increasing oxidation state below 3.7+ in spinel manganese oxides [56], which is in agreement with our results. However, on closer inspection of all our samples, Mn OS reaches a maximum and starts to decrease again as chemical shift keeps increasing (see figure 4.10). This phenomenon can be understood by considering the origin of chemical shift in paramagnetic materials. NMR spectra of paramagnetic materials are mainly dominated by two interactions: dipolar interactions and Fermi-contact. The first one related to the interaction between the nuclear and electronic moments, and the latter is a through-bond interaction related to the transfer of unpaired spin density from the

paramagnetic nucleus to the s orbitals of the Li atoms [40, 56]. In spinel manganese oxides Fermi-contact interactions are predominant in the resulting chemical shift. The isotropic part of this interaction can be written as $H_c = I_z A_s \langle S_z \rangle$, where A_s is the electron–nuclear hyperfine coupling constant and $\langle S_z \rangle$ is the thermally averaged value of the paramagnetic spin. A_s is a measure of the transferred spin density from Mn t_{2g} and e_g orbitals to the lithium s orbitals. On the other hand, $\langle S_z \rangle$ is proportional to χB_0 where χ is the magnetic susceptibility and B_0 the magnetic field [40, 42, 56]. In spinel LMOs the magnetic susceptibility, χ , decreases as oxidation state increases from 3.5+ to 4+. This can be understood by looking at the spin-only magnetic moments of both ions where $\mu_{SO, Mn^{4+}} = 3.873\mu_B < \mu_{SO, Mn^{3+}} = 4.899\mu_B$. The ratio between Mn⁴⁺/Mn³⁺ ions increases as oxidation state takes values closer to 4+ in which state less unpaired electrons exist. When the Mn⁴⁺/Mn³⁺ ratio increases, the average magnetic moment per atom, and thus the magnetic susceptibility, both decrease with the decrease of unpaired electron density. On the other hand, A_s is affected by Mn oxidation state through overlapping of the lithium s orbitals with Mn t_{2g} and e_g orbitals. In figure 4.4 we saw that the lattice parameter, a , decreases linearly with Li extraction and therefore with increasing Mn OS. As the bond lengths are shortened, the overlapping between Li and Mn s and d orbitals increases making A_s magnitude larger. Thus, there are two opposing effects that cause the change in Fermi-contact shift with Mn OS, namely the decrease of $\langle S_z \rangle$ due to lower magnetic susceptibility and the increase in A_s due to larger overlapping of Li s and Mn d orbitals. Thus, the magnitude and sign of the chemical shift is determined by A_s in this case as other studies have asserted before [56]. We have found that indeed Li chemical shift at all sites, i.e. 8a, 16c and 16d, increases with increasing Mn OS when Li content > 0.29. However, at lower Li content, i.e. 0.13, oxidation state decreases while chemical shift keeps increasing (except for Li 16d). This inflection in the trend suggests that A_s is no longer the determining factor of the chemical shift but that the magnetic susceptibility is playing a bigger role. If the oxidation states lowers, it follows that so does the hyperfine coupling, nevertheless, depending on which Li site, their resonance continues to shift to higher or lower values. As A_s continues to increase due to a lower lattice parameter even in samples with the smallest Li amount, it follows that the magnetic susceptibility is responsible for this change. In Li_{8a} and Li_{16d} resonances are shifting downfield meaning a higher magnetic susceptibility. This in turn means that amount of Mn³⁺ ions is increasing at Li content < 0.29. This inflection points correlates well with ND proton insertion take-off and the second plateau of the titration curve, strongly suggesting that the phenomenon happening in the second plateau is proton insertion accompanied by an increase in the concentration of Mn³⁺ ions.

On the other hand, Mn³⁺ ions can have either high- or low-spin states, eg. $3d t_{2g}^3 e_g^1$ or $3d t_{2g}^4 e_g^0$, respectively (see figure 4.11). The spin-only magnetic moment is related to the number of unpaired electrons (n) by $\sqrt{n(n+2)}$, thus $\mu_{SO} = 4.899\mu_B$ for Mn³⁺ high-spin and $\mu_{SO} = 2.828\mu_B$ for Mn³⁺ low-spin. In figure 4.10, Li_{8a} and Li_{16c} resonances shift further downfield even when Mn OS decreased. A_s influence keeps increasing as the lattice parameter for HLMOD0-013L is smaller resulting in

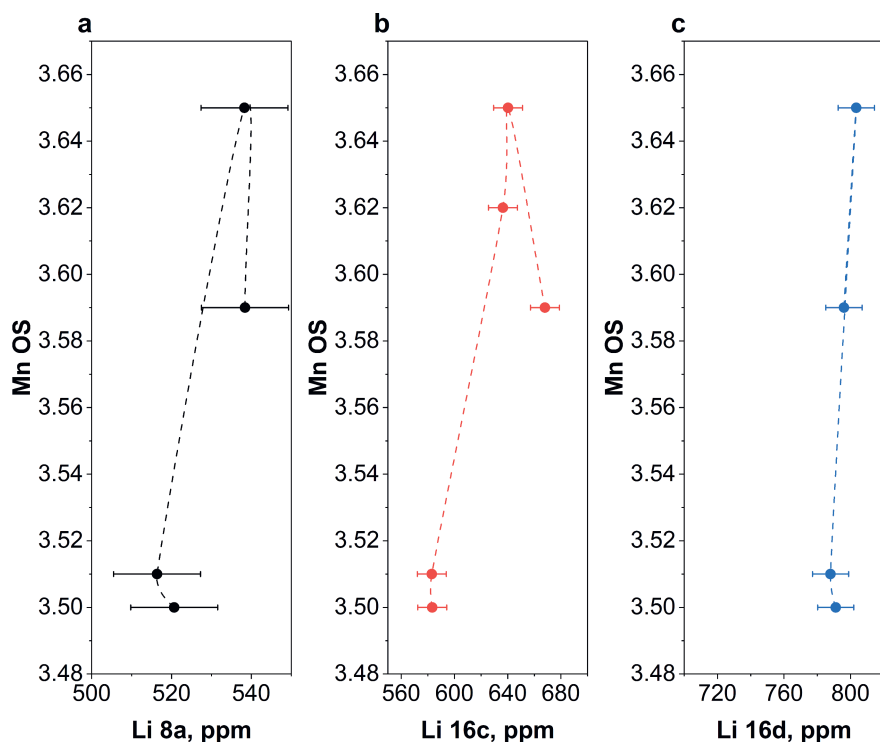


Figure 4.10: Mn OS change with ^6Li chemical shift: (a) Li_{8a} , (b) Li_{16c} , (c) Li_{16d} .

more overlapping of Li and Mn s and d orbitals, therefore this shift must be the result of an increase in the magnetic susceptibility, and thus the magnetic moment, of the neighbouring paramagnetic nucleus. This shift at these two specific sites suggests that Mn^{3+} high-spin exists in our samples and is mostly located around remaining Li atoms in the samples at the 8a positions and those that have migrated to the interstitial 16c sites. On the other hand, Li atoms that have migrated to vacant 16d sites do not seem to affect the spin state of the neighbouring Mn atoms as chemical shift decreases again with decreasing Mn OS.

Further insight can be gained by inspection of manganese average oxidation state against Li^+ and H^+ content for our samples as shown in figure 4.12. In general, oxidation state lowers as more protons are inserted thus decreasing the ratio of $\text{Mn}^{4+}/\text{Mn}^{3+}$ ions. As previously discussed, more Mn^{3+} ions in a high-spin state would create a larger ferri-contact shift, deshielding protons further. This suggests that proton insertion aids in the formation of high-spin Mn^{3+} centres neighbouring 96g sites. Proton/deuteron and lithium NMR results suggests that proton insertion together with Li extraction aid in the formation of more high-spin Mn^{3+} species. High-spin states of Mn^{3+} ions have been identified in previous studies as

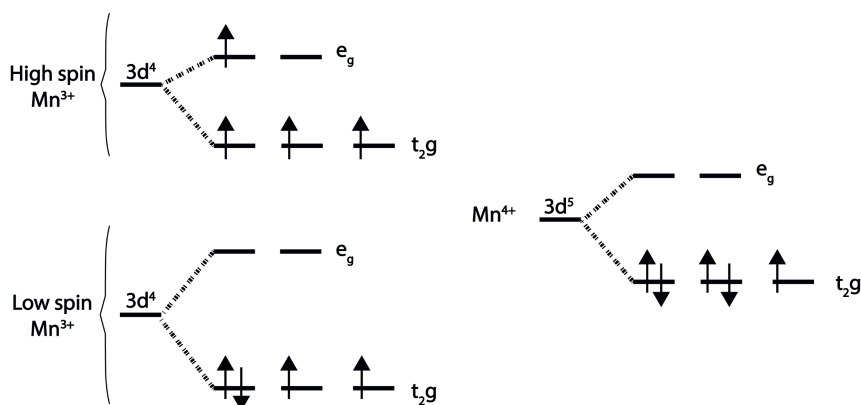


Figure 4.11: (left) Mn^{3+} high-spin (low splitting energy, Δ_o) and low-spin (high splitting energy, δE_o) electronic configuration, and (right) Mn^{4+} electronic configuration.

the catalytically active species owing to their loosely bound electron in the e_g orbital [26, 27, 60]. However, more research on the magnetic susceptibility of our samples is necessary in order to find out the actual spin-states but the present results give strong suggestions for the formation of high-spin states.

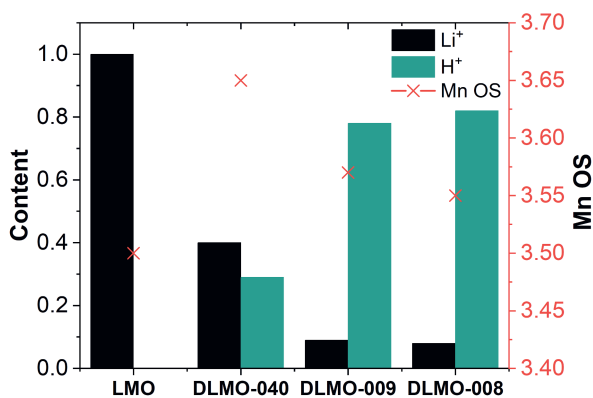


Figure 4.12: Li^+ and H^+ content (bars, left axis) and estimated Mn average oxidation state (right axis).

To support this hypothesis, electrochemistry results show that electrocatalytic activity to ORR, as evaluated by ORR onset potential, increases as larger amounts of protons are inserted in the spinel structure. In figure 4.13, it is interesting to notice that electrocatalytic activity also increases with the initial increase of Mn oxidation state up to Li^+ content = 0.29 and H^+ content = 0.4. After this point, Mn oxidation state starts to decrease again. In our most protonated sample that

was measured for catalytic activity, i.e. HLMO-029, oxidation state indicates that the ratio of $\text{Mn}^{3+}/\text{Mn}^{4+}$ favours Mn^{4+} species. A simple charge balance analysis from estimations of Mn oxidation states show that up to Li^+ content = 0.3, Mn oxidation state increases as mostly positive charges are removed from the crystal lattice, whereas below this point Mn oxidation state starts to decrease when positive charges accumulate from proton insertion. However, it is interesting to notice that stoichiometric, non-protonated LMO has the largest amount of Mn^{3+} ions (Mn oxidation state = 3.5+) but the lowest electrocatalytic activity with a loss of ~ 120 mV (vs. RHE) in comparison to HLMO-029 where Mn has an oxidation state of 3.66 ± 0.0016 . This finding suggests that even though a higher amount of Mn^{4+} exists in the sample, some of the existing Mn^{3+} ions have been modified by the local magnetic field to create high-spin states probably by the insertion of protons in the crystal. In short, there are strong suggestions that Mn oxidation state is not solely responsible for catalysis, but that charge transport is somehow aided by H^+ in the vicinity. Protons in the surface may act as active sites for intermediate species in ORR as well as H nuclei in the bulk may influence the local magnetic field experienced by Mn^{3+} centres via oxygen bonds. Thus, the electron density around Mn would decrease and allow a high-spin electronic configuration of Mn^{3+} species, i.e. $3d\ t_2g^3\ e_g^1$.

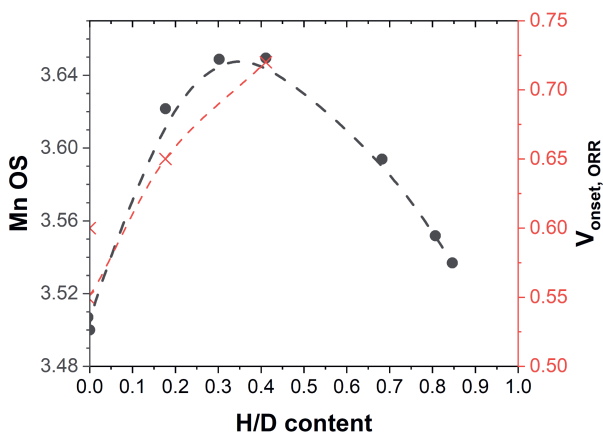


Figure 4.13: Mn OS and $V_{\text{onset, ORR}}$ vs H^+ content.

4.5. Conclusion

In general, we have prepared protonated spinel types from a Li-Mn-O system. Ion-exchange in LMOs happens in two stages as seen in potential (pH) vs. volume results from titration experiments. In a first stage, mostly Li^+ are removed from the lattice (up to Li^+ content = 0.6), and in a second stage mostly protons are inserted while there is strong evidence of high-spin Mn^{3+} centre formation (at Li content

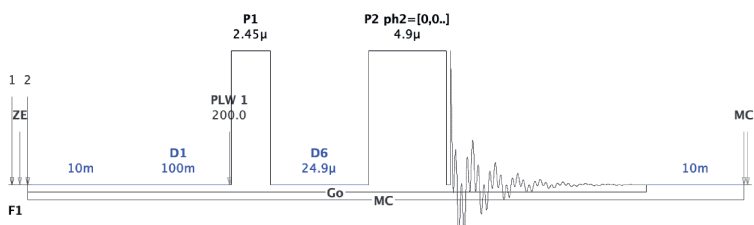
<0.3). These results agree with charge balance analysis done from estimations of Mn oxidation state. Up to Li^+ content = 0.3, Mn oxidation state increases as mostly positive charges are removed from the crystal lattice and Mn compensates by oxidising from (III) to (IV) valency. Below this point Mn oxidation state starts to decrease when positive charges accumulate from proton insertion. Proton insertion in the crystal lattice has been confirmed by neutron diffraction and solid-state NMR measurements where we have characterized the signature signal of crystal protons in a spinel LMO system. Furthermore, a correlation between Li^+ content and H^+ content from ND results has been presented and used to analyse solid-state NMR and electrochemistry results. We find that electrocatalytic activity as evaluated by onset potential to ORR, increases with increasing amounts of protons inserted as does the chemical shift. Larger chemical shifts are associated with increasing amounts of Mn^{3+} centres in either low- or high-spin configurations.

Even though it is hard to deconvolute NMR chemical shift into contributions from bond formation and orbital overlap or modification of the spin-state of paramagnetic centres with NMR experiments alone, a combination with electrochemistry tests has given some directions. In short, higher proton content results in higher onset potential to ORR, thus suggesting a synergistic effect between protons and active Mn centres. Furthermore, our results also suggest that formation of high-spin Mn^{3+} ions is aided by proton insertion and that the correlation between these two species and electrocatalytic activity is probably due to a modification of the local magnetic field experienced by neighbouring Mn centres by the inserted thus reducing the energy difference between the 3d split orbitals allowing one electron from the t_{2g} up to the e_g orbital where Mn^{3+} would be activated towards ORR, even though a higher ratio of $\text{Mn}^{4+}/\text{Mn}^{3+}$ exists at this point. Furthermore, we find that these centres exist near occupied 8a Li and interstitial Li 16c positions. In turn, this also suggests that small amounts of Li could be necessary in order to increase the concentration of high-spin Mn^{3+} ions. However, we would like to remark that more research is necessary in order to better understand spin configuration of Mn ions and its impact on electrocatalytic activity.

We want to finish by remarking that these results, even though in their early stages, open the possibility of new inexpensive materials that can be activated to ORR in acidic electrolyte, thus opening new opportunities in PEM fuel cell applications. Here a simple protonation procedure can improve electrocatalysis as measured by onset potential to ORR, however, whether activation is happening through charge redistribution creating high-spin Mn^{3+} or through the creation of new catalysis sites (H^+) is still unclear.

4.A. Hahn-echo pulse program for ^2H measurements

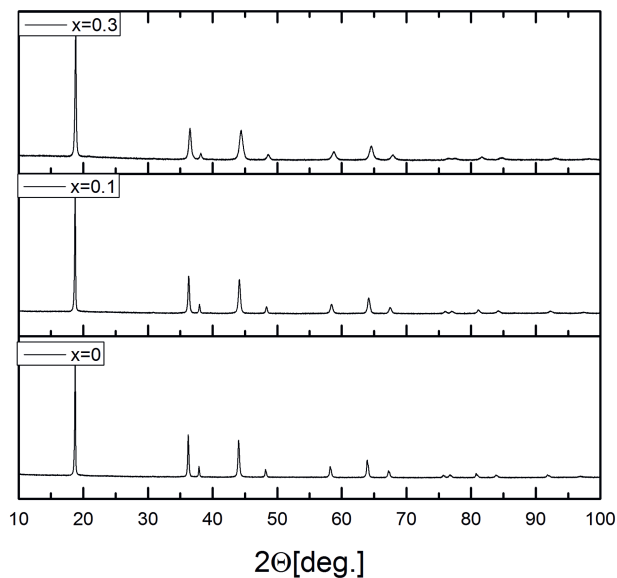
Pulse program used for hahn-echo measurements.



4

4.B. Synthesis of starting spinels

Resulting $\text{Li}_{1+\delta}\text{Mn}_{2-\delta}\text{O}_4$ with $\delta = 0, 0.1, 0.3$. They are all in the spinel crystal structure. SEM micrographs of a) scraped electrode and b-e) elemental mapping.

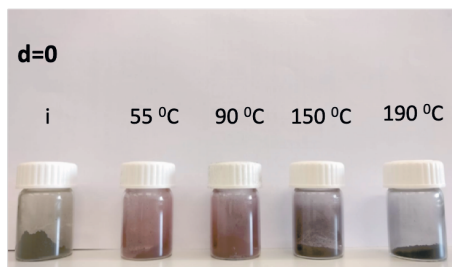
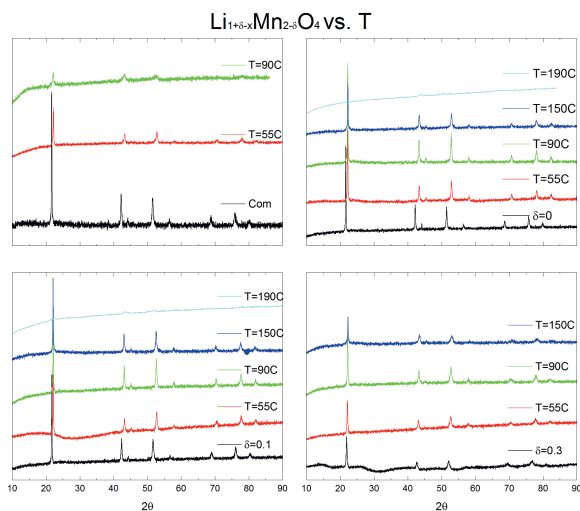


δ	mass ICP, g	Li %w/w	Mn %w/w	Li	Mn	Compound
0	0.0455	1.8	29	0.99	2.012	$\text{Li}_{0.99}\text{Mn}_{2.01}\text{O}_4$
0.1	0.0487	2.5	33	1.12	1.875	$\text{Li}_{1.12}\text{Mn}_{1.88}\text{O}_4$
0.3	0.0448	3.2	33	1.30	1.697	$\text{Li}_{1.30}\text{Mn}_{1.70}\text{O}_4$

4.C. Temperature studies

The resulting materials were characterized by XRD for crystal structure and ICP for Li and Mn content.

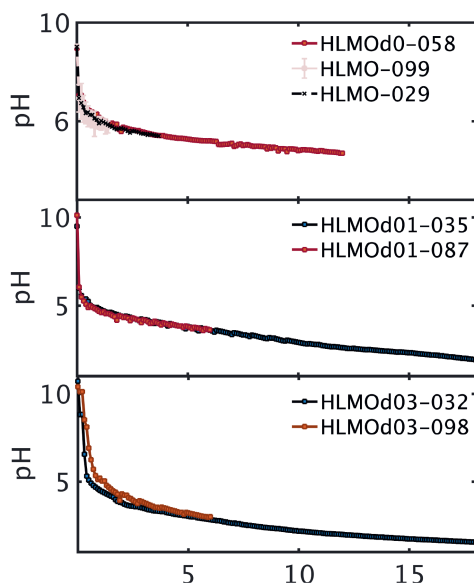
Delta theo	ICP-starting
0	$\text{Li}_{0.99}\text{Mn}_2\text{O}_4$
0.1	$\text{Li}_{1.12}\text{Mn}_2\text{O}_4$
0.3	$\text{Li}_{1.30}\text{Mn}_2\text{O}_4$



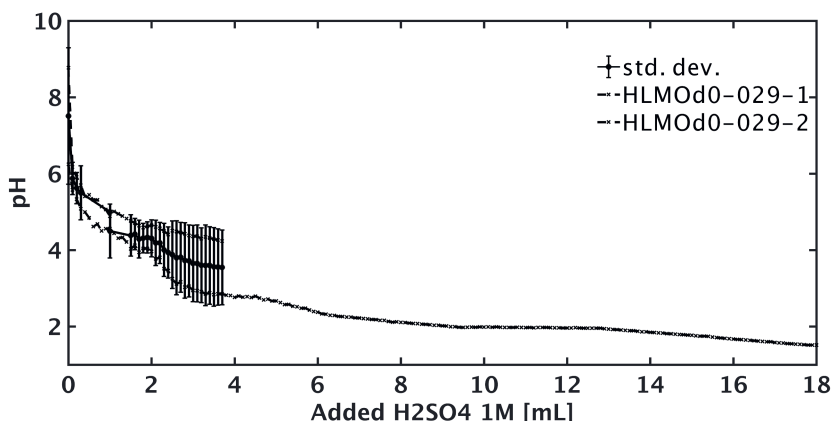
X-ray diffractograms after leaching show the typical reflections of a spinel crystal, as indexed in the previous section, up to 150 °C. At 190 °C, the material has changed into a rutile form (XRD for $\delta = 0.3$ at that temperature was not taken). We also observe that at 55 and 90 °C the powders are of a dark red colour, hinting at a lot of Mn^{3+} ions while at higher temperatures it becomes darker and darker, suggesting more Mn^{4+} ions as would be the case in $\lambda\text{-MnO}_2$.

4.D. Titration curves

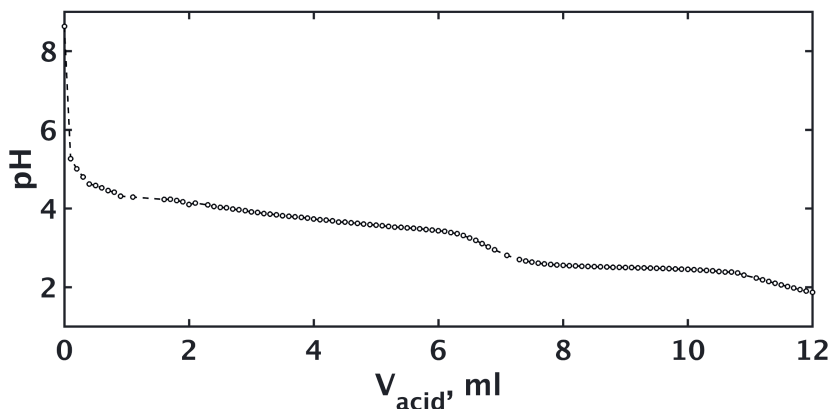
a. Titration curves for all d values with different amounts of acid added. HLMO-029 titration data transfer was stopped at ~ 3 ml, however titration proceeded until the end with 18 ml acid added.



b. Error of titration with different calibration of the burette. Highest pH values during first run(suffix -1), lowest pH values after changing calibration (suffix -2). However, under the same calibration, all resulting curves were fairly consistent. See previous figure; there all different experiments followed the same titration line when adding different amounts of acid. Final pH of HLMO-029-1 was an estimate based on the difference between both curves.

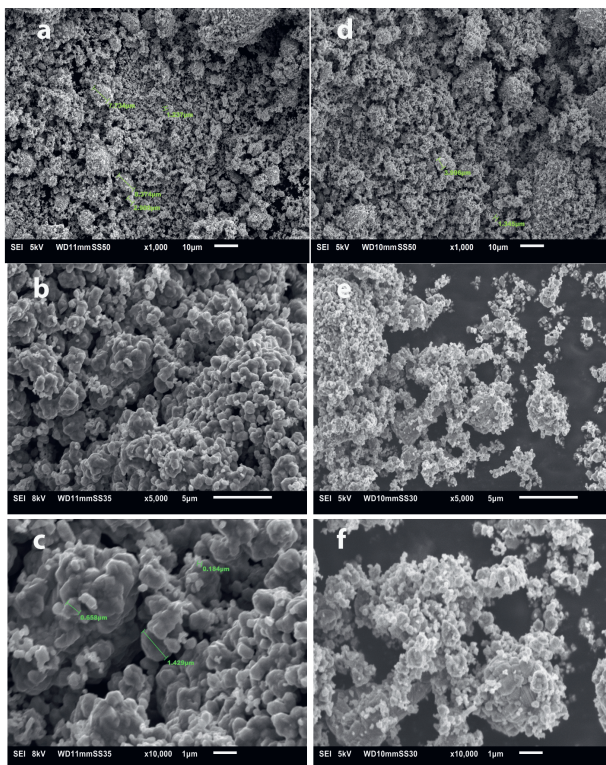


c. Calibration curve with 2g of LMOd0. For this mass of LMO, 12 ml of H_2SO_4 1 M correspond to more than twice the estimated amount to remove all Li. Here we see 2 plateaus. In the first, mostly Li^+ extraction is expected to happen. In the second, and according to ND results, mostly H^+ insertion is expected. This trend was also observed in the previous figure, where de-lithiation of 4 g LMOd0 with 18 ml of H_2SO_4 1 M also reaches this second plateau, where according to ND results, protonation starts to increase following a power law.



4.E. SEM micrographs

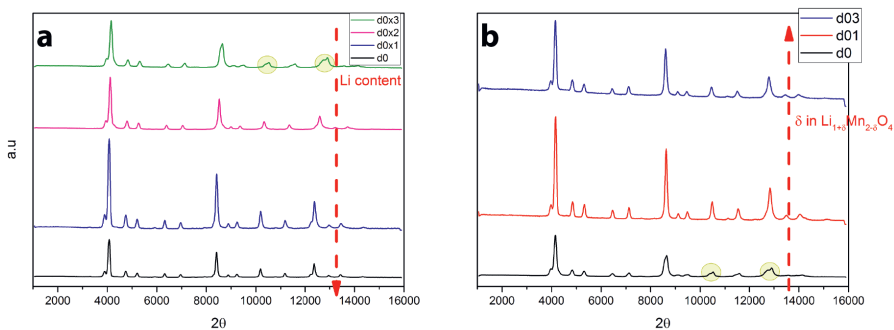
Powders before (a-c, LMOd0) vs. after de-lithiation (d-f, LMOd0-029).



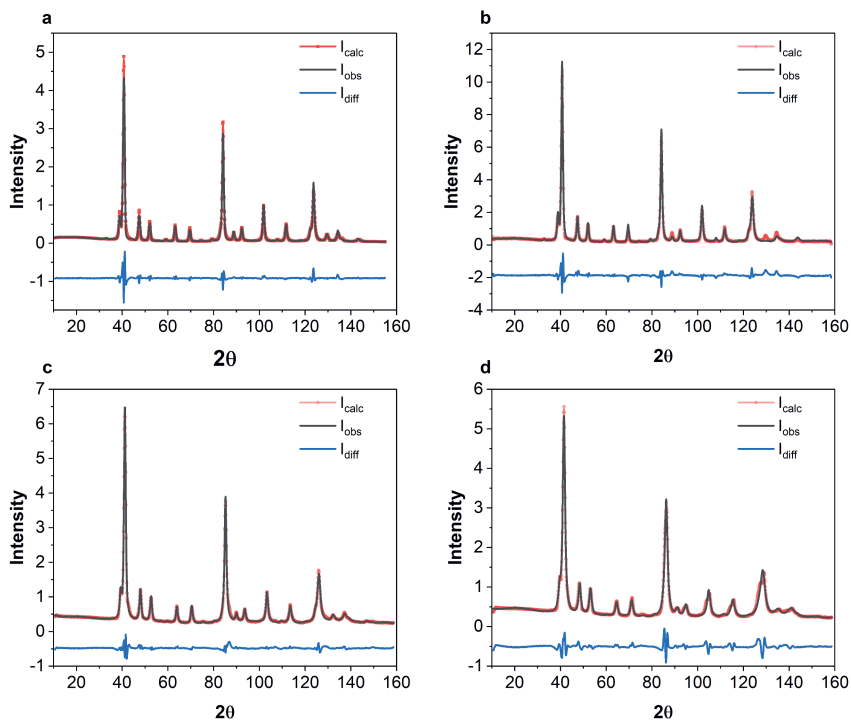
4

4.F. Neutron Diffraction

a. Raw data



b. Rietveld refinement

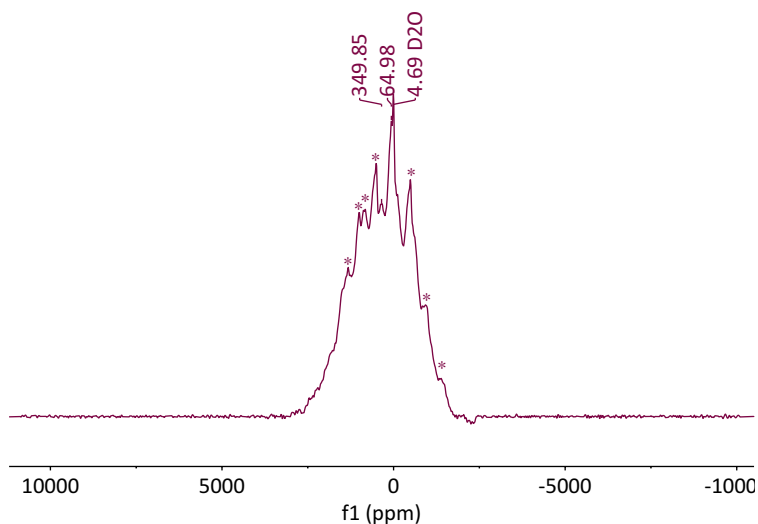


c. Rietveld refinement result summary.

Sample	ICP					Rietveld refinement					
	Li content	a, nm	Lx	Ly	p, nm	H			wRp	O-H, A	Formula
						F	Uiso	y			
LMO	0,98	8,22	38,8	0	24,6	-	-	0	0,11	-	LiMn_2O_4
B18/B37	1,00843161	8,216	48,61	0	19,6	0,0016	0,07896	0,02	0,0978	-	$(\text{H}_{0,02})\text{Li}_{0,99}\text{Mn}_2\text{O}_4$
B19	0,57825637	8,139	62,4	0	15,3	0,0141	0,07896	0,17	0,0546	-	$(\text{H}_{0,17})\text{Li}_{0,58}\text{Mn}_2\text{O}_4$
B22	0,28726348	8,05	96,8	0	9,9	0,03	0,01635	0,36	0,0842	-	$(\text{H}_{0,36})\text{Li}_{0,28}\text{Mn}_2\text{O}_4$
HMO90	0,13	8,02	46,15	0	20,7	0,057	0,03656	0,68	0,073	1,25	$(\text{H}_{0,68})\text{Li}_{0,13}\text{Mn}_2\text{O}_4$

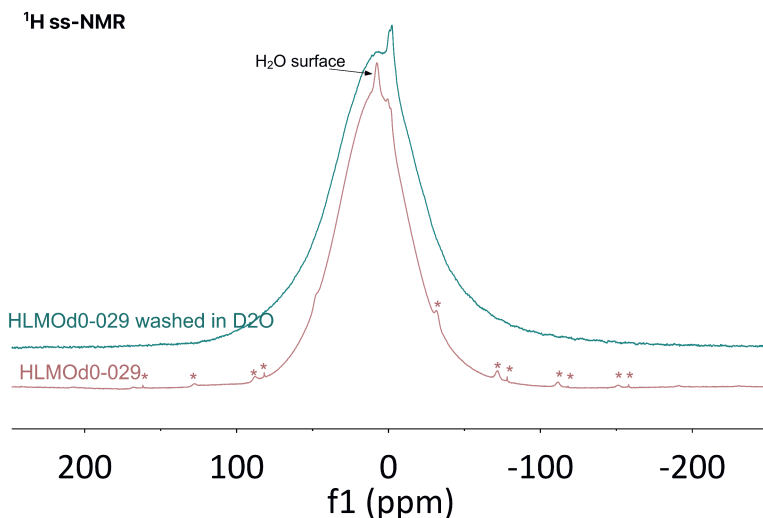
4.G. Solid-state NMR

a. ^2H NMR of DLMO-013L with a hanh-echo sequence Labeled resonances correspond to center bands and those labelled with a star correspond to sidebands.



4

b. Typical ^1H and ^2H NMR spectra with a one pulse sequence of HLMO-013L A broad signal difficult to resolve as a result of the paramagnetic environment in which protons are found. Furthermore, in ^1H measurements protons in the probe obscure the signal further. However, deuteration of the sample reveals that the resonance at 7.8 ppm corresponds to adsorbed water.



4.H. Mn OS validation

The difference in OS of LMO is due to calibration error around OS = 3.5 in XAS experiments. XAS calculations taken from chapter 5.

Sample	Formula	Mn OS, ND	Mn OS, XAS
LMO	LiMn_2O_4	3,50	3,04
B18/B37	$(\text{H}_{0.02})\text{Li}_{0.99}\text{Mn}_2\text{O}_4$	3,49	NA
B19	$(\text{H}_{0.17})\text{Li}_{0.58}\text{Mn}_2\text{O}_4$	3,63	NA
B22	$(\text{H}_{0.36})\text{Li}_{0.28}\text{Mn}_2\text{O}_4$	3,63	3,69
HMO90	$(\text{H}_{0.68})\text{Li}_{0.13}\text{Mn}_2\text{O}_4$	3,59	NA

References

- [1] A. Alaswad, A. Omran, J. R. Sodre, T. Wilberforce, G. Pignatelli, M. Dassisti, A. Baroutaji, and A. G. Olabi, "Technical and Commercial Challenges of Proton-Exchange Membrane (PEM) Fuel Cells," *Energies*, vol. 14, no. 1, p. 144, 2020.
- [2] A. Marinoiu, E. Carcadea, A. Sacca, A. Carbone, C. Sisu, A. Dogaru, M. Raceanu, and M. Varlam, "One-step synthesis of graphene supported platinum nanoparticles as electrocatalyst for PEM fuel cells," *International Journal of Hydrogen Energy*, vol. 46, no. 22, pp. 12242–12253, 2021.
- [3] L. Du, V. Prabhakaran, X. Xie, S. Park, Y. Wang, and Y. Shao, "Low-PGM and PGM-Free Catalysts for Proton Exchange Membrane Fuel Cells: Stability Challenges and Material Solutions," *Advanced Materials*, vol. 33, no. 6, pp. 1–18, 2021.
- [4] Z. Xia, L. An, P. Chen, and D. Xia, "Non-Pt Nanostructured Catalysts for Oxygen Reduction Reaction: Synthesis, Catalytic Activity and its Key Factors," *Advanced Energy Materials*, vol. 6, no. 17, pp. 1–29, 2016.
- [5] C. Wei, Z. Feng, G. G. Scherer, J. Barber, Y. Shao-Horn, and Z. J. Xu, "Cations in Octahedral Sites: A Descriptor for Oxygen Electrocatalysis on Transition-Metal Spinels," *Advanced Materials*, vol. 29, no. 23, pp. 1–8, 2017.
- [6] C. Goswami, K. K. Hazarika, and P. Bharali, "Transition metal oxide nanocatalysts for oxygen reduction reaction," *Materials Science for Energy Technologies*, vol. 1, no. 2, pp. 117–128, 2018.
- [7] K. K. Hazarika, C. Goswami, H. Saikia, B. J. Borah, and P. Bharali, "Cubic Mn₂O₃ nanoparticles on carbon as bifunctional electrocatalyst for oxygen reduction and oxygen evolution reactions," *Molecular Catalysis*, vol. 451, pp. 153–160, 2018.
- [8] A. Harriman, I. J. Pickering, J. M. Thomas, and P. A. Christensen, "Metal oxides as heterogeneous catalysts for oxygen evolution under photochemical conditions," *Journal of the Chemical Society, Faraday Transactions 1: Physical Chemistry in Condensed Phases*, vol. 84, no. 8, pp. 2795–2806, 1988.
- [9] I. Zaharieva, P. Chernev, M. Risch, K. Klingan, M. Kohlhoff, A. Fischer, and H. Dau, "Electrosynthesis, functional, and structural characterization of a water-oxidizing manganese oxide," *Energy and Environmental Science*, vol. 5, no. 5, pp. 7081–7089, 2012.
- [10] Y. Nie, L. Li, and Z. Wei, "Recent advancements in Pt and Pt-free catalysts for oxygen reduction reaction," *Chemical Society Reviews*, vol. 44, no. 8, pp. 2168–2201, 2015.
- [11] C. Ottone, M. Armandi, S. Hernández, S. Bensaid, M. Fontana, C. F. Pirri, G. Saracco, E. Garrone, and B. Bonelli, "Effect of surface area on the rate of

- photocatalytic water oxidation as promoted by different manganese oxides," *Chemical Engineering Journal*, vol. 278, pp. 36–45, 2015.
- [12] S. K. Ghosh and H. Rahaman, *Noble Metal–Manganese Oxide Hybrid Nanocatalysts*. Elsevier Inc., 2019.
- [13] F. H. Lima, M. L. Calegario, and E. A. Ticianelli, "Investigations of the catalytic properties of manganese oxides for the oxygen reduction reaction in alkaline media," *Journal of Electroanalytical Chemistry*, vol. 590, no. 2, pp. 152–160, 2006.
- [14] K. A. Stoerzinger, M. Risch, B. Han, and Y. Shao-Horn, "Recent Insights into Manganese Oxides in Catalyzing Oxygen Reduction Kinetics," *ACS Catalysis*, vol. 5, no. 10, pp. 6021–6031, 2015.
- [15] I. M. Mosa, S. Biswas, A. M. El-Sawy, V. Botu, C. Guild, W. Song, R. Ramprasad, J. F. Rusling, and S. L. Suib, "Tunable mesoporous manganese oxide for high performance oxygen reduction and evolution reactions," *Journal of Materials Chemistry A*, vol. 4, no. 2, pp. 620–631, 2015.
- [16] I. Roche, E. Chaînet, M. Chatenet, and J. Vondrák, "Carbon-supported manganese oxide nanoparticles as electrocatalysts for the Oxygen Reduction Reaction (ORR) in alkaline medium: Physical characterizations and ORR mechanism," *Journal of Physical Chemistry C*, vol. 111, no. 3, pp. 1434–1443, 2007.
- [17] J. Vondrák, B. Klápště, J. Velická, M. Sedlaříková, V. Novák, and J. Reiter, "Carbon/manganese oxide based fuel cell electrocatalyst using "flywheel" principle," *Journal of New Materials for Electrochemical Systems*, vol. 8, no. 1, pp. 1–4, 2005.
- [18] A. Flegler, S. Hartmann, H. Weinrich, M. Kapuschinski, J. Settelein, H. Lormann, and G. Sextl, "Manganese Oxide Coated Carbon Materials as Hybrid Catalysts for the Application in Primary Aqueous Metal-Air Batteries," *C*, vol. 2, no. 1, p. 4, 2016.
- [19] S. J. Venkata, G. A., and R. K., "Morphological and structural analysis of manganese oxide nanoflowers prepared under different reaction conditions," *Applied Surface Science*, vol. 449, pp. 228–232, aug 2018.
- [20] Y. Dessie, S. Tadesse, R. Eswaramoorthy, and B. Abebe, "Recent developments in manganese oxide based nanomaterials with oxygen reduction reaction functionalities for energy conversion and storage applications: A review," *Journal of Science: Advanced Materials and Devices*, vol. 4, no. 3, pp. 353–369, 2019.
- [21] H. Antoni, D. M. Morales, Q. Fu, Y. T. Chen, J. Masa, W. Schuhmann, and M. Muhler, "Oxidative Deposition of Manganese Oxide Nanosheets on Nitrogen-Functionalized Carbon Nanotubes Applied in the Alkaline Oxygen Evolution Reaction," *ACS Omega*, vol. 3, no. 9, pp. 11216–11226, 2018.

- [22] T. Hayashi, N. Bonnet-Mercier, A. Yamaguchi, K. Suetsugu, and R. Nakamura, "Electrochemical characterization of manganese oxides as a water oxidation catalyst in proton exchange membrane electrolyzers," *Royal Society Open Science*, vol. 6, no. 5, 2019.
- [23] F. Cheng, J. Shen, B. Peng, Y. Pan, Z. Tao, and J. Chen, "Rapid room-temperature synthesis of nanocrystalline spinels as oxygen reduction and evolution electrocatalysts," *Nature Chemistry*, vol. 3, no. 1, pp. 79–84, 2011.
- [24] M. Risch, K. A. Stoerzinger, B. Han, T. Z. Regier, D. Peak, S. Y. Sayed, C. Wei, Z. Xu, and Y. Shao-Horn, "Redox Processes of Manganese Oxide in Catalyzing Oxygen Evolution and Reduction: An in Situ Soft X-ray Absorption Spectroscopy Study," *Journal of Physical Chemistry C*, vol. 121, no. 33, pp. 17682–17692, 2017.
- [25] C. Wei, Z. Feng, G. G. Scherer, J. Barber, Y. Shao-Horn, and Z. J. Xu, "Cations in Octahedral Sites: A Descriptor for Oxygen Electrocatalysis on Transition-Metal Spinel," *Advanced Materials*, vol. 29, no. 23, pp. 1–8, 2017.
- [26] S. Park, Y. H. Lee, S. Choi, H. Seo, M. Y. Lee, M. Balamurugan, and K. T. Nam, "Manganese oxide-based heterogeneous electrocatalysts for water oxidation," *Energy and Environmental Science*, vol. 13, no. 8, pp. 2310–2340, 2020.
- [27] U. Maitra, A. Govindaraj, and C. N. Rao, "Importance of trivalency and the eg 1 configuration in the photocatalytic oxidation of water by mn and co oxides," *Proceedings of the National Academy of Sciences of the United States of America*, vol. 110, no. 29, pp. 11704–11707, 2013.
- [28] X. Yang, H. Kanoh, W. Tang, and K. Ooi, "Synthesis of Li(1.33)Mn(1.67)O₄ spinels with different morphologies and their ion adsorptivities after delithiation," *Journal of Materials Chemistry*, vol. 10, no. 8, pp. 1903–1909, 2000.
- [29] S. Y. Sun, X. Song, Q. H. Zhang, J. Wang, and J. G. Yu, "Lithium extraction/insertion process on cubic Li-Mn-O precursors with different Li/Mn ratio and morphology," *Adsorption*, vol. 17, no. 5, pp. 881–887, 2011.
- [30] J. Wang, Y. Liu, H. Zhang, Y. Li, H. Bai, W. Wu, Z. Li, and X. Zhang, "Embedding sulfonated lithium ion-sieves into polyelectrolyte membrane to construct efficient proton conduction pathways," *Journal of Membrane Science*, vol. 501, pp. 109–122, 2016.
- [31] K. Sato, Y. Inoue, S. Yasukawa, and H. Takahashi, "The surface structure formed by H₂ desorption from proton-exchanged HyLi_{1-(x+y)}Mn₂O₄ and its catalytic activity for oxidation of methane and butane," *Applied Surface Science*, vol. 65-66, no. C, pp. 308–312, 1993.
- [32] D. M. Robinson, Y. B. Go, M. Greenblatt, and G. C. Dismukes, "Water Oxidation by λ -MnO₂: Catalysis by the Cubical Mn₄O₄ Subcluster Obtained by Delithiation of Spinel LiMn₂O₄," *Journal of the American Chemical Society*, vol. 132, no. 33, pp. 11467–11469, 2010.

- [33] K. Ooi, Y. Miyai, S. Katoh, H. Maeda, and M. Abe, "Analysis of pH Titration Data in A λ -MnO₂ + LiOH System on the Basis of Redox Mechanism," *Langmuir*, vol. 6, no. 1, pp. 289–291, 1990.
- [34] K. Ooi, Y. Miyai, and J. Sakakihara, "Mechanism of Li Insertion in Spinel-Type Manganese Oxide. Redox and Ion-Exchange Reactions," *Langmuir*, vol. 7, no. 6, pp. 1167–1171, 1991.
- [35] Q. Feng, Y. Miyai, H. Kanoh, and K. Ooi, "Li⁺ Extraction/Insertion with Spinel-Type Lithium Manganese Oxides. Characterization of Redox-Type and Ion-Exchange-Type Sites," *Langmuir*, vol. 8, no. 7, pp. 1861–1867, 1992.
- [36] B. Ammundsen, D. J. Jones, J. Rozière, and G. R. Burns, "Mechanism of Proton Insertion and Characterization of the Proton Sites in Lithium Manganate Spinel," *Chemistry of Materials*, vol. 7, no. 11, pp. 2151–2160, 1995.
- [37] Z. Y. Ji, M. Y. Zhao, J. S. Yuan, J. Wang, J. Q. Zhou, H. B. Yin, and B. Y. Sun, "Li⁺ Extraction from Spinel-Type LiMn₂O₄ in Different Eluents and Li⁺ Insertion in the Aqueous Phase," *Solvent Extraction and Ion Exchange*, vol. 34, no. 6, pp. 549–557, 2016.
- [38] J. C. Hunter, "Preparation of a new crystal form of manganese dioxide: λ -MnO₂," *Journal of Solid State Chemistry*, vol. 39, no. 2, pp. 142–147, 1981.
- [39] H. Heise and S. M. Editors, *Topics in Current Chemistry 335 Modern NMR Methodology*, vol. 335.
- [40] A. J. Pell, G. Pintacuda, and C. P. Grey, "Paramagnetic NMR in solution and the solid state," *Progress in Nuclear Magnetic Resonance Spectroscopy*, vol. 111, pp. 1–271, 2019.
- [41] F. Blanc, C. Copéret, A. Lesage, and L. Emsley, "High resolution solid state NMR spectroscopy in surface organometallic chemistry: Access to molecular understanding of active sites of well-defined heterogeneous catalysts," *Chemical Society Reviews*, vol. 37, no. 3, pp. 518–526, 2008.
- [42] C. P. Grey and N. Dupré, "NMR studies of cathode materials for lithium-ion rechargeable batteries," *Chemical Reviews*, vol. 104, no. 10, pp. 4493–4512, 2004.
- [43] P. Examiner, M. Nuzzolillo, and A. E.-c. Chaney, "United States Patent (19)," 1999.
- [44] B. H. Toby, "EXPGUI, a graphical user interface for GSAS," *Journal of Applied Crystallography*, vol. 34, pp. 210–213, apr 2001.
- [45] A. E. Goldberg, "GSAs," *The SAGE Encyclopedia of LGBTQ Studies*, 2016.
- [46] K. Momma and F. Izumi, "VESTA 3 for three-dimensional visualization of crystal, volumetric and morphology data," *Journal of Applied Crystallography*, vol. 44, pp. 1272–1276, dec 2011.

- [47] S. Bach, S. Belair, C. Cachet-Vivier, J. P. Pereira-Ramos, L. Sanchez, P. Lavela, and J. L. Tirado, "Electrochemical proton insertion in $\text{Mn}_{2.2}\text{Co}_{0.27}\text{O}_4$ from aqueous borate solution," *Electrochimica Acta*, vol. 45, no. 6, pp. 931–934, 1999.
- [48] W. Liu, K. Kowal, and G. C. Farrington, "Mechanism of the Electrochemical Insertion of Lithium into LiMn_2O_4 Spinel," *Journal of The Electrochemical Society*, vol. 145, no. 2, pp. 459–465, 1998.
- [49] L. Xiong, Y. Xu, C. Zhang, Z. Zhang, and J. Li, "Electrochemical properties of tetravalent Ti-doped spinel LiMn_2O_4 ," *Journal of Solid State Electrochemistry*, vol. 15, no. 6, pp. 1263–1269, 2011.
- [50] F. Luo, C. Wei, C. Zhang, H. Gao, J. Niu, W. Ma, Z. Peng, Y. Bai, and Z. Zhang, "Operando X-ray diffraction analysis of the degradation mechanisms of a spinel LiMn_2O_4 cathode in different voltage windows," *Journal of Energy Chemistry*, vol. 44, pp. 138–146, 2020.
- [51] P. Aitchison, B. Ammundsen, T. Bell, D. Jones, J. Rozière, G. Burns, H. Berg, R. Tellgren, and J. Thomas, "Proton insertion in spinel lithium manganates and the effect of manganese substitution," *Physica B: Condensed Matter*, vol. 276–278, pp. 847–848, 2000.
- [52] P. Aitchison, B. Ammundsen, D. J. Jones, G. Burns, and J. Rozière, "Cobalt substitution in lithium manganate spinels: Examination of local structure and lithium extraction by XAFS," *Journal of Materials Chemistry*, vol. 9, no. 12, pp. 3125–3130, 1999.
- [53] B. Ammundsen, M. S. Islam, D. J. Jones, and J. Rozière, "Local structure and defect chemistry of substituted lithium manganate spinels: X-ray absorption and computer simulation studies," *Journal of Power Sources*, vol. 81–82, pp. 500–504, 1999.
- [54] B. Ammundsen, D. J. Jones, and J. Rozière, "X-Ray Absorption Fine Structure Spectroscopy as a Probe of Local Structure in Lithium Manganese Oxides," *Journal of Solid State Chemistry*, vol. 141, no. 1, pp. 294–297, 1998.
- [55] B. Ammundsen, M. S. Islam, D. J. Jones, and J. Rozière, "Computer modelling of lithium and proton intercalation in spinel lithium manganates: Effect of octahedral vacancies," *Molecular Crystals and Liquid Crystals Science and Technology Section A: Molecular Crystals and Liquid Crystals*, vol. 311, pp. 109–114, 1998.
- [56] D. M. Pickup, D. Simon, M. Fookan, H. Krampitz, E. R. Van Eck, and E. M. Kelder, " ^6Li MAS NMR study of stoichiometric and chemically delithiated $\text{Li}_x\text{Mn}_2\text{O}_4$ spinels," *Journal of Materials Chemistry*, vol. 13, no. 4, pp. 963–968, 2003.

- [57] V. W. Verhoeven, I. M. De Schepper, G. Nachtegaal, A. P. Kentgens, E. M. Kelder, J. Schoonman, and F. M. Mulder, "Lithium dynamics in LiMn₂O₄ probed directly by two-dimensional ⁷Li NMR," *Physical Review Letters*, vol. 86, no. 19, pp. 4314–4317, 2001.
- [58] F. Dogan, J. R. Croy, M. Balasubramanian, M. D. Slater, H. Iddir, C. S. Johnson, J. T. Vaughey, and B. Key, "Solid state NMR studies of Li₂MnO₃ and li-rich cathode materials: Proton insertion, local structure, and voltage fade," *Journal of the Electrochemical Society*, vol. 162, no. 1, pp. A235–A243, 2015.
- [59] B. Berglund and R. W. Vaughan, "Correlations between proton chemical shift tensors, deuterium quadrupole couplings, and bond distances for hydrogen bonds in solids," *The Journal of Chemical Physics*, vol. 73, no. 5, pp. 2037–2043, 1980.
- [60] G. M. Nolis, A. Adil, H. D. Yoo, L. Hu, R. D. Bayliss, S. H. Lapidus, L. Berkland, P. J. Phillips, J. W. Freeland, C. Kim, R. F. Klie, and J. Cabana, "Electrochemical Reduction of a Spinel-Type Manganese Oxide Cathode in Aqueous Electrolytes with Ca²⁺ or Zn²⁺," *Journal of Physical Chemistry C*, vol. 122, no. 8, pp. 4182–4188, 2018.

5

Protonated LiMn_2O_4 (HLMO) as Electrocatalysts For Hydrogen Oxidation and Oxygen Reduction Reactions in PEMFCs

*Insofar as it is possible to divide people into categories,
the surest criterion is the deep-seated desires that orient them
to one or another life-long activity.*

Milan Kundera, *The Unbearable Lightness of Being*

A. L. Rangel-Cárdenas, M. Fehse, S.J Picken, G. J. Koper and E.M. Kelder. Protonated spinel Lithium Manganese Oxides as electrocatalysts for HOR and ORR in PEMFCs. ***In preparation.***

Manganese oxides in different crystal structures have been extensively studied as catalysts to multiple reactions, especially the spinel types have been presented as promising alternatives for ORR in alkaline conditions. The activity of these materials has been shown to stem mainly from the Mn^{3+}/Mn^{4+} redox couple, however, their study in PEMFCs has been somewhat limited. In this work we show a spinel lithium manganese oxide (LMO) obtained from chemical de-lithiation route where Li^+ to H^+ exchange preserves the crystal structure and a disordered cubic LMO resulting from the MEA fabrication process. Electrochemical activity has been studied for both materials, ex-situ (for cubic spinel LMO) and in operando (for cubic disordered LMO) with X-ray absorption spectroscopy (XAS) at Mn k-edge in a PEMFC. All membrane-electrode assemblies (MEAs) used Pt as counter electrode and a Nafion® solid electrolyte. We find indications that these materials can chemically split H_2 gas by a slight change in the Mn edge when exposing the powders to 1 atm of H_2 . Further ex-situ studies show reversible electrochemical extraction (ORR) and insertion of protons (HOR) in the spinel structure, at the same time demonstrating a series of structural changes, e.g. Mn oxidation state (OS), Mn–O bond lengths (BL), Mn coordination number (CN) and oxygen vacancy formation/annihilation, depending on operation as whether a HOR or ORR electrocatalyst. Finally, operando measurements of Mn k-edge in disordered LMOs show a stable Mn oxidation state throughout operation suggesting stability of Mn in contact with a solid electrolyte, as opposed to its instability in acidic liquid electrolyte as found in traditional voltammetry measurements. These results highlight the importance of screening new materials in real operating conditions as often traditional ex-situ techniques cannot fully reflect the real environment and thus misleading conclusions may be reached preventing us from following up promising studies. In short, we show that spinel type and strongly reduced HLMOs in cubic structures with variable structural parameters are active to both relevant reactions in an acidic environment, thus opening a wide range of possibilities for low-cost electrocatalysts that can be fine-tuned according to application.

5.1. Introduction

Platinum fast kinetics towards ORR and HOR in acidic media makes it the golden standard catalyst for proton-exchange membrane fuel cells (PEMFCs). However, its high cost and susceptibility to CO poisoning have been a major impediment to the establishment of PEMFCs as more attractive clean energy devices. This has led to a research focus on lowering the Pt loading at the cathode where the more sluggish ORR takes place and to the development of non-noble metal catalysts [4].

In this quest, transition metals oxides (TMOs) have recently attracted a lot of attention because of their low cost and their variable oxidation states which combined with high electrical conductivity gives them interesting chemical properties [4–7]. For instance, manganese oxides in different crystal structures have been extensively studied as catalysts in many different applications, e.g. in the conversion of CO, NO_x, SO_x and other volatile organic compounds, decomposition of ozone and hydrogen peroxides, organic reduction and oxidation, removal of bacterial pathogens, epoxidation of olefins, photo-/electrochromics and oxygen evolution and reduction reactions (OER and ORR) [5, 7–12]. More specifically, in terms of ORR activity MnO, MnO₂, Mn₃O₄, MnOOH, Mn₂O₃ and Mn₅O₈ have all been shown to be highly active in alkaline conditions [3, 10, 11, 13, 14]. However, despite their historic potential as catalysts to ORR and OER in alkaline and neutral conditions in e.g. metal-air batteries [15–19], alkaline fuel cells [14, 16, 19], microbial fuel cells [19, 20] and electrolyzers [14, 21, 22], research on manganese oxides as catalysts in PEMFCs has been rather limited. In fact, to our knowledge only a few studies concerning acidic environments are available to date. Huynh et al. [23] studied MnO_x activity to OER on a wide pH range and suggested that these materials can be activated to function as catalysts in acidic environments by exploiting a self-healing process that consists of oxidative electrodeposition of dissolved Mn ions. Another study by Hayashi et al. researches four MnO₂ polymorphs as catalysts in PEM electrolyzers [22] with the finding that Mn/C catalyst has similar performance to Pt/C catalysts when evaluated by their 2 mA·cm⁻² potential in liquid electrolyte and the 2 V current density when using a solid electrolyte. However, direct application of manganese oxides in PEMFCs is even more scarce; Mirshekari and Shirvanian [24] studied commercial Mn₂O₃ and Mn₃O₄ at variable particle sizes as catalyst to ORR by the rotating disk electrode technique in 0.1 M HClO₄ [24], and Mosa et al. have suggested Cs-MnO_x as potential catalyst in PEMFCs, especially in methanol fuel cells, although activity in acidic electrolyte was not directly tested [14]. We presume that the lack of documentation of MnOs in acidic media is due to the thermodynamic instability predicted by Pourbaix for Mn at low pH values [25]. However, in the last few years the stabilization of TMOs against corrosion in acidic conditions for PEM electrolyzers has started to gain attention with a few suggestions already found in the literature for manganese oxides, e.g. addition of titanium oxide or doping with fluorine [22, 26, 27]. These findings, though in early stages, open up the possibility of engineering Earth abundant TMOs in order to use them as catalysts in acidic environments.

On the other hand, catalysis in alkaline media research often suggests active materials that allow reversible proton insertion and various manganese oxides have

been studied in that respect, e.g. Mn_2O_3 , Mn_3O_4 , and MnO_2 [7, 9, 11]. Particularly manganese oxides in cubic crystal structures such as spinel manganese oxides have been shown as promising alternatives for ORR in alkaline conditions [4–7, 10, 28, 29]. These cubic spinel class of materials with formula AMn_2O_4 have been shown to be more catalytically active than their tetragonal counterparts as they have better affinity towards oxygen adsorption as well as higher density of active sites [4, 28]. It has been elucidated that presence of the oxidation states 3+ and 4+ with ratio $\text{Mn}^{3+}:\text{Mn}^{4+} > 1$ is vital for the four electron ORR pathway [13]. This suggests higher catalytic activity in the Mn^{3+} species which has been attributed to the presence of one extra electron resulting in Jahn-Teller distortion, a well-known phenomenon in manganese oxides [14, 30].

An interesting class of spinel-type materials with mixed $\text{Mn}^{3+}/\text{Mn}^{4+}$ oxidation states are lithium manganese oxides $\text{Li}_{1+\delta}\text{Mn}_{2-\delta}\text{O}_4$ ($0 < \delta < 1/3$). These are commonly used cathodes in Li-ion batteries, but have been shown to be selective absorbents [31–33], useful catalysts to the oxidation of methane and butane as well as to water oxidation in photocatalytic systems [34, 35]. Recently, LiMn_2O_4 (LMO) was used as an inorganic filler for PEMFC membranes [33], where the result was increased proton conductivity.

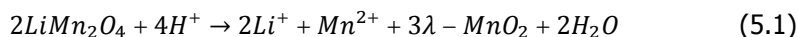
Spinel LMOs become particularly interesting once lithium has been extracted from the structure in strong acidic media [36–40]. Lithium extraction is the result of a disproportionation reaction of Mn^{3+} to Mn^{2+} and Mn^{4+} as proposed by Hunter [41] and an ion-exchange reaction where Li^+ ions are exchanged with H^+ [37, 38]. The result is a spinel product with overall stoichiometry $\text{H}_{(1-x)-y}\text{Li}_{1-x}\text{Mn}_2\text{O}_4$ (HLMO). This proton-exchanged LMO shows improved catalytic activity for the oxidation of methane and n-butane [34]. Furthermore, H_2 thermal desorption from HLMO has been shown to form a stable spinel phase in up to 200 °C [34]. These combination of properties, e.g. tunable $\text{Mn}^{3+}/\text{Mn}^{4+}$ ratio, Li^+/H^+ ion exchange in acidic media with H^+ recombination into H_2 , together with their ability to act as catalysts in similar systems, make spinel HLMOs an interesting material to study as ORR and HOR electrocatalyst for PEMFCs, i.e. in acidic environments.

The ionic substitution in the LMO structure induces local structural and electronic perturbations, which can affect lithium and proton diffusion in the lattice and so their chemical and electrochemical performance. A better understanding of the structural effects of proton exchange can be gained by examining the local structural and electronic environment of the HLMOs by X-ray Absorption Spectroscopy (XAS). XANES and EXAFS at the Mn K-edge have been used to study Mn oxidation state in battery materials [30, 42, 43] as well as to probe its electronic configuration. Here, we study the Mn K-edge of proton-exchanged manganese oxides as both anode and cathode in ex-situ and operando conditions in a PEMFC to find out whether they can act as electrocatalysts and what is the role of $\text{Mn}^{3+}/\text{Mn}^{4+}$ and H^+ ions in their functionality. Understanding the effect of proton substitution on the local structure of the spinel LMOs can provide important insights into how the structure of these materials can be tailored to give optimum electrochemical properties.

5.2. Experimental

5.2.1. Synthesis

Spinel LiMn_2O_4 was prepared by a solid state reaction as detailed in Chapter 4. Shortly, $\text{LiOH}\cdot\text{H}_2\text{O}$ (Merck) and $\text{Mn}(\text{CH}_3\text{COO})_2\cdot 4\text{H}_2\text{O}$ (Fluka) were mixed in a molar ratio Li:Mn of 1:2 and left to dissolve in their own crystal water while heating up to 100 °C under constant stirring. Two calcination steps followed at 500 °C and 700 °C for 5 and 10 h, respectively. The samples were ball-milled at 750 rpm for 30 min in 2 cycles of 15 min with opposing directions. The resulting LMO powder was chemically de-lithiated to three different compositions by titration with 1 M H_2O_4 using a Metrohm DMS Titrino 716 titrator as described in Chapter 4. An extra reference sample was prepared by mixing 4 g LMO in 75 ml 5% HCl for 24 h under constant stirring at room temperature. The amount of solution was chosen to be at least twice the stoichiometric protons necessary to achieve complete delithiation following equation 5.1:



All samples were vacuum filtered and washed several times with demineralized water and finally dried in a vacuum oven at 55 - 90 °C for at least 24 h. De-lithiated, proton-exchanged LMO samples are referred to as HLMO for simplicity.

In table 5.1 a summary of the tested and analysed materials as prepared in Chapter 4 is shown.

Table 5.1: Li content and sample labels.

Sample	Li content, (1-x)	Preparation	Short name
LiMn_2O_4 home-made	1	Solid state synthesis	LMO
Delithiated LMO, composition 1	0.29	Titration with 1 M H_2SO_4	HLMO-029
Delithiated LMO, composition 2	0.58	Titration with 1 M H_2SO_4	HLMO-058
Delithiated LMO, composition 3	0.99	Titration with 1 M H_2SO_4	HLMO-099
Delithiated LMO, composition 4	0.13	Leaching in 5% HCl	HLMO-013L

5.2.2. Membrane Electrode Assembly (MEA) preparation

Inks with the active material were prepared by stirring 45 mg HLMO, 45 mg carbon black and 1.2 g Nafion™ solution (PFSA 5 wt.%, Quitech) in 9 ml ethanol for five minutes. The solution was then dispersed in an ultrasound bath for 30 minutes. The resulting inks were sprayed onto a carbon gas diffusion layer (Fuel Cell store, GDL 340C) and left to dry on a hotplate for 2 h so as to obtain working electrodes with an HLMO loading of 0.1 mg·cm⁻². Finally, the MEAs were prepared by hot-pressing together a working electrode, a Nafion™ 117 membrane (thickness of 0.007 in) and a Pt counter electrode (Fuel Cell store, L=0.5 mg·cm⁻²) at 30 kN and 135 °C for 90 s.

5.2.3. Characterization

The samples were analysed by XRD with a Bruker D8 ADVANCE diffractometer (Co $K\alpha$, $\lambda = 0.1789$ nm) and the SEM micrographs were obtained using a JEOL JSM-6010 LA with a standard beam potential of 5 kV. Lithium and manganese content were analysed by ICP-OES using a Perkin Elmer Optima 5300DV instrument.

5.2.4. Electrochemical measurements

The HLMOs were tested in a three-electrode electrochemical cell using the rotating disk electrode (RDE) with a 5 mm glassy carbon disk (PINE Instruments) and an Autolab potentiostat. The working electrode was prepared by coating the glassy carbon disk (0.196 cm²) with an ink of the active material. The ink consisted of 4 mg HLMO, 2 mg Vulcan XC-72R and 4.56 μ L Nafion™ (solution at 5 wt.%) dispersed in 12 mL IPA by sonication for 30 minutes. Finally, a 13 μ L aliquot was deposited onto the glassy carbon and left to dry at room temperature inside a fumehood. A Pt wire was used as counter electrode and all measurements were taken against a RHE electrode in 0.1 M HClO₄ electrolyte. The electrolyte was purged with either Argon or Oxygen for 30 min prior to any experiment. Cyclic voltammetry (CV) measurements were recorded at a scan rate of 50 mV·s⁻¹.

The electrochemical protonation and deprotonation of HLMOs was done in a fuel cell configuration. Here, the working electrode was made by pressing 6 mg of powder (in a 1:1 ratio of HLMO:Vulcan) onto a carbon gas diffusion layer (Fuel Cell store, GDL 340C) in a 10mm dye at 7000 lb for 2 minutes. The fuel cell was then assembled by putting together the working electrode, a Nafion™117 membrane and Pt as counter electrode. The components were held together by simply tightening the cell; no MEA was fabricated in this case (see Appendix 5.A). Hydrogen and oxygen gases were produced in-situ with an electrolyser kit (Fuel Cell store). For the proton discharge, or deprotonation, the HLMO electrode was used at the oxygen side of the cell while cutting off the feed from the hydrogen side. A constant voltage of 0.01 V was applied for 300 s until a stable current (close to 0 A) was reached. At this point, the material was assumed to have used any protons left in the structure to recombine with the oxygen feed to produce water. On the other hand, for (further) protonation the HLMO was used at the hydrogen side of the cell while blocking the feed from the oxygen side. Again, a constant voltage of 0.01 V was applied for 300 s until a stable current (close to 0 A) was reached. At this point, insertion of as many protons as possible in the structure by oxidising hydrogen gas is assumed. Finally, in order to study the veracity of proton insertion and its reversibility in the spinel HLMOs, a material that was cycled between protonation and deprotonation was prepared ending in a protonated state.

5.2.5. X-ray absorption (XAS) measurements

All X-ray absorption spectra presented here were collected on the BM26A (DUBBEL) beamline at the European Synchrotron Radiation Facility (ESRF) in Grenoble, France. The storage ring was operated at an energy of 6 GeV and a beam current of 200 mA. A Si(111) monochromator was used to tune the energy of the incident beam

before entering the cell to 6.5 keV to match Mn K-edge. The spot size of the X-ray beam on the sample was 2 mm² (fwhm). For the operando measurements, two windows of 1 cm² in diameter were cut on the MEAs at the Pt side in order to allow the beam to pass through and into the HLMO side of the fuel cell. The gases were humidified by flow through a bubbler prior to entering the FC (See picture of set-up in Appendix 5.B). The electrochemical tests were performed in galvanostatic mode using a MACCOR battery testing system with a maximum current setting of 1 A. The MACCOR program was set in current steps from 0.001C to 10C of 30 min while the voltage response was measured. Powder measurements were done by pressing a pellet onto Kapton tape. In order to identify the oxidation state in the HLMO samples, references with known oxidation state and comparable coordination geometry were also measured, e.g. MnO, Mn₂O₃, Mn₃O₄, MnO₂ and LiMn₂O₄.

5.2.6. XAS Data Analysis

Processing and analysis of the data were performed with the Athena and Artemis software packages, using IFEFFIT. The energy was calibrated using the first maximum of the first derivative (see Appendix 5.C). Measurements were taken duplicate or triads and then merged together in Athena. First-shell EXAFS fitting was performed in k² weighting (checking k¹ and k³ during analysis) over the energy range $2 < k < 10 \text{ \AA}^{-1}$ and distance range $1.25 < R < 3.0 \text{ \AA}$ on the basis of the face-centred cubic (fcc) crystal model. The amplitude reduction factor, *s*₀₂, was set to a value of *s*₀₂ = 0.85 (taken from literature [44]). Second shell fitting was performed in *k* and distance ranges. Both shells were fit with restrained *E*₀ and amplitude reduction factor, *S*₀₂, to be the same for both paths. All crystals were drawn using free software VESTA [45].

5.3. Results

5.3.1. Synthesis

Figure 5.1 (taken from Chapter 4) shows a reference titration curve for home-made LMO where two plateaus indicating a reaction in two steps are present. According to this, three points were chosen for analysis: beginning of the first plateau, transition region and end of the second plateau (figure 5.1a). Figure 5.1b shows X-ray diffractograms of the prepared samples, confirming a cubic spinel crystal structure.

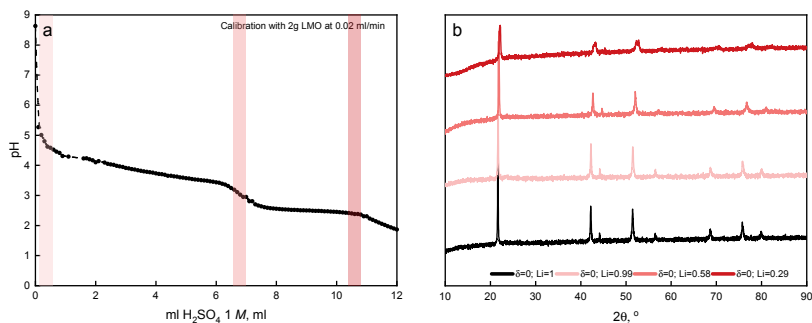


Figure 5.1: Synthesized vs. commercial spinel $LiMn_2O_4$.

5.3.2. MEA fabrication

Nafion addition to manganese oxides has been reported to reduce Mn ions from Mn^{3+} to Mn^{2+} oxidation state [46]. We monitored changes to our spinel materials by XRD and XANES from powder to MEA as Nafion is added to the ink used for the electrode. Results are shown in figure 5.2.

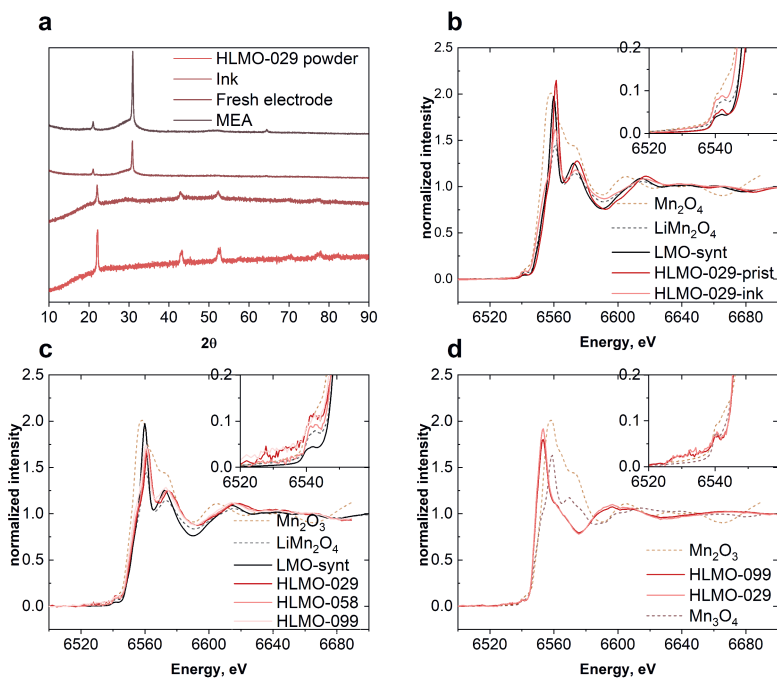


Figure 5.2: Changes of the starting spinel type from powder to MEA: (a) XRD of powder to MEA, (b) XAS comparison with an HLML-029 ink, (c) XAS comparison of electrodes, (d) XAS comparison of MEAs.

The spinel crystal structure remained upon addition of Nafion to the ink, however some changes can be observed in the diffractograms shown in figure 5.2a, i.e. increased background, broader line shapes and peak shift. XANES measurements reveal that the spinel types have been slightly reduced after Nafion addition, from 3.69+ to 3.39+. The EXAFS region (see Appendix 5.D) shows a 2-shell structure similar to that of a spinel, while the pre-edge region (see inset in figure 5.2b) shows two characteristic oscillations related to Mn 3d t_{2g} and e_g energy levels characteristic of Mn^{3+} and Mn^{4+} oxidation states in spinel LMOs. In general, Nafion did induce a slight overall reduction in Mn oxidation state but it did not affect its crystal structure.

On the other hand, results from electrodes with different compositions show an increase oxidation state as Li content decreases. Removal of positive charges (Li^+ ions) would result in charge compensation by Mn nuclei if no other positive charges, i.e. H^+ , are introduced in the lattice. Thus, it follows that proton-exchange is not a 1:1 process. From XANES results it is evident that HLMO in the fresh electrodes is in the spinel form, however, from XRD results it is not so clear. Carbonaceous species from the ink and substrate dominate X-ray diffraction, however on closer inspection reflections belonging to a cubic spinel can be seen along with new reflections where $MnSO_4 \cdot H_2O$, Mn_5O_8 and $Li_2Mn_2O_4$ have been identified as possible candidates (see Appendix 5.E). The lowered intensity of HLMO is due to its lower concentration in the solid mixture with Vulcan. However, there are several signs that the crystallinity of the material has somewhat changed, e.g. broader line shapes, increased background intensity, and particularly broad lines or “bumps” around $2\theta=50^\circ$ and 22° which indicate a more amorphous material. The resulting material in the MEA is more closely related to a distorted tetragonal spinel as in Mn_3O_4 (Mn OS=2.66+) as seen from the pre-edge features and edge position (see figure 5.2 insets).

Mn ions in manganese oxides can adopt several oxidation states which give them the versatility of forming different crystal structures. However, slight changes in Mn^{3+}/Mn^{4+} ratio can result in a slightly different overall oxidation state and corresponding unit cell size. As the synthesis process is not homogeneous and de-lithiation depends on surface area, it is possible that not all grains are equally de-lithiated and instead a mixture of several crystals with slightly different compositions, and subsequent oxidation states and lattice parameters, result. Thus, XRD, XAS and ICP results reflect but merely the average of the material. Broader line shapes in x-ray diffractograms of powders can be explained by several crystals with slightly different lattice parameters, however, all of them belong to the cubic spinel family. Spinel crystals can be cubic (as in LMO where Mn^{3+} and Mn^{4+} exist together, average OS=3.5+) or be distorted to a tetragonal unit cell (as in Mn_3O_4 where there is a mix of Mn^{2+} and $^{3+}$, with average OS=2.66+). Both have close-packed oxygen lattice and differ mainly in the filling of octahedral (Oh) and tetrahedral (Th) sites with Mn ions [47].

From XRD and XAS spectra of MEAs, the material can now be understood as a mixture of several distorted tetragonal spinel crystal types with different compositions whose average oxidation state is $\sim 2.66+$. We shall refer to them now as

disordered spinels (HLMO-dis).

5.3.3. Cubic spinel types as potential ORR and HOR catalysts

Figure 5.3a shows conventional voltammetry in 1 M HClO₄ saturated with Argon. As an example, the first 50 cycles of an HLMO-029 layer are shown. In general, HLMO is very unstable in acid liquid electrolyte as predicted by Pourbaix at this pH and potential [25]. Under these conditions, Mn⁴⁺ species dissolve as Mn²⁺ ions in the acid electrolyte and this process corresponds to the redox couple centred at ~1.4 V vs. SHE. Once the material was stabilized, further cycles were measured under oxygen saturation (5.3b) and a clear increase in the reduction current is observed at ~0.7 V vs. RHE, thus indicating ORR activity. However, ORR has a high overpotential and HLMO suffers initial changes in liquid electrolyte.

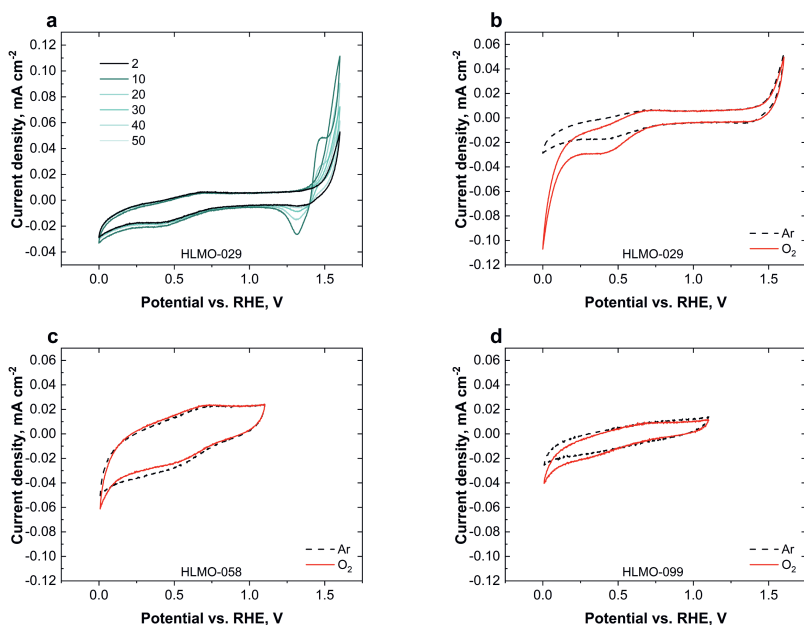


Figure 5.3: Voltammetry on cubic spinel types.(a) First 50 CVs of HLMOd0-029 in Ar-saturated 0.1 M HClO₄. (b) Stabilised HLMOd0-029 in Ar-saturated electrolyte (black) vs. O₂-saturated electrolyte (red); (c) Stabilised HLMOd0-058 in Ar-saturated electrolyte (black) vs. O₂-saturated electrolyte (red); and (d) Stabilised HLMOd0-099 in Ar-saturated electrolyte (black) vs. O₂-saturated electrolyte (red)

The highest activity in O₂ is observed in the most de-lithiated HLMO sample, suggesting that proton insertion is related to activity. Furthermore, it is noteworthy that as a semiconductor *LiMn₂O₄* has a low electrical conductivity, thus additives are necessary to improve current density. Figure 5.4 shows CVs of HLMOs/Vulcan in Ar-saturated electrolyte which present a current density ~6 times higher than

their pure HLMO counterparts.

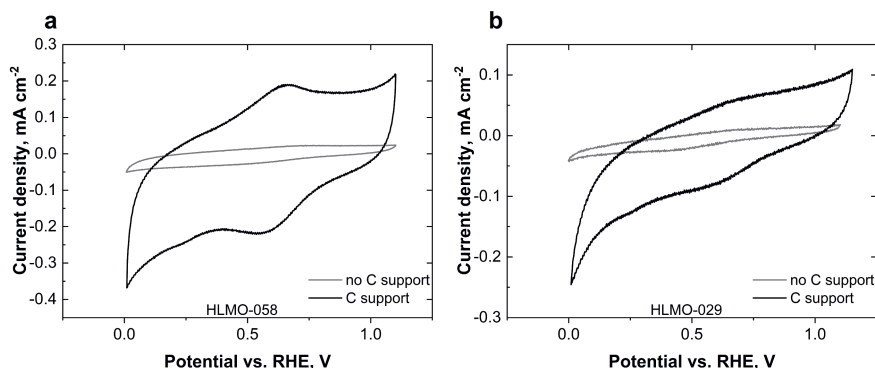


Figure 5.4: Voltammograms of HLMOs vs. HLMO/Carbon support of: (a) HLMOd0-058 and (b) HLMOd0-029.

On the other hand, to probe hydrogen oxidation in HLMOs, powders and MEAs were exposed to a 1 bar of H_2 flow and XANES spectra at Mn k-edge were recorded before and after exposure. Figure 5.5a shows a comparison of XANES spectra under air vs. H_2 flow. In HLMO-013L powder, there is a slight decrease in Mn k-edge energy meaning Mn reduction as the HLMO takes in positive charges, with an average OS of $\sim 3.96+$ (this was a sample leached in acid for 24h). In figure 5.5, a pristine MEA from HLMO-029 was exposed to H_2 flow before operation. In this case, Mn reduction is more noticeable with an average OS change from $2.71+$ in the pristine MEA to $2.59+$ after applying 1 bar of H_2 . In both cases, inspection of the pre-edge features suggests no change in Mn coordination or local structure and resembles that of a spinel-like crystal. In both, cubic spinel powder and disordered spinel types in the MEA, hydrogen was oxidised as protons that were taken up by the structure.

5.3.4. XAS of disordered HLMO in *operando* fuel cells

HLMO-dis MEAs (vs. Pt) were tested in *operando* conditions as either an oxygen or hydrogen electrode. Typical voltage and current vs. time curves using a constant current program are shown in figure 5.6b. Figure 5.6a shows XANES spectra for a HLMO-029 vs. Pt cell, with HLMO-dis at H_2 side under a constant voltage program. During operation there is no change in oxidation state (i.e. no change in energy edge) or pre-edge features and “white line” intensity (A), suggesting a stable reaction with fast kinetics, i.e. charge in = charge out in the timescale of the measurement. (See Appendix 5.F for electrochemical measurements at near short-circuit conditions).

On the other hand, during ORR operation the behaviour of HLMO is more nuanced as seen in figure 5.6c (with a constant current program). Mn oxidation state increases slightly from 2.52 to $2.65+$ while the “white line” intensity (A) increases

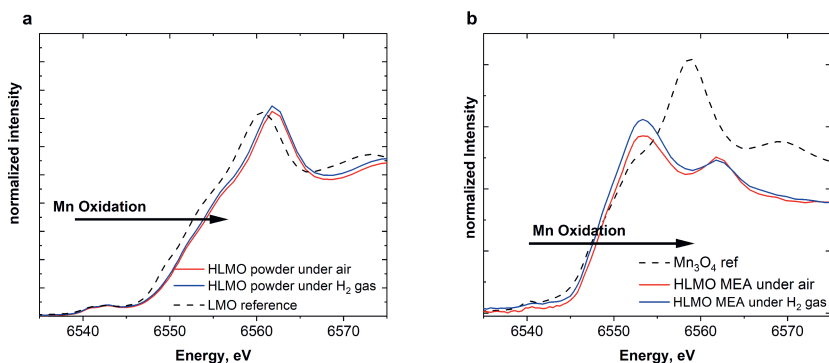


Figure 5.5: XANES under air (red) vs. under 1 bar H_2 (blue). (a) Powder and (b) MEA.

5

and shoulder B intensity decreases. These changes could be related to oxygen atoms in the lattice as the white line intensity represents transitions to 4p hybridised states [48–52] for 3d metals and the first oscillation after the edge represents wave interference with the nearest neighbour, i.e. oxygen in this case [49, 53, 54]. The relation of this structural feature to operation as either HOR or ORR electrocatalyst was further studied by cycling a pristine cell (HLMO-013L vs. Pt) between operation at O_2 or H_2 side. Figure 5.6d shows a comparison of XANES spectra as follows: i) pristine cell; ii) end of operation as ORR electrocatalyst; iii) subsequent operation as HOR electrocatalyst. Initially, the structure related to shoulder B exists in the pristine cell, however, at the end of operation at ORR side, shoulder B intensity has significantly decreased together with an increase in the “white line” intensity (A). Taking the material at this state and flipping the gas flows, the HLMO was subsequently operated as a HOR electrocatalyst. In this case, the inverse tendency was observed, i.e. “white line” intensity decreased while shoulder B was formed again. This phenomenon suggests that the structure related to shoulder B is reversible and fundamental for operation of the material as electrocatalyst to one reaction or the other.

5.3.5. Ex-situ measurements of pure cubic spinel HLMO in a PEMFC

To further investigate the mechanisms of these reactions e.g. nature of shoulder structure (B), its relation to spinel manganese oxides and other structural features, pure cubic spinel HLMO-029 was studied ex-situ by electrochemical (de-)protonation to the feasible extremes. This was achieved by the procedure detailed in section 5.2.4 and illustrated in figure 5.7 a and b.

Figure 5.7 shows the comparison of XANES measurements of the resulting materials against pristine cubic spinel HLMO-029 powder. Again, changes in “white line” and shoulder structure intensities have been observed according to functionality along with more pronounced changes in oxidation state, i.e. from 3.74+ to

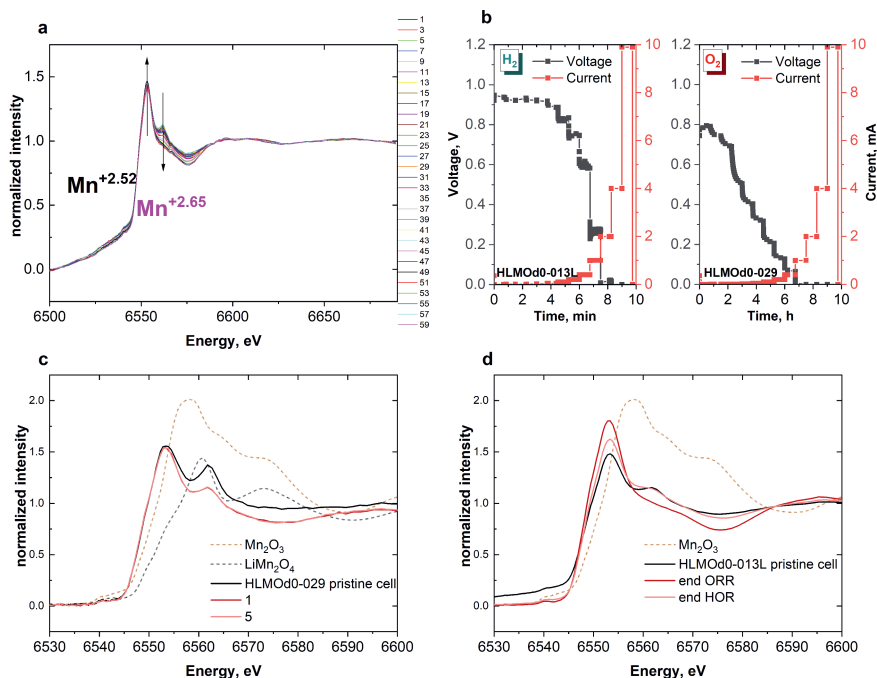


Figure 5.6: Operando x-ray absorption spectroscopy of a fresh HLMO-029 vs. Pt cell as (a) HLMO @ H₂ electrode and (c) as O₂ electrode. In (b) the I and V vs. programs followed. In (d) Structure at end of operation when the same cell (HLMO-013 vs. Pt) is used as H₂ electrode after use as O₂ electrode.

3.65+, thus confirming (de)protonation of the spinel. At ORR (de-protonation), A increases and B decreases, while at HOR (protonation) A decreases and B increases in intensity.

Extended energy ranges were scanned in order to gain information from longer distance interactions. Fourier transform of the EXAFS region is shown in figure 5.7d along with fittings using a 2-shell model as described in the methods section. Results from the fittings are shown in figure 5.8. Here, a change in coordination number (CN) of Mn (figure 5.8a) is seen upon (de-)protonation. During operation at oxygen side Mn is over-coordinated (CN >6) while during operation at hydrogen side Mn is under-coordinated (CN <6). The change in coordination with oxygen atoms can be explained by oxygen vacancy (V_o) formation/annihilation. For instance, oxygen fed to the cathode is first used to fill existing oxygen vacancies and interstices until overly coordinating Mn with 6.49 oxygen atoms in average. Oxygen vacancy filling is a known phenomenon in metal oxides, which when used as ORR electrocatalysts may delay reaction onset [55–58]. In the case of HOR, from the change in CN one could think that oxygen vacancies are formed, however, there is no change in oxidation state. In turn, this suggests that oxygen atoms

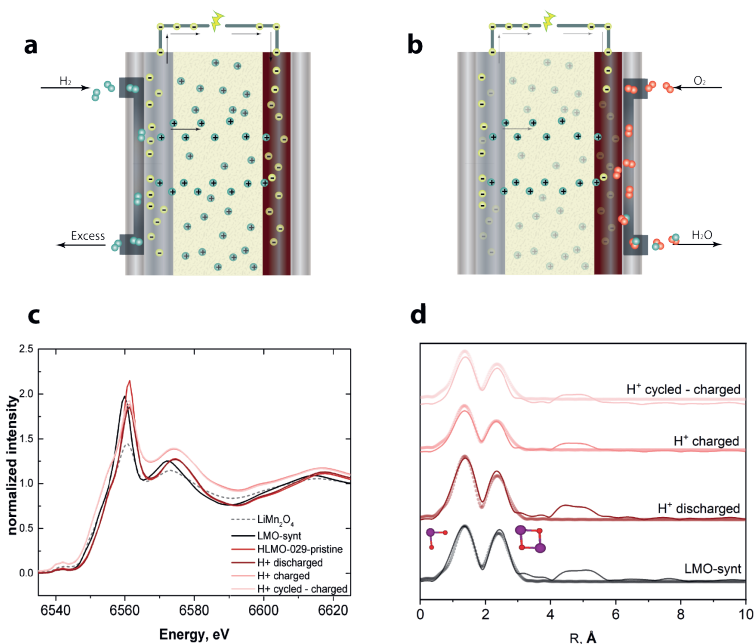


Figure 5.7: (a) Set-up for electrochemical protonation; (b) set-up for electrochemical deprotonation; (c) XANES region; (d) FT of EXAFS region and fit (transparent dots). First shell is Mn-O distance and second shell is Mn-Mn distance.

are not leaving the lattice but rather redistributing over it, so that vacancies are formed around the octahedra with Mn centre thus explaining lower CN. Furthermore, we observe structural reversibility upon proton insertion. Features like CN (figure 5.8a), oxidation state (figure 5.8b) and Mn—O bond length (figure 5.8c) appear to change accordingly with calculated proton concentration (figure 5.8d) and revert to their initial values after one (de-)protonation cycle.

These results agree well with *operando* measurements of HLMO-dis and support the hypothesis of oxygen vacancy formation/annihilation according to electrochemical reaction. Finally, we should remember that these *ex-situ* results reflect extremes of (de-)protonation whereas a real fuel cell would operate somewhere in between. Therefore, there must be optimal structural parameters, e.g. $[V_o]$, $[H^+]$ and oxidation state, that would make spinel types, cubic or tetragonal, HLMOs active for either reaction, i.e. ORR or HOR.

5.4. Discussion

5.4.1. Characterisation

We have prepared different spinel HLMOs with compositions $0.13 < Li^+ < 0.99$ that have slightly different average unit cell sizes according to their Lithium content.

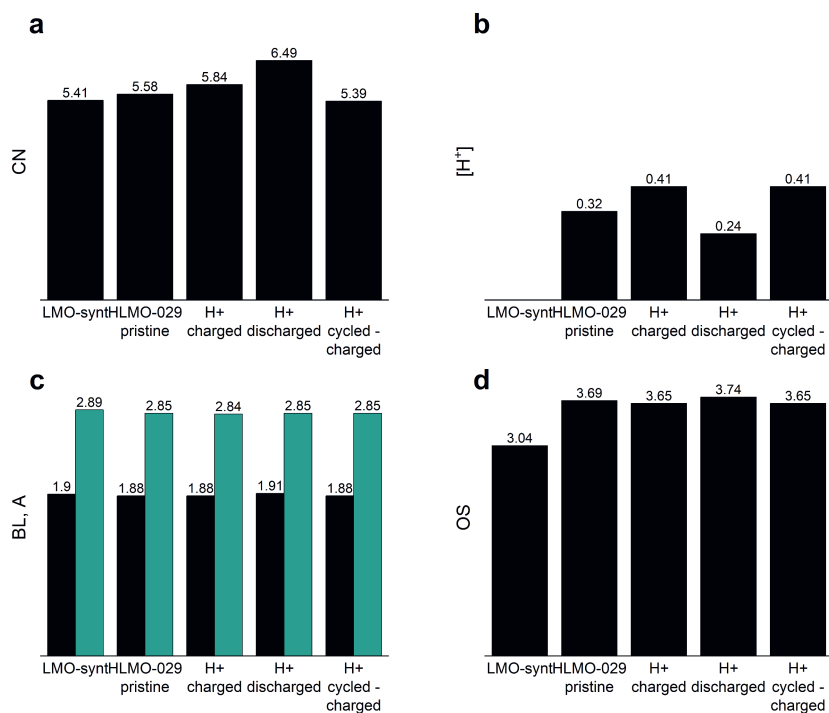


Figure 5.8: Fitting results at different stages of the process. (a) Coordination number; (b) Estimated proton content; (c) Bond length: Mn-O (black), Mn-Mn (turquoise), in Å; (d) Oxidation state .

Each of these spinel types show line broadening in x-ray diffractograms, suggesting a small distribution of crystal sizes and compositions within one single sample. Our initial cubic spinel LMO has an average oxidation state of 3.04+, meaning a weighted distribution towards Mn^{3+} states rather than Mn^{4+} . Pre-edge features agree with a cubic structure where Mn ions are in an octahedral (Oh) field with two visible oscillations, P1 and P2, whose centroids are approximately 2 eV apart. These two oscillations are characteristic of materials where there is crystal-field splitting between the t_{2g} and e_g orbitals such as where Mn^{3+} and Mn^{4+} exist together (e.g. spinel LMO), thus creating a broad pre-edge region [48, 51, 52, 59–61]. These two features can be related to excitation of core electrons (1s) to unoccupied energy levels. In the case of 3d metals, such as Mn, these transitions correspond to $1s \rightarrow 3d$ excitations, and have been related to transitions to 3d t_{2g} (P1) and 3d e_g (P2) energy levels [5, 49, 50, 52]. Studies have attributed manganese's catalytic activity to several reactions, e.g. water oxidation, to the presence of Mn^{3+} species. The ease of transfer of its unpaired e_g electron has been pinpointed as critical for active catalysts [5, 62–65]. Upon de-lithiation of LMO, we see an increase in the relative

intensity of P2 in relation to P1 and an oxidation of Mn to an overall oxidation state of 3.69+ in HLMO-029. The increase in the second pre-edge feature (P2) would then suggest an increase in density of unoccupied e_g orbitals (higher hole density of 3d states) that can be correlated to the change in average oxidation state towards higher density of Mn^{4+} , in agreement with previous work by Nam et al. [52]. Thus, our results show that even after strong de-lithiation, Mn average oxidation state is still relatively far from the expected Mn^{4+} state. When starting with standard LMO ($Mn_{3.5+}$), it is expected that most Li^+ would be leached out at this point making a material similar to λ - Mn_2O_4 (Mn^{4+}). However, from our results we see that we have made a spinel with higher Mn^{3+} concentration than standard LMO, thus upon strong de-lithiation higher amounts of Mn^{3+} remain, increasing our expectations for electrocatalytic activity.

Subjecting the resulting powders to standard methods of MEA fabrication, i.e. ink preparation with Nafion as binder and hot-pressing electrodes to make one assembly, resulted in a structural change of the material. Previous studies suggested Nafion's capability to reduce manganese oxides [46, 66]; however, we find in our studies that even though there is indeed a slight reduction upon Nafion addition, the crystal structure remains a cubic spinel. A more critical step is hot-pressing, where temperature and pressure have distorted the cubic structure into a tetragonal one. Thus, the spinel is locally distorted by the Jahn-teller effect resulting in $Mn^{3+}O_6$ octahedra with different Mn—O bond length along the z axis [50, 52, 67]. Pre-edge features confirm a tetragonal structure with only one oscillation before the edge corresponding to Mn atoms in an Oh field. At the same time, EXAFS features show a 2-shell structure at short distances, similar to that of cubic or tetragonal spinels, however at longer distances they do not agree, suggesting instead some sort of long distance disorder.

In summary, spinel-type HLMOs can be understood as a distribution of several types with slightly different crystal sizes (lattice parameter, a) and their subsequent composition as Li^+/H^+ content affects the lattice size, as well as a weighted distribution of oxidation states 2+, 3+ and 4+ depending on their cubic nature or if they have been distorted to a tetragonal form.

5.4.2. Performance

Cubic spinel types with average oxidation state $3+ < OS < 4+$ and disordered tetragonal spinel types with average oxidation state $2+ < OS < 3+$ have both been studied as HOR and ORR electrocatalysts. Both show activity to HO and OR reactions and similar trends for various structural and electronic properties have been found in both spinel families. Materials with different compositions, e.g. HLMO-029 and HLMO-013L, both showed an increase in "white line" intensity (A) and intensity of shoulder B (see figure 5.6d and figure 5.7c) when operated under air flow and reducing conditions (ORR). In 3d transition metals such as Mn, the white line intensity is related to transitions to 4p unoccupied energy levels, $1s \rightarrow 4p$. In addition, in some studies this intensity has been related to hybridization of Mn 4p orbitals with O 2p [48, 50]. The higher energy shoulder in the XANES region (B) can be related to the distance of the absorbing atom to its nearest neighbour, i.e. oxy-

gen, as oscillations past the edge happen as a result of constructive or destructive interactions with neighbouring atoms. Many authors have related this oscillation to Mn—O bond length through a direct relation (rule), although its applicability is widely debated [54]. However, DFT studies in LMO materials have found that this oscillation is indeed related to interactions with the nearest oxygen atoms [50, 68]. The intensity can also be understood as a density of states (DOS) which would suggest an increase in transitions to 4p orbitals or increased density of hybridised Mn 4p/ O 2p states.

On the other hand, we see the opposite trend when the material is operated under hydrogen flow and oxidizing conditions (HOR). In this case, the white line intensity (A) decreases while the intensity of shoulder B increases. In both materials, cubic and disordered tetragonal, we have observed reversibility of the structures associated to features A and B, by using the final structure at ORR as the initial state at the HOR side. Ex-situ cycling through (de)protonation processes has shown the same results, with both features returning to almost initial conditions even after going through 2 cycles of protonation, i.e. pristine → electrochemical protonation (HOR) → electrochemical deprotonation (ORR) → electrochemical protonation (HOR).

EXAFS analysis of (de-)protonated cubic spinel HLMO-029 verified changes in oxidation state as expected, e.g. oxidation at ORR operation, reduction at HOR, as well as it helped clarify the states in which spinel HLMOs can become active to ORR or HOR. Fittings of the EXAFS region revealed a change in Mn local environment where it evolves to an over-coordinated structure (CN>6) along with an increase in oxidation state and a decrease in proton concentration when operating at ORR. Oxygen vacancies are common defects found in metal oxides originating from synthesis and preparation methods [24, 56, 69], thus it is reasonable to think that under the right conditions, e.g. oxygen rich environment and reductive potentials, these vacancies would be filled by available oxygen atoms. As discussed previously, oxygen absorption is in fact, a property of metal oxides [55–58]. Once Mn coordination is saturated with oxygen to a state where energetics would favour oxygen reduction, Mn oxidises by losing some of its structural protons that exist as -OH groups, probably formed during chemical protonation.

On the other hand, when spinels are used as HOR electrocatalyst, EXAFS analysis reveals a decrease in Mn coordination (CN<6) along with lower oxidation state and increased proton concentration. Contrary to the previous case, Mn under-coordination here suggests formation of oxygen vacancies. MD simulations by Croy et al. on cathode materials for Li batteries such as spinel LNMO (Li-Ni-Mn-O) and layered Li₂MnO₃ showed that Li atoms migrate within the materials to interstitials where no bond with Mn is formed, i.e. bond length > 2.3 Å, and propose oxygen migration as one of the causes for Mn under-coordination. They have found that when all Li is removed, additional O vacancies are created in proportion to hole doping. This entails a similar situation as in our spinels as most Li has been removed and hole doping is happening by insertion of positive charges as protons. However, we observe no change in Mn oxidation state when operating as HOR electrocatalyst which suggest no change in overall charge in the material. This suggests O mi-

gration to neighbouring vacancies within the crystal. In spinel structures O atoms occupy the 32e sites (Wyckoff position) that correspond to the corners of octahedra with Mn centre and tetrahedra with Li⁺ centre. A decrease in CN around Mn centres would then suggest O migration to vacancies in tetrahedral corners with Li⁺ centre or interstitial Li⁺ vacancy where incoming H⁺ can accommodate and form -OH groups. Figure 5.9 shows a representation of the proposed working mechanisms based on this work.

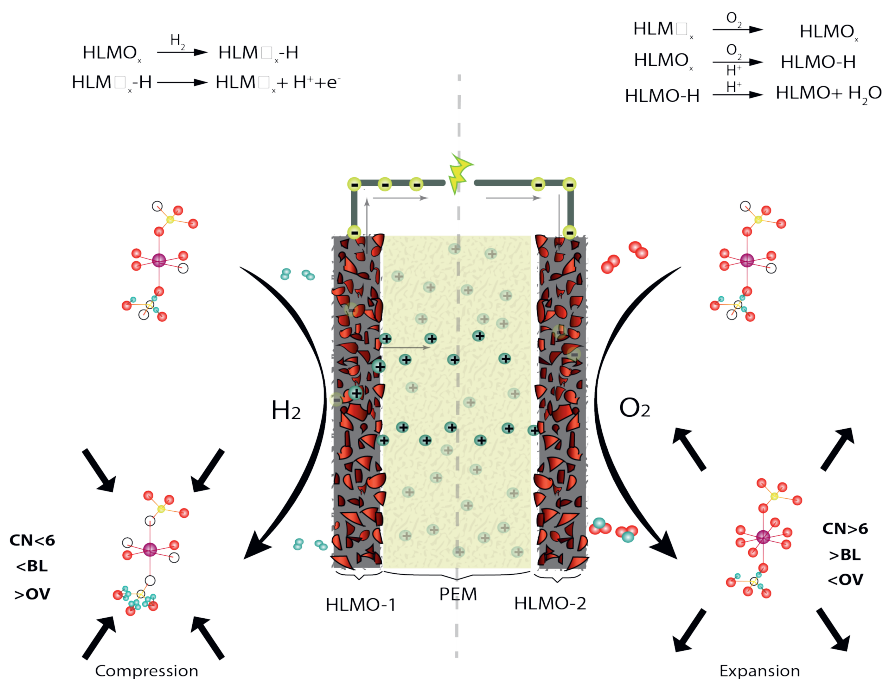


Figure 5.9: Schematic of the proposed working mechanism. CN: coordination number; BL: bond length; OV: oxygen vacancies (\square_x)

Furthermore, changes in oxidation state suggest that similar to its Platinum counterpart, ORR is the limiting process in a fuel cell with a sluggish, multi-step reaction. On the other hand, HOR seems to have faster kinetics as no change is seen in Mn energy edge during operation or in ex-situ experiments, suggesting that the rate at which positive charge is inserted equals the rate at which negative charge is lost. Along with these changes, we also observe changes in Mn—O average bond length. Results from EXAFS show that at ORR Mn—O bond length increases and it decreases at HOR conditions. This agrees with oxygen atoms overly coordinating Mn forcing the negative charges to move further away (structure stretches) or oxygen atoms migrating away thus increasing the attraction forces between Mn and remaining O atoms (structure compresses). It should be noted that our ex-situ experiments were carried under “extreme” conditions (near short-circuit current at each side), but in a real fuel cell an optimum I-V relation exists to maximize power

output, therefore an optimum combination of structural and electronic properties, e.g. CN, OS, $[H^+]$ can be achieved for maximum activity to each reaction.

Finally, it is worth highlighting the fact that our preliminary experiments done by traditional electrochemical techniques, i.e. voltammetry in liquid electrolyte, showed the expected Mn instability at pH=1 due to Mn dissolution and disproportionation as predicted in Pourbaix diagrams. In contrast, in experiments done under more realistic PEM FC conditions, e.g. solid electrolyte, Mn was found to be more stable with no significant indications of dissolution and showing promise as an alternative inexpensive electrocatalyst in acidic conditions. This result brings to attention the importance of testing materials in conditions as close as possible to their final application as theoretical predictions may shy us away from trying. To date, and to our knowledge, only a handful of studies can be found on electrocatalytic activity of transition metal oxides at pH values <7 , whereas the vast majority are concerned with its potential as electrocatalyst in alkaline environments.

5.5. Conclusions

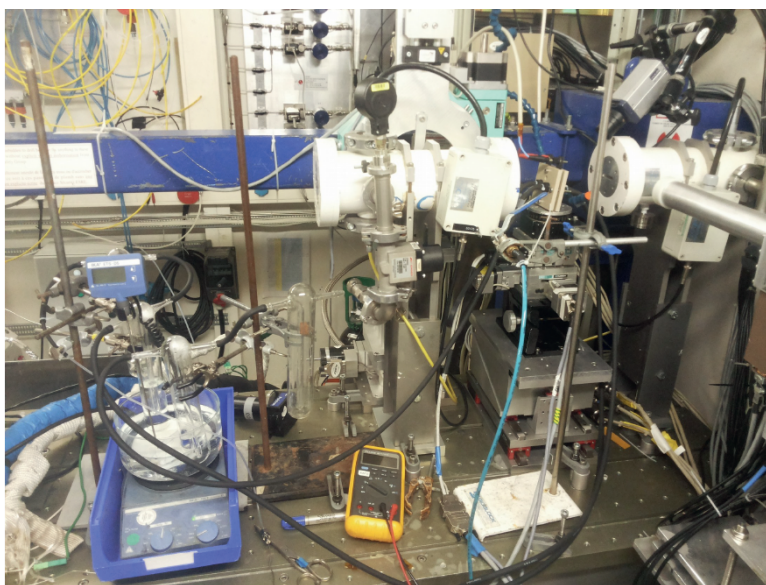
This work has shown that inexpensive materials such as lithium manganates can be used as electrocatalysts in PEM fuel cells and should provide a starting point to the directions in which it is possible to optimize and take advantage of spinel HLMO double functionality. Multivalent transition metals, such as Mn, have an inherent versatility due to their capacity to take many oxidation states that result in several different structures. This gives us the power to design material suitable for desired applications by fine-tuning structural and electronic properties. In our case, a simple treatment such as de-lithiation/protonation can make them (more) active to HO and OR reactions in acid media. Furthermore, these materials show structural reversibility which opens a window to future research on catalyst regeneration, since a simple procedure such as reverting the fuel cell can return the material to a nearly pristine state.

5.A. Fuel cell



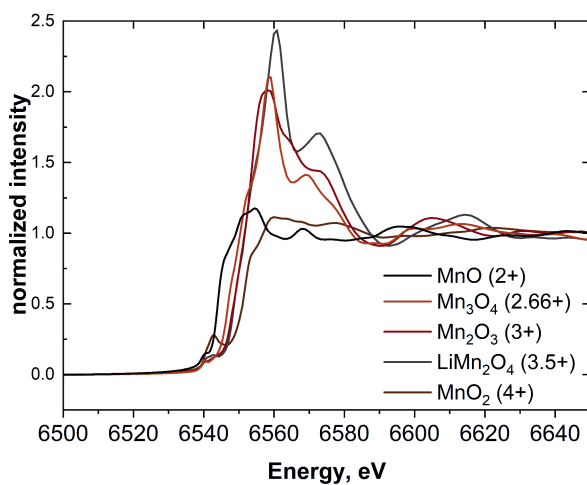
5.B. XAS set-up

5

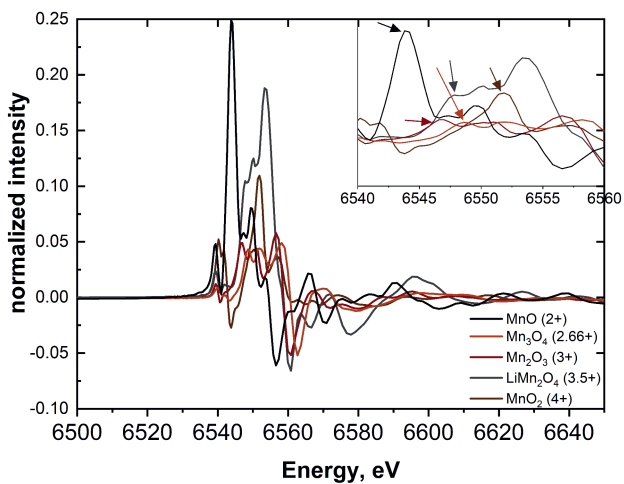


5.C. Calibration of Mn oxidation state

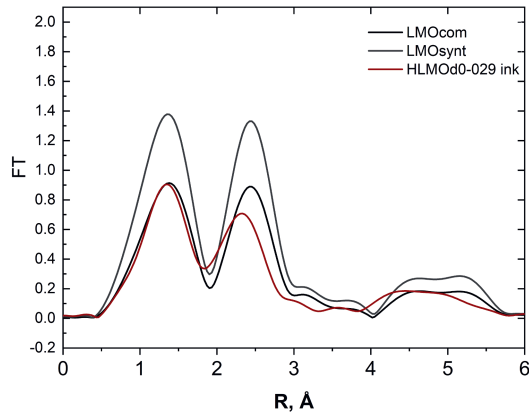
XANES of standards.



First derivative: Edge energy taken as first maximum of first derivative.



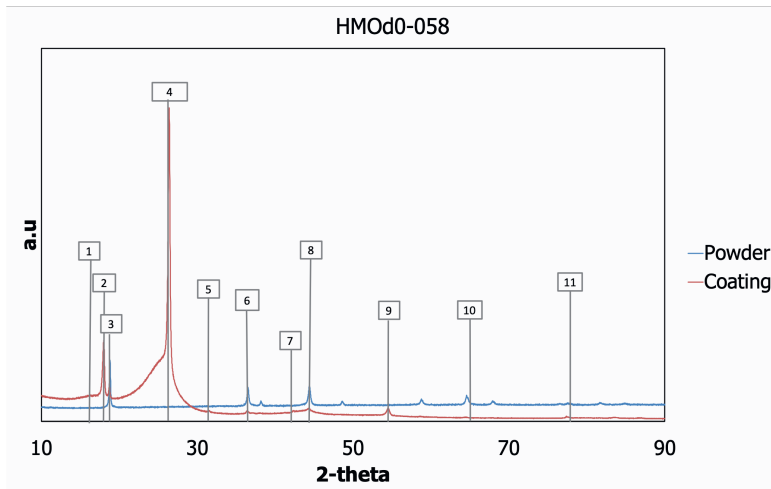
5.D. EXAFS upon Nafion addition



5

5.E. Identification of non-spinel reflections in Electrodes and MEAs

Example of an HLMOd0 sample:



Strongest reflections of likely compounds:

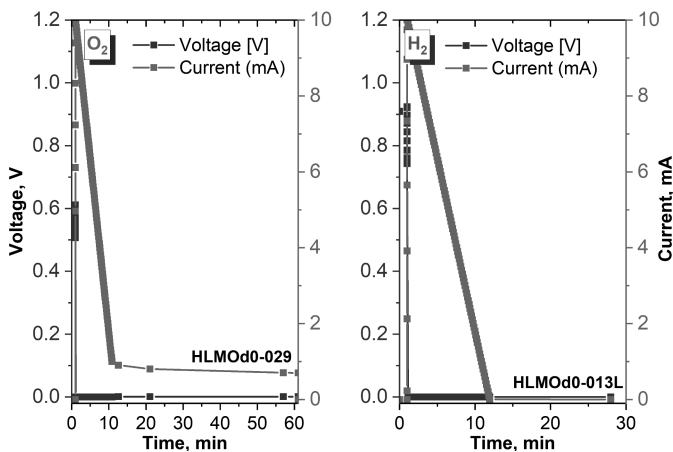
Strongest reflections	d	sin θ (rad)	θ (rad)	θ (deg)	2 θ (deg)	Compound
a	3.35E-10	0.2299403	0.23201634	13.2935569	26.5871138	C
b	2.08E-10	0.37033654	0.37937129	21.73637397	43.47274795	
c	1.96E-10	0.3930102	0.40390293	23.14193324	46.28386648	
a	4.89E-10	0.15752556	0.15818443	9.063300084	18.12660017	Mn ₅ O ₈
b	2.81E-10	0.27412811	0.27768297	15.91006219	31.82012438	
c	2.35E-10	0.32778723	0.33396045	19.13452451	38.26904903	
a	4.92E-10	0.15656504	0.15721184	9.007574768	18.01514954	MnSO ₄ ·7H ₂ O
b	5.49E-10	0.14030965	0.14077416	8.065764975	16.13152995	
c	4.88E-10	0.15784836	0.15851132	9.082029383	18.16405877	
a	4.83E-10	0.1594824	0.16016632	9.176854249	18.3537085	Li ₂ Mn ₂ O ₄
b	2.43E-10	0.31699588	0.32256033	18.48134566	36.96269133	
c	2.00E-10	0.38515	0.39537036	22.65305276	45.30610552	
a	4.76E-10	0.16182773	0.16254252	9.313000214	18.62600043	LiMn ₂ O ₄
b	2.49E-10	0.30935743	0.31451724	18.0205105	36.041021	
c	2.06E-10	0.37393204	0.38324501	21.95832169	43.91664338	

Phase identification:

Peak	2 θ	2 θ (rad)	θ	sin θ	sin ² θ	d(hkl)	ID
1	16.51	0.288154	0.144077	0.1436	0.0206	5.36499E-10	MnSO ₄ ·7H ₂ O
2	18.02	0.314508	0.157254	0.1566	0.0245	4.91869E-10	MnSO ₄ ·7H ₂ O/Mn ₅ O ₈ /Li ₂ Mn ₂ O ₄ /LiMn ₂ O ₄
3	18.7	0.326377	0.163188	0.1625	0.0264	4.74133E-10	Spinel LMO
4	26.37	0.460243	0.230122	0.2281	0.0520	3.37709E-10	Graphite
5	31.88	0.556411	0.278205	0.2746	0.0754	2.80486E-10	Mn ₅ O ₈
6	36.48	0.636696	0.318348	0.3130	0.0980	2.46104E-10	LiMn ₂ O ₄
7	42.12	0.735133	0.367566	0.3593	0.1291	2.14362E-10	Graphite
8	44.4	0.774926	0.387463	0.3778	0.1428	2.03869E-10	Graphite/Spinel LMO
9	54.59	0.952775	0.476388	0.4586	0.2103	1.67978E-10	Unknown
10	65.07	1.135686	0.567843	0.5378	0.2892	1.43228E-10	Spinel LMO
11	77.46	1.351932	0.675966	0.6257	0.3914	1.2312E-10	Spinel LMO

5.F. FC under constant voltage conditions

HLMOd0-029 and HLMOd0-013L vs. Pt fuel cell using a constant voltage program to approximate to near short-circuit conditions.



References

- [1] J. P. Brenet, "Electrochemical behaviour of metallic oxides," *Journal of Power Sources*, vol. 4, no. 3, pp. 183–190, 1979.
- [2] Y. Gorlin and T. F. Jaramillo, "Investigation of surface oxidation processes on manganese oxide electrocatalysts using electrochemical methods and ex situ X-ray photoelectron spectroscopy," *Journal of the Electrochemical Society*, vol. 159, no. 10, pp. 782–786, 2012.
- [3] F. H. Lima, M. L. Calegario, and E. A. Ticianelli, "Investigations of the catalytic properties of manganese oxides for the oxygen reduction reaction in alkaline media," *Journal of Electroanalytical Chemistry*, vol. 590, no. 2, pp. 152–160, 2006.
- [4] Z. Xia, L. An, P. Chen, and D. Xia, "Non-Pt Nanostructured Catalysts for Oxygen Reduction Reaction: Synthesis, Catalytic Activity and its Key Factors," *Advanced Energy Materials*, vol. 6, no. 17, pp. 1–29, 2016.
- [5] C. Wei, Z. Feng, G. G. Scherer, J. Barber, Y. Shao-Horn, and Z. J. Xu, "Cations in Octahedral Sites: A Descriptor for Oxygen Electrocatalysis on Transition-Metal Spinels," *Advanced Materials*, vol. 29, no. 23, pp. 1–8, 2017.
- [6] C. Goswami, K. K. Hazarika, and P. Bharali, "Transition metal oxide nanocatalysts for oxygen reduction reaction," *Materials Science for Energy Technologies*, vol. 1, no. 2, pp. 117–128, 2018.
- [7] K. K. Hazarika, C. Goswami, H. Saikia, B. J. Borah, and P. Bharali, "Cubic Mn₂O₃ nanoparticles on carbon as bifunctional electrocatalyst for oxygen reduction and oxygen evolution reactions," *Molecular Catalysis*, vol. 451, pp. 153–160, 2018.
- [8] A. Harriman, I. J. Pickering, J. M. Thomas, and P. A. Christensen, "Metal oxides as heterogeneous catalysts for oxygen evolution under photochemical conditions," *Journal of the Chemical Society, Faraday Transactions 1: Physical Chemistry in Condensed Phases*, vol. 84, no. 8, pp. 2795–2806, 1988.
- [9] I. Zaharieva, P. Chernev, M. Risch, K. Klingan, M. Kohlhoff, A. Fischer, and H. Dau, "Electrosynthesis, functional, and structural characterization of a water-oxidizing manganese oxide," *Energy and Environmental Science*, vol. 5, no. 5, pp. 7081–7089, 2012.
- [10] Y. Nie, L. Li, and Z. Wei, "Recent advancements in Pt and Pt-free catalysts for oxygen reduction reaction," *Chemical Society Reviews*, vol. 44, no. 8, pp. 2168–2201, 2015.
- [11] C. Ottone, M. Armandi, S. Hernández, S. Bensaid, M. Fontana, C. F. Pirri, G. Saracco, E. Garrone, and B. Bonelli, "Effect of surface area on the rate of photocatalytic water oxidation as promoted by different manganese oxides," *Chemical Engineering Journal*, vol. 278, pp. 36–45, 2015.

- [12] S. K. Ghosh and H. Rahaman, *Noble Metal–Manganese Oxide Hybrid Nanocatalysts*. Elsevier Inc., 2019.
- [13] K. A. Stoerzinger, M. Risch, B. Han, and Y. Shao-Horn, "Recent Insights into Manganese Oxides in Catalyzing Oxygen Reduction Kinetics," *ACS Catalysis*, vol. 5, no. 10, pp. 6021–6031, 2015.
- [14] I. M. Mosa, S. Biswas, A. M. El-Sawy, V. Botu, C. Guild, W. Song, R. Ramprasad, J. F. Rusling, and S. L. Suib, "Tunable mesoporous manganese oxide for high performance oxygen reduction and evolution reactions," *Journal of Materials Chemistry A*, vol. 4, no. 2, pp. 620–631, 2015.
- [15] I. Roche, E. Chaînet, M. Chatenet, and J. Vondrák, "Carbon-supported manganese oxide nanoparticles as electrocatalysts for the Oxygen Reduction Reaction (ORR) in alkaline medium: Physical characterizations and ORR mechanism," *Journal of Physical Chemistry C*, vol. 111, no. 3, pp. 1434–1443, 2007.
- [16] J. Vondrák, B. Klápště, J. Velická, M. Sedlaříková, V. Novák, and J. Reiter, "Carbon/manganese oxide based fuel cell electrocatalyst using "flywheel" principle," *Journal of New Materials for Electrochemical Systems*, vol. 8, no. 1, pp. 1–4, 2005.
- [17] A. Flegler, S. Hartmann, H. Weinrich, M. Kapuschinski, J. Settelein, H. Lormann, and G. Sextl, "Manganese Oxide Coated Carbon Materials as Hybrid Catalysts for the Application in Primary Aqueous Metal-Air Batteries," *C*, vol. 2, no. 1, p. 4, 2016.
- [18] J. Venkata Swetha, H. Parse, B. Kakade, and A. Geetha, "Morphology dependent facile synthesis of manganese oxide nanostructures for oxygen reduction reaction," *Solid State Ionics*, vol. 328, no. August, pp. 1–7, 2018.
- [19] Y. Dessie, S. Tadesse, R. Eswaramoorthy, and B. Abebe, "Recent developments in manganese oxide based nanomaterials with oxygen reduction reaction functionalities for energy conversion and storage applications: A review," *Journal of Science: Advanced Materials and Devices*, vol. 4, no. 3, pp. 353–369, 2019.
- [20] I. Roche and K. Scott, "Carbon-supported manganese oxide nanoparticles as electrocatalysts for oxygen reduction reaction (orr) in neutral solution," *Journal of Applied Electrochemistry*, vol. 39, no. 2, pp. 197–204, 2009.
- [21] H. Antoni, D. M. Morales, Q. Fu, Y. T. Chen, J. Masa, W. Schuhmann, and M. Muhler, "Oxidative Deposition of Manganese Oxide Nanosheets on Nitrogen-Functionalized Carbon Nanotubes Applied in the Alkaline Oxygen Evolution Reaction," *ACS Omega*, vol. 3, no. 9, pp. 11216–11226, 2018.
- [22] T. Hayashi, N. Bonnet-Mercier, A. Yamaguchi, K. Suetsugu, and R. Nakamura, "Electrochemical characterization of manganese oxides as a water oxidation catalyst in proton exchange membrane electrolyzers," *Royal Society Open Science*, vol. 6, no. 5, 2019.

- [23] M. Huynh, D. K. Bediako, and D. G. Nocera, "A functionally stable manganese oxide oxygen evolution catalyst in acid," *Journal of the American Chemical Society*, vol. 136, no. 16, pp. 6002–6010, 2014.
- [24] G. R. Mirshekari and A. P. Shirvanian, "Electrochemical behavior of titanium oxide nanoparticles for oxygen reduction reaction environment in PEM fuel cells," *Materials Today Energy*, vol. 9, no. 8, pp. 235–239, 2018.
- [25] M. Pourbaix, *Thermodynamique des solutions aqueuses diluées. Représentation graphique du rôle du pH et du potentiel*. 1945.
- [26] R. Frydendal, E. A. Paoli, I. Chorkendorff, J. Rossmeisl, and I. E. Stephens, "Toward an Active and Stable Catalyst for Oxygen Evolution in Acidic Media: Ti-Stabilized MnO₂," *Advanced Energy Materials*, vol. 5, no. 22, 2015.
- [27] P. P. Patel, M. K. Datta, O. I. Velikokhatnyi, R. Kuruba, K. Damodaran, P. Jampani, B. Gattu, P. M. Shanthi, S. S. Damle, and P. N. Kumta, "Noble metal-free bifunctional oxygen evolution and oxygen reduction acidic media electrocatalysts," *Scientific Reports*, vol. 6, no. February, pp. 1–14, 2016.
- [28] F. Cheng, J. Shen, B. Peng, Y. Pan, Z. Tao, and J. Chen, "Rapid room-temperature synthesis of nanocrystalline spinels as oxygen reduction and evolution electrocatalysts," *Nature Chemistry*, vol. 3, no. 1, pp. 79–84, 2011.
- [29] M. Risch, K. A. Stoerzinger, B. Han, T. Z. Regier, D. Peak, S. Y. Sayed, C. Wei, Z. Xu, and Y. Shao-Horn, "Redox Processes of Manganese Oxide in Catalyzing Oxygen Evolution and Reduction: An in Situ Soft X-ray Absorption Spectroscopy Study," *Journal of Physical Chemistry C*, vol. 121, no. 33, pp. 17682–17692, 2017.
- [30] P. Aitchison, B. Ammundsen, D. J. Jones, G. Burns, and J. Rozière, "Cobalt substitution in lithium manganate spinels: Examination of local structure and lithium extraction by XAFS," *Journal of Materials Chemistry*, vol. 9, no. 12, pp. 3125–3130, 1999.
- [31] X. Yang, H. Kanoh, W. Tang, and K. Ooi, "Synthesis of Li(1.33)Mn(1.67)O₄ spinels with different morphologies and their ion adsorptivities after delithiation," *Journal of Materials Chemistry*, vol. 10, no. 8, pp. 1903–1909, 2000.
- [32] S. Y. Sun, X. Song, Q. H. Zhang, J. Wang, and J. G. Yu, "Lithium extraction/insertion process on cubic Li-Mn-O precursors with different Li/Mn ratio and morphology," *Adsorption*, vol. 17, no. 5, pp. 881–887, 2011.
- [33] J. Wang, Y. Liu, H. Zhang, Y. Li, H. Bai, W. Wu, Z. Li, and X. Zhang, "Embedding sulfonated lithium ion-sieves into polyelectrolyte membrane to construct efficient proton conduction pathways," *Journal of Membrane Science*, vol. 501, pp. 109–122, 2016.

- [34] K. Sato, Y. Inoue, S. Yasukawa, and H. Takahashi, "The surface structure formed by H₂ desorption from proton-exchanged HyLi_{1-(x+y)}Mn₂O₄ and its catalytic activity for oxidation of methane and butane," *Applied Surface Science*, vol. 65-66, no. C, pp. 308–312, 1993.
- [35] D. M. Robinson, Y. B. Go, M. Greenblatt, and G. C. Dismukes, "Water Oxidation by λ -MnO₂: Catalysis by the Cubical Mn₄O₄ Subcluster Obtained by Delithiation of Spinel LiMn₂O₄," *Journal of the American Chemical Society*, vol. 132, no. 33, pp. 11467–11469, 2010.
- [36] K. Ooi, Y. Miyai, S. Katoh, H. Maeda, and M. Abe, "Analysis of pH Titration Data in a λ -MnO₂ + LiOH System on the Basis of Redox Mechanism," *Langmuir*, vol. 6, no. 1, pp. 289–291, 1990.
- [37] K. Ooi, Y. Miyai, and J. Sakakihara, "Mechanism of Li Insertion in Spinel-Type Manganese Oxide. Redox and Ion-Exchange Reactions," *Langmuir*, vol. 7, no. 6, pp. 1167–1171, 1991.
- [38] Q. Feng, Y. Miyai, H. Kanoh, and K. Ooi, "Li⁺ Extraction/Insertion with Spinel-Type Lithium Manganese Oxides. Characterization of Redox-Type and Ion-Exchange-Type Sites," *Langmuir*, vol. 8, no. 7, pp. 1861–1867, 1992.
- [39] B. Ammundsen, D. J. Jones, J. Rozière, and G. R. Burns, "Mechanism of Proton Insertion and Characterization of the Proton Sites in Lithium Manganate Spinels," *Chemistry of Materials*, vol. 7, no. 11, pp. 2151–2160, 1995.
- [40] Z. Y. Ji, M. Y. Zhao, J. S. Yuan, J. Wang, J. Q. Zhou, H. B. Yin, and B. Y. Sun, "Li⁺ Extraction from Spinel-Type LiMn₂O₄ in Different Eluents and Li⁺ Insertion in the Aqueous Phase," *Solvent Extraction and Ion Exchange*, vol. 34, no. 6, pp. 549–557, 2016.
- [41] J. C. Hunter, "Preparation of a new crystal form of manganese dioxide: λ -MnO₂," *Journal of Solid State Chemistry*, vol. 39, no. 2, pp. 142–147, 1981.
- [42] B. Ammundsen, D. J. Jones, J. Rozière, and G. R. Burns, "Effect of chemical extraction of lithium on the local structure of spinel lithium manganese oxides determined by X-ray absorption spectroscopy," *Chemistry of Materials*, vol. 8, no. 12, pp. 2799–2808, 1996.
- [43] B. Ammundsen, D. J. Jones, and J. Rozière, "X-Ray Absorption Fine Structure Spectroscopy as a Probe of Local Structure in Lithium Manganese Oxides," *Journal of Solid State Chemistry*, vol. 141, no. 1, pp. 294–297, 1998.
- [44] A. Siebel, Y. Gorlin, J. Durst, O. Proux, F. Hasché, M. Tromp, and H. A. Gasteiger, "Identification of Catalyst Structure during the Hydrogen Oxidation Reaction in an Operating PEM Fuel Cell," *ACS Catalysis*, vol. 6, no. 11, pp. 7326–7334, 2016.

- [45] K. Momma and F. Izumi, "VESTA 3 for three-dimensional visualization of crystal, volumetric and morphology data," *Journal of Applied Crystallography*, vol. 44, pp. 1272–1276, dec 2011.
- [46] R. K. Hocking, R. Brimblecombe, L. Y. Chang, A. Singh, M. H. Cheah, C. Glover, W. H. Casey, and L. Spiccia, "Water-oxidation catalysis by manganese in a geochemical-like cycle," *Nature Chemistry*, vol. 3, no. 6, pp. 461–466, 2011.
- [47] U. Leiden and R. M. Prof, *A comparative study of platinum nanodeposits on surfaces by STM and AFM after heat treatment PROEFCHRIFT door Roman Tsybukh in 1975 Promotiecommissie*. No. september, 2010.
- [48] F. De Groot, "High-resolution X-ray emission and X-ray absorption spectroscopy," *Chemical Reviews*, vol. 101, no. 6, pp. 1779–1808, 2001.
- [49] P. Wernet, "Chemical interactions and dynamics with femtosecond X-ray spectroscopy and the role of X-ray free-electron lasers," *Philosophical Transactions of the Royal Society A: Mathematical, Physical and Engineering Sciences*, vol. 377, no. 2145, 2019.
- [50] T. Okumura, Y. Yamaguchi, M. Shikano, and H. Kobayashi, "Further findings of X-ray absorption near-edge structure in lithium manganese spinel oxide using first-principles calculations," *Journal of Materials Chemistry A*, vol. 2, no. 21, pp. 8017–8025, 2014.
- [51] V. Cuartero, S. Lafuerza, M. Rovezzi, J. García, J. Blasco, G. Subías, and E. Jiménez, "X-ray absorption and emission spectroscopy study of Mn and Co valence and spin states in $TbMn_{1-x}Co_xO_3$," *Physical Review B*, vol. 94, no. 15, pp. 1–10, 2016.
- [52] K. W. Nam, M. G. Kim, and K. B. Kim, "In situ Mn K-edge X-ray absorption spectroscopy studies of electrodeposited manganese oxide films for electrochemical capacitors," *Journal of Physical Chemistry C*, vol. 111, no. 2, pp. 749–758, 2007.
- [53] G. J. McIntosh and A. Chan, "Probing hydrogen bonding interactions and impurity intercalation in gibbsite using experimental and theoretical XANES spectroscopy," *Physical Chemistry Chemical Physics*, vol. 20, no. 37, pp. 24033–24044, 2018.
- [54] N. Horsfall, "Part 2," *Virgil, "Aeneid" 6*, 2013.
- [55] "Ruiz_17.pdf."
- [56] P. H. Rana and P. A. Parikh, "Role of oxygen storage/supply capacity of mixed oxides of Ce and Zr in ethanol oxidation," *Chemical Engineering Research and Design*, vol. 137, pp. 478–487, 2018.
- [57] "Schalow_05.pdf."

- [58] L. André, S. Abanades, and L. Cassayre, "Mixed metal oxide systems applied to thermochemical storage of solar energy: Benefits of secondary metal addition in Co and Mn oxides and contribution of thermodynamics," *Applied Sciences (Switzerland)*, vol. 8, no. 12, 2018.
- [59] D. C. Radu, P. Glatzel, W. M. Heijboer, J. H. Bitter, B. M. Weckhuysen, and F. M. de Groot, *Mn and Fe Ions and Oxo clusters in ZSM-5: Pushing the limits of X-ray Spectroscopy*, vol. 170. Elsevier B.V., 2007.
- [60] M. Sikora, C. Kapusta, K. Knížek, Z. Jiráček, C. Autret, M. Borowiec, C. J. Oates, V. Procházka, D. Rybicki, and D. Zajac, "X-ray absorption near-edge spectroscopy study of Mn and Co valence states in $\text{LaMn}_{1-x}\text{Co}_x\text{O}_3$ ($x=0-1$)," *Physical Review B - Condensed Matter and Materials Physics*, vol. 73, no. 9, pp. 1–5, 2006.
- [61] V. Cuartero, S. Lafuerza, M. Rovezzi, J. García, J. Blasco, G. Subías, and E. Jiménez, "X-ray absorption and emission spectroscopy study of Mn and Co valence and spin states in $\text{TbMn}_{1-x}\text{Co}_x\text{O}_3$," *Physical Review B*, vol. 94, no. 15, 2016.
- [62] J. Ma, C. Wang, and H. He, "Transition metal doped cryptomelane-type manganese oxide catalysts for ozone decomposition," *Applied Catalysis B: Environmental*, vol. 201, pp. 503–510, 2017.
- [63] U. Maitra, A. Govindaraj, and C. N. Rao, "Importance of trivalency and the eg 1 configuration in the photocatalytic oxidation of water by mn and co oxides," *Proceedings of the National Academy of Sciences of the United States of America*, vol. 110, no. 29, pp. 11704–11707, 2013.
- [64] S. Park, Y. H. Lee, S. Choi, H. Seo, M. Y. Lee, M. Balamurugan, and K. T. Nam, "Manganese oxide-based heterogeneous electrocatalysts for water oxidation," *Energy and Environmental Science*, vol. 13, no. 8, pp. 2310–2340, 2020.
- [65] C. H. Van Oversteeg, H. Q. Doan, F. M. De Groot, and T. Cuk, "In situ X-ray absorption spectroscopy of transition metal based water oxidation catalysts," *Chemical Society Reviews*, vol. 46, no. 1, pp. 102–125, 2017.
- [66] Y. Wei, K. B. Kim, G. Chen, and C. W. Park, "Characterizations on the microstructures of LiMn_2O_4 prepared by a simple soft-chemical technique," *Materials Characterization*, vol. 59, no. 9, pp. 1196–1200, 2008.
- [67] M. C. Kemei, J. K. Harada, R. Seshadri, and M. R. Suchomel, "Structural change and phase coexistence upon magnetic ordering in the magnetodielectric spinel Mn_3O_4 ," *Physical Review B - Condensed Matter and Materials Physics*, vol. 90, no. 6, 2014.
- [68] B. Gilbert, B. H. Frazer, A. Belz, P. G. Conrad, K. H. Neilson, D. Haskel, J. C. Lang, G. Srajer, and G. De Stasio, "Multiple scattering calculations of bonding and X-ray absorption spectroscopy of manganese oxides," *Journal of Physical Chemistry A*, vol. 107, no. 16, pp. 2839–2847, 2003.

- [69] G. M. Nolis, A. Adil, H. D. Yoo, L. Hu, R. D. Bayliss, S. H. Lapidus, L. Berkland, P. J. Phillips, J. W. Freeland, C. Kim, R. F. Klie, and J. Cabana, "Electrochemical Reduction of a Spinel-Type Manganese Oxide Cathode in Aqueous Electrolytes with Ca^{2+} or Zn^{2+} ," *Journal of Physical Chemistry C*, vol. 122, no. 8, pp. 4182–4188, 2018.

Acknowledgements

Darwin once said in his Origin Of Species: *"...those who learned to collaborate and improvise more efficiently have prevailed."* And I think this holds true as we go through life as well.

As with any other aspect of life, this piece of work would not have been possible without the incidental appearance of so many wonderful people throughout my life.

First, I would like to thank my three promotors. Mine was an exceptional and lucky position as being part of two research groups gave me more opportunities than I could otherwise have had. Even though that could represent some challenges, it also came with a lot of advantages. I had the opportunity to hear three points of view from different backgrounds in scientific discussions that helped me broaden my own views in many ways. It meant access to more tools, techniques and people that would help me grow in different directions. It also meant juggling what at times felt like a lot, but all the same, it meant that I had three times more the support that one would normally have. And for that I am very grateful.

Stephen, you were my first promotor, and though we met a little later in my project, your enthusiasm to try different things immediately got me excited. Thank you for all your support, enthusiasm, your scientific jokes that never let a meeting be boring, and thank you for your availability, even on weekends, when something was exciting or necessary. From you I see that when one's job is a hobby, it is never work. **Erik**, thank you for giving me the opportunity to do this PhD together with Ger. Your good energy and talking to you about "cool experiments" always left me motivated to work. At the same time, chats with you about life always lightened the mood. Thank you for your support all these years, and for giving me the chance to keep working with you. **Ger**, you were the first person I met in this project and I knew then that I wanted to work with you on it. Thank you for giving me the opportunity to take this position and be part of our small and cozy energy subgroup. You were my main supervisor and have supported me all these years in the good and bad moments for both. Not even sickness was an obstacle for you to show up for me and guide me. You have supported me, cheered me up, gently told me off when I needed it, and for all these things I am deeply grateful. Thank you for keeping me motivated when times got hard. I enjoyed trips to schools and conferences with you a lot, as much as dinners and the occasional drink with you and Carla. Thank you for the warm environment you created. You have been a great supervisor.

Finally, from all of you I have seen and learned what doing scientific research for fun is.

I was lucky to receive scientific support not only from supervisors, but also from others that even though not in my immediate team, contributed as much to this research and my growth. **Marnix**, even though you were not my supervisor, you guided me and supported me when I needed it. I remember the first time I talked to you about my project, and that same day you had already arranged the neutron diffraction measurements that would become a very important part of this thesis. Thank you for your initiative, your enthusiasm, your support and for your honest interest in seeing us learn and grow. **Swapna**, thank you for all your guidance and help, not only with the difficult NMR measurements that I insisted on continuing and you patiently helped me through, but also for your guidance through a PhD life. I am very grateful to both of you for having me feel part of the battery family. **Fokko**, for a while you were also part of my supervisors team, and I appreciate the contributions you made to this project during that time. You were my introduction to material science and electrochemistry since the times of my master thesis. And since then there was hardly a conversation with you that did not make me think of something new. Thank you for always inviting me to think further.

5

Research could not be possible without all the supporting staff that are always there to help when needed. **Ben**, thank you for your disposition to help always with the XRD and for your good energy. **Duco**, thank you for your help, not only with the SEM but also with our electrochemistry lab, having your support was a turning point. **Bart**, thank you for your assistance with all the LabVIEW programs, you always had time and patience when I had a request; and an orange and a smile. **Marcel**, your big smile and good mood were contagious, lightening the mood at lunch and coffee breaks. Thanks for your help on surface roughness measurements. **Lars**, thank you for your help in the chemistry and electrochemistry lab, more than once you got me unstuck. **Xiaohui**, thank you for your help with the 2D-XRD, you were always willing to help us find a way. **Veby**, you have helped me with multiple issues along the years, thank you for always doing it promptly and so kindly. In the **SEE** labs, **Frans** and **Michel**, thank you for your guidance and help whenever I needed something from your labs. You always welcomed and helped me with a big smile. **Kees** and **Michel** (Thijs), thank you for your help with neutron diffraction measurements. **Baukje**, thank you for your help with ICP-OES measurements. **Ilse** and **Nicole**, thanks for helping me figure out many administrative issues and for doing it so kindly and promptly.

Furthermore, I would like to thank those who have collaborated in some way in this project. **Marcus**, thank you for helping us with X-ray absorption measurements at the synchrotron in Grenoble. Even though it was a three-day time slot that we had, your job did not finish there. Thank you for always being willing to help me analyse the data and for the mini workshop in Athena and Artemis. No matter how long it had been, you always had time to help me. **Jure**, thank you for assisting us with the water sorption measurements and later for getting me started with the analysis. You were always willing to help. Thank you for your good vibe in the lab, it was always fun to talk to you.

I would also like to thank the master students I had the opportunity to work with, and whose hard work contributed knowledge and results to this thesis. **Da-
vide**, you were my first student and we were both learning about fuel cells as we went. I am happy that you stayed here and wish you all the best with your own PhD. **Harish**, also my first student at the same time but in Erik's side at the old ChemE building. Thank you for your help with the sPEEK synthesis during those lonely days after everyone had moved out of the old building. **Marianne**, your contribution to this work has been very valuable. Thank you for your help with the synthesis of materials, we had a nice opportunity to go measure our samples at the synchrotron in Grenoble, not without a nice stop to go around Lyon first. It was a pleasure working with you. **Dhruva**, thank you for your help with water sorption measurements. You were always very excited to try new things in the lab and make them work. **Michele**, thank you for assisting with RDE measurements. And **Tyas**, thank you for your help with synthesis work and RDE measurements. you were always curious and willing to find answers. And to all the other students, bachelors in their final projects and those from lab courses, I always learned something from our adventures together.

To the **ASM** people: **Matija**, your good mood and lively spirit always made you very fun to be around. Our Friday ASM borrels turned to parties with **Tomasz**, **Qian** and **Meng** were a lot of fun. You were the first friends I made in ASM and those were joyful times that I shall remember with pleasure. **Serhii**, your calmness was contagious and you always had something insightful to say, thank you for that. **Vasu**, I shall remember your good vibes. **Jos**, thank you for lightening up lunches and coffee breaks and for the small chats in Spanish. **Bowen**, wish you all the best with your postdoc in US. **Fanny**, thank you for introducing us to the survival run, that was a lot of fun! **Susan**, thank you for your kind smile always. **Michelle**, thank you for all the talks, laughs, your sweetness and your kindness, I wish you all the best with your new challenge in the medical sciences. **Cancel**, your big smile and energy were contagious. **Elmira**, I shall remember your softness and kindness, it was always a pleasure to talk and share with you, all the best with finishing your project. **Suellen**, it was fun to have you as my fumehood neighbour even if for a short time, it was always a pleasure to talk to you, wish you all the best with finishing. **Yu**, you have been a fun office mate, thank you the sweets and the chats. **Jianen**, you were also a fun desk neighbour, thank you for the fun chats and for turning on my PC so many times! **Hendrick**, it was a lot of fun to have you around, you always had a joke or something thoughtful to say, thanks for all the great chats and time. To my office mates that ended up becoming very good friends: **Qian**, you were my long time desk neighbour, which brought us together to Friday borrel/parties, many Chinese and some Colombian dinners, birthdays and cups of tea... or warm water. You made long hours at the office more fun as well as outside the office. All the best as prof. Liu and with baby Yi. **Tomasz**, our adventures started with playing together bass and guitar on week evenings, to eventually forming "Some Noise" with **Steffen** and **Audrey** which would never perform for a public but would turn into a fun Sunday afternoon ritual. Our adventures took us

hiking in the heat of summer, kayaking, and playing volleyball or any other game in summer evenings. Your willingness to try everything is something I already miss. Thank you for all of that. **Emma**, you were my office mate and my only group mate. You helped me a lot when I was new and inexperienced and your kindness of heart made it very easy to bond with you. I miss our coffee rituals talking about many aspects of life. Having you around has been a warming experience and also a very fun one when we had the opportunity to play and jump together with Alice and Maya. And to all others, **Kai, Yiming, Yongjun, Guotai, Peggy, Tobias, Irene, Reese, Mariano**, thanks for the talks, laughs and moments shared together. Thanks to all the **MECS** passing-by'ers of office D2.290, **Robin, Giorgio, Martin, Davide and Audrey**, there was a time when we were all relatively new, which made those lighter times and office D2.290 an office full of joy. Even as you moved out, the fun activities continued with volleyball games and dinners at the sport centre. Also thanks to other MECS members, **Anirud**, also part of those summer activities. **Fahime**, for the fun parties. **Steffen**, thank you for all the good times, from playing music together on Sunday afternoons, to long hours of figuring and counting frets to transpose a song, to volleyball evenings, group dinners and so on, those are all good memories I take with me. And **Audrey**, who has been many things along the years: office mate, band mate, sports mate and flatmate. But most of all, one of the best friends I have made during my PhD time. You were a support and a cheerleader in hard times, and you were there to celebrate in the good ones too. I have learned so much from you, from electrochemistry to films to take it easy when it is wise to do so. Thank you for your kindness, your calmness and the stimulating discussions. Thank you for your friendship.

To the **SEE** people: **Peter-Paul, Thomas, Violetta**, my first contacts with the group through the ADEM projects. The ADEM meetings turned out to be an annual excuse to go partying in The Hague. Thank you for the good times and for encouraging me to spend more time with the battery group, that was a big help for this project. **Alex**, thank you for your good energy, your smile and your willingness to collaborate, I hope we calculate that proton mobility one day. **Remco**, thank you for all the chats and laughs. With the two of you, **Viola, Ming and Chao** I always felt a warm environment in the office. **Hannan** there is no talk with you when there is not at least one joke; thank you for the fun chats, laughter and the rapping hours where we discovered your talent. I wish you all the best with finishing your PhD. **Tammo**, thank you for keeping up us to date about the football results in the Netherlands, and for being the barista at the coffee breaks. And **Viola**, you were the only person I could relate to in experience during these years, the hard times brought us together, and together we have enjoyed many happy ones too. Thank you for your support and friendship in and outside of work. And to all others, thanks for the moments shared, I am sure we will share many more in the next 2 years: **Zhaolong, Eveline, Victor, Mark(1), Mark(2), Pranav, Theo, Pier and Lars**.

A special thanks to my friends, **Tipnis**, for always being there along the years, **Manuel** for the beautiful cover design and the fun 3-people parties during corona. To my Spanish-speaking support crew: **Jesu**, desde tiempos de ingeniería química en Colombia siempre he podido contar con vos, y la distancia no ha sido un obstáculo; gracias por venir de visita y por recibirme en Alemania, una vez al año no hace daño. **Lucho**, gracias por motivarme a seguir con la guitarra, y por los viajes, de visita o de paseo. **Meli y Jose Pablo**, por los findes relajados, las lecciones de surf y las acampadas de festival mal preparadas. **María**, maquito, gracias por tu apoyo constante, tu nobleza y tu paciencia. gracias por compartir tantas experiencias. gracias por la ayuda en los días más oscuros, y también en los más claros. gracias por darme la mano siempre sin reparos. gracias por compartir un buen café, hasta el que está malo, gracias por recorrer el mundo como voladores sin palo. éste no es el final de la aventura, sino el comienzo de otra, sólo que ahora lo haremos como dos doctoras. **Frank**, te tengo que agradecer varias cosas a lo largo de los años. Gracias por los cafés de media tarde, las conversaciones interesantes, y las risas en los días estresantes. Pero sobre todo gracias por tu apoyo en los últimos meses, lo has hecho todo más fácil y llevadero. Gracias por estar aquí.

Y finalmente, quiero dar las gracias a las personas sin las que no podría estar aquí: mi familia. **Pa y Ma**, ustedes siempre han creído en mí y me han enseñado a perseverar por mis sueños. No puedo agradecerles lo suficiente por sus años de sacrificio por nosotros. **Pa**, recuerdo aquellas noches de salir al patio y mirar las estrellas, buscando constelaciones y señales. Desde entonces me he preguntado cómo funciona el universo, me he maravillado con él y he soñado con ser una "científica". Las decisiones que he tomado desde entonces me han traído aquí, siguiendo ese sueño. Gracias pa, por inculcarme la curiosidad. **Ma**, la curiosidad por sí sola no es suficiente, y vos me has inculcado la perseverancia y la fortaleza para perseguir lo que quiero. Sin tus enseñanzas me habría rendido en el camino. **Javi**, tu curiosidad infinita le da fuerza a la mía. Siempre me has hecho pensar en cosas diferentes y desde diferentes puntos de vista. Desde discusiones de filosofía, música o la vida, siempre me has ayudado a expandir mi mente. Gracias por ayudarme a crecer. **Mamá**, gracias por cuidar de mí, apoyar mis decisiones y tenerme siempre presente, su ayuda y la de **tía** lo han hecho todo siempre más fácil. Y al resto de mi familia, **madrina, tías, tíos, primos, primas**, que de una u otra forma me han ayudado a través de los años. Con mensajes de apoyo y motivación, visitas cuando voy a casa, y lugares donde donde pasar las noches en mis largas travesías entre Ocaña y Holanda, a todos muchas gracias, han hecho este camino mucho mejor.

Angie
Delft, 2021

Curriculum Vitæ

Angie Lorena Rangel Cárdenas

Angie L. Rangel Cárdenas was born on the 17th of November, 1990 in Ocaña, Colombia. In 2007 she moved to Bucaramanga, Colombia where she started a 5-year engineering program at Universidad Industrial de Santander (UIS). In 2012 she graduated as a Chemical Engineer with a final thesis on the topic of Life Cycle Assessments in an industrial electroplating process.

In 2013, Angie moved to Delft, the Netherlands to start a master's degree in Sustainable Energy Technologies. There she followed a photovoltaics track as an specialisation. She also specialised in energy storage and culminated her degree in 2015 with a thesis on energy storage in aqueous batteries. At the same time, she had the opportunity to be an intern at ECN in the biomass department, again in a project related to Life Cycle Assessments.

Electrochemistry and materials became her passion, which led her to start a Ph.D. in material science and electrochemistry in 2016 in the project "Charge carrier dynamics in PEM fuel cells" at the Advanced Soft Matter group in the Chemical Engineering department at TU Delft. This project was funded by ADEM and co-developed in the Storage of Electrochemical Energy group at the Radiation, Science and Technology department. During her research years she had the opportunity to become acquainted with several advanced material characterisation techniques and also had the chance to work together with several students. She supervised 6 master students in their final project, 1 bachelor student and assisted in the laboratory courses for first and second year bachelors supervising many of them in small projects.

In 2020, she started as a postdoctoral researcher at the Storage of Electrochemical Energy group at the Radiation, Science and Technology department in the topic of materials for water electrolysis.



List of Publications & Oral Presentations

6. **A.L. Rangel-Cárdenas**, M.Fehse, S.J. Picken, Koper, G.J.M. & E.M. Kelder. *Protonated spinel Lithium Manganese Oxides as electrocatalysts for HOR and ORR in PEMFCs*, **In Preparation**.
5. **A.L. Rangel-Cárdenas**, S. Ganapathy, G.J.M. Koper, S.J. Picken, M. Wagemaker & E.M. Kelder. *Proton exchange in spinel LiMn_2O_4 for ORR in acidic environments - Structure and activity*, **In Preparation**.
4. **A.L. Rangel-Cárdenas**, G.J.M. Koper & S.J. Picken. *Anomalous water sorption kinetics in a carbon-supported Nafion thin-film membrane-electrode assembly*, **In Preparation**.
3. **A.L. Rangel-Cárdenas** & M.Fehse, S.J. Picken, Koper, G.J.M. & E.M. Kelder. *Protonated spinel Lithium Manganese Oxides as electrocatalysts for HOR and ORR in PEMFCs*, [70th Annual International Society of Electrochemistry meeting, ISE \(2019\)](#).
2. **A.L. Rangel-Cárdenas** & G.J.M. Koper. **Soundbite**. *Transport in proton exchange membranes for fuel cell applications — a systematic non-equilibrium approach*, [6th Conference of the International Association of Colloid and Interface Scientists, IACIS \(2018\)](#).
1. **A.L. Rangel-Cárdenas** & G.J.M. Koper. *Transport in proton exchange membranes for fuel cell applications — a systematic non-equilibrium approach*, [Materials](#) **10**(6), 576 (2017).

